

Electrostatics in ionic solution
work and energy, charge regulation, and
inhomogeneous surfaces

ISBN: 978-90-393-5724-8

Electrostatics in ionic solution
work and energy, charge regulation, and
inhomogeneous surfaces

Elektrostatica in ionische oplossingen
arbeid en energie, ladingsregulatie, en inhomogene oppervlakken

(met een samenvatting in het Nederlands)

Proefschrift

ter verkrijging van de graad van doctor aan de Universiteit Utrecht op gezag van de rector magnificus, prof.dr. G.J. van der Zwaan, ingevolge het besluit van het college voor promoties in het openbaar te verdedigen op dinsdag 31 januari 2012 des ochtends te 10.30 uur

door

Nicolaas Jacobus Henricus Boon

geboren op 22 augustus 1984 te Alkmaar

Promotor: Prof.dr. H. van Beijeren
Co-promotor: Dr. R.H.H.G. van Roij

Dit proefschrift werd mogelijk gemaakt met financiële steun van de Nederlandse Organisatie voor Wetenschappelijk Onderzoek (NWO).

Contents

1	Introduction	3
1.1	Colloids	3
1.2	Ions	4
1.3	Charge and screening	5
2	Effective electrostatic interactions	7
2.1	Introduction	7
2.2	Density functional theory	8
2.3	Mean-field theory	11
2.4	The Poisson-Boltzmann equation	12
2.5	Planar geometry	13
2.6	Linear PB and DLVO theory	14
2.7	Spherical cell theory and charge renormalisation	17
2.8	Discussion	19
3	Reversible ‘Blue energy’ by cyclic double-layer (de-)compression	21
3.1	Introduction	21
3.2	System and thermodynamics	24
3.3	Microscopic model and density functional theory	28
3.4	Numerical results	32
3.5	Limited fresh water supply	38
3.6	Discussion	40
4	Charge reversal of porous silica colloids by proton uptake	43
4.1	Introduction	43
4.2	Theory	45
4.3	Results and discussion	50
4.4	Silica in water	54
4.5	Discussion	54

5	Electrostatic interactions between Janus particles	57
5.1	Introduction	57
5.2	Method	59
5.3	Results	62
5.4	DLVO theory for dipolar colloids	64
5.5	Discussion	70
6	Charge renormalisation of Janus particles	73
6.1	Introduction	73
6.2	Theory	75
6.3	Results	76
6.4	Discussion	81
7	Phase diagrams of spheres with a constant zeta-potential	85
7.1	Introduction	85
7.2	Model and theory	87
7.3	Effective charge and screening length	89
7.4	Effective interactions and phase diagrams	91
7.5	Summary and conclusions	96
	Appendix: Jellium model	97
8	Charge regulation and ionic screening of patchy surfaces	99
8.1	Introduction	99
8.2	Theory	101
8.3	Results	108
8.4	Discussion	117
	Appendix: Nonlinear PB	118
9	Effective attraction between similar patchy surfaces	121
9.1	Introduction	121
9.2	Theory	123
9.3	Method	125
9.4	Results	125
9.5	Random patchiness	130
9.6	Discussion	132
10	Conclusions and Outlook	135
	Bibliography	138
	Samenvatting voor iedereen	145
	Dankwoord	149
	Publications	151

The air that forms our atmosphere is a gas of fast-moving molecules that exchange kinetic energy during collisions with other gas molecules and solid objects, as if they were involved in a giant 3-dimensional game of billiards on a nanometer scale. The average energy that is transferred during each of these collisions is extremely small, about 10^{-21} Joule at room temperature. Air molecules are nevertheless so tiny that this energy scale involves velocities which are, maybe not surprisingly, in the order of the speed of sound. Unlike a normal game of billiards in which all balls eventually stop rolling, the movement of air molecules is perpetual. This is because on a nanometer scale, the molecules that form the walls, a page of this thesis, or a billiard table, shake so vigorously that the air molecules that collide with these never come to rest.

The average thermal kinetic energy of translation is independent of the mass or other properties of a particle. Therefore the associated thermal velocity is too low to be visible for large (and heavy) ‘particles’ that we can see with our bare eye, such as grains of sand. However, by using just a normal light microscope it can be observed that micron-sized objects on a water-air interface are significantly affected by these thermal excitations, and accordingly display a random movement that is a direct result of their thermal velocity. This was what Brown observed in 1827 when he studied pollen grains under his microscope [1]. Einstein and Sutherland were the first to relate this so-called Brownian motion to the constant bombardment with invisibly small molecules, and Einstein related the diffusion of the particles to their size, the temperature and the viscosity of the solvent [2, 3].

1.1 Colloids

Considering particles inside a liquid, the so-called *colloidal* size regime with particle sizes between ≈ 10 nm and $1 \mu\text{m}$ is special. In this regime particles are much larger than the molecules of the solvent, which can therefore be considered to be a

continuum, but the particles are small enough to be able to explore different spatial configurations due to Brownian motion. Since these particles do not immediately ‘sink’ to the bottom, larger structures like colloidal strings or crystals might form spontaneously. A well known natural example of this are colorful opal gems, in which a spontaneous crystalline ordering of colloids has been ‘frozen in’, causing interesting optical properties. Colloidal systems are present in our everyday life. Examples are paints, inks, cosmetic products and various food products, which all consist of colloidal particles suspended in a liquid continuous medium. However, the continuous medium can also be a gas [4]; fog can be regarded as a colloidal system of small water droplets in air. Apart from their intrinsic interests, colloids are interesting to study the behaviour of atomic and molecular systems [5] as their greater size and larger time scales often make experiments much easier to perform. General phenomena in physics, like phase transitions and coexistence, glasses, and various crystal structures, are also observed in colloidal systems. Nowadays, colloids can be made synthetically with high control over the shape and material properties. Examples include particles with the shape of dumbbells, cubes, caps, or snowmen, or with heterogeneous ‘patchy’ surfaces that can form directional bonds such that new structures (e.g. with a complete photonic band gap or enhanced stability against demixing) can (self-)assemble. In Chapters 5 and 6 we will investigate the electrostatic interactions between spherical ‘Janus’ particles with differently charged hemispheres.

1.2 Ions

Just as the thermal bombardment with water molecules is sufficient to empower Brownian motion, it is also sufficient to break ionic bonds of molecules that are immersed in a solvent. In water, salts easily dissociate. Sodium chloride for example can be split with little effort into the ion pair Na^+ and Cl^- , which causes the salt to dissolve. Although pulling the positive and the negative ion pair apart costs electrostatic energy, dissolution opens up a whole new range of possible spatial configurations of the ion pair, and therefore the probability of a recombination of two opposite ions is often small.

Large objects tend to fall down and remain on the floor. However, on a nanometer scale nature behaves different than on the scale we live. Whilst we see large objects only minimising their potential energy, for microscopic particles the most probable situation is defined not only by the corresponding potential energy, but also by the number of ways the particles can be arranged within a certain situation. Like we mentioned, (table) salt dissolves, but also air molecules are distributed within an atmosphere that is tens of kilometers tall. The competition between energy minimisation and configurational richness can be formulated in terms of the Helmholtz free energy, $F = E - TS$, in which the energy E has been modified by a term TS , with S the entropy which is related to the (logarithm of) the number

of available configurations corresponding to a certain situation (e.g. undissolved vs. dissolved), see e.g. Ref. [6]. The preferred state of the system corresponds to minimal free energy and therefore generally depends on the temperature T . A nice example of this is the mixing of two volumes that contain solutions of different salinity, e.g. seawater and river water. If these volumes are connected to each other the number of available ion configurations increases enormously just by allowing the ions to move between both volumes. Although the associated change in energy is (almost) zero, both volumes will therefore eventually mix spontaneously. This tendency of the ions to gain entropy turns out to be so strong that one can ‘trade’ the mixing of both volumes for a significant extraction of energy by letting the system perform (electrical) work as the volumes mix. In Chapter 3 we will discuss how one can perform such a trade-off optimally, by using a novel method that relies on the use of modern highly porous carbon electrodes [7]. The high porosity of this material grants a very high electrostatic capacity which has led to its use in so-called ultracapacitors. We will exploit the thermodynamic property that the capacity of these electrodes changes with the ion concentration in the electrolyte.

1.3 Charge and screening

Unlike the carbon electrodes for which a (high) surface charge can be delivered by an external source of electric current, the surface of a colloidal particle charges spontaneously by ion dissociation or by preferred adsorption of a particular ion species. As these charging processes are thermal the resulting surface charge densities are not extremely high; associated electrostatic surface potentials larger than 100 mV are rare. Partial ionisation of the surface leads to a charge that depends on the number of ionisable bonds on the colloidal surface and their corresponding bond energies. Similar colloids typically experience an electrostatic repulsion that makes them more stable against coagulation that is induced by short-ranged van der Waals forces [8, 9]. A net electrostatic charge makes colloidal particles move in electric fields. This allows them to be used in for example the electrophoretic displays of e-readers.

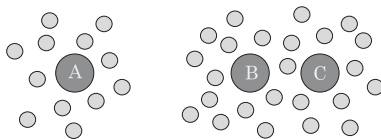


Figure 1.1: A sketch of the counterions (small) in the double layers of three charged colloids (large).

The charged surface electrostatically attracts ions with an opposite charge, but repels similarly charged ions. This causes the formation of a so-called ‘double layer’ of countercharge around the colloid which eventually screens all the surface charge on the colloidal surface, see colloid ‘A’ in Fig. 1.1, where we sketched the counter-

ons in the double layer. Entropic benefits for the ions cause that the double layer does not condense on the colloidal surface, but has a typical thickness of maximally about a micron in water, known as the Debye screening length. Due to the opposite charge of the double layer, the colloids appear to be uncharged if observed from a few screening lengths distance. Therefore, the only possibility for a pair of colloids to interact electrostatically is when double layers overlap at closer distances, as is sketched for pair 'B' and 'C' in Fig. 1.1.

In Chapters 4, 7, 8, and 9 we will consider surfaces that charge due to various kinds of chemical equilibria. The regulated charge can often be characterised by a single 'chargeability' parameter. In this way, the charge becomes dependent on the colloid density, and typically one observes reduction of the colloid charge in the vicinity of other colloids. This leads to a reduced pair repulsion between similar colloids. A close description of various charge mechanisms can help us to understand experimentally found crystallisation curves, such as for colloids that charge in presence of AOT micelles. Furthermore, an inhomogeneous distribution of chargeable groups on the colloidal surface can often lead to attractions between similar colloids that repel each other at greater distances, as we will see in Chapter 9.

Chapter 2

Effective electrostatic interactions

Abstract

Density functional theory is applied to find the electrostatic interactions of charge configurations suspended in electrolyte. The resulting theory is known as Poisson-Boltzmann theory and involves a nonlinear differential equation for the electrostatic potential. No general analytic solution is known for this equation. Throughout the thesis we will therefore apply theoretical models that give accurate results either in simplified geometries, or for sufficiently low charge densities. In this chapter, we will (re-)derive models that are known from literature and determine the parameter space in which they can be applied.

2.1 Introduction

Elementary electrostatics teaches us that the electrostatic energy that is needed to assemble a certain charge configuration $q(\mathbf{r})$ in vacuum involves a straightforward calculation using Coulomb's law,

$$H_{\text{vacuum}}[q] = \frac{e^2}{2} \iint d\mathbf{r} d\mathbf{r}' \frac{q(\mathbf{r})q(\mathbf{r}')}{|\mathbf{r} - \mathbf{r}'|} - U_{\text{self}}, \quad (2.1)$$

with e the elementary charge, $q(\mathbf{r})$ the charge density in units of elementary charges per volume, and U_{self} a constant self-energy term. Eq. (2.1) is expressed in the Gaussian system, such that the dielectric permittivity of vacuum $\epsilon_0 = 1$ and the elementary charge $e = 1.5 \cdot 10^{-14} \text{ kg}^{1/2} \text{ m}^{3/2} \text{ s}^{-1}$. Eq. (2.1) can for example be used to calculate the electrostatic force between charged particles or to find the work that is needed to charge a conducting surface. In this chapter we will generalise this description towards systems in which the charge configuration is suspended in an electrolytic solution at temperature T , consisting of solvent molecules and ions in the form of cations(+) and anions(-). The effective electrostatic energy of the configuration $q(\mathbf{r})$ then results from interaction between the charges themselves, but also from interactions with solvent molecules and ions. One has in principle to consider all degrees

of freedom in position and orientation of these particles in order to find the effective interaction energy of the configuration $q(\mathbf{r})$. This is generally impossible as the number of solvent molecules and ions is typically extremely large. However by using appropriate approximations on the (electrostatic) properties of the solvent and the ions it is possible to find a description of the electrostatic energy in which the degrees of freedom of the medium are *integrated out*. It is a natural choice to start such a procedure by considering the solvent molecules as their number exceeds the number of ions by a large factor. Solvent molecules are charge neutral and typically form an incompressible liquid. The molecules however in general have a dipole moment which causes a tendency to align with electric fields. At the minimum free energy (as we consider the system to be at constant temperature) of the solvent the gain in electrostatic energy of the individual molecules by aligning with the field is balanced by the corresponding loss in rotational entropy. Electrostatics teaches us a very accurate approximation in which all the degrees of freedom of the solvent molecules are integrated out by introducing an effective Coulomb pair interaction in which the interactions as given in Eq. (2.1) are modified by a factor ϵ^{-1} , with ϵ the dielectric constant of the solvent. At the dielectric interface between a (colloidal) surface and the liquid one has to add a bound- (polarisation induced) charge density that is determined by the local electric field and the ratio of the dielectric constant at both sides of the interface [10]. Throughout this thesis, the solvent will be treated at this level of approximation.

2.2 Density functional theory

Just as it is possible to integrate out the degrees of freedom of the solvent molecules it is also possible to integrate out the degrees of freedom of the ions, for instance by using density functional theory (DFT), see e.g. Ref. [11]. The ions can be regarded as a gas of charged species that 'live' inside the solvent. The ions have charges $\pm e$, where we assume that the ions are monovalently charged. It turns out to be convenient to treat the ions grand-canonically; one assumes that the system is connected to a large reservoir of electrolyte such that the chemical potential of both ion species is fixed and one is therefore able to define a 'bulk' density of ions. Eventually, a Legendre transformation can be applied at the end of the calculations should the number of ions be fixed, as we will see in Chapter 3. By considering the locations and charges of the non-ionic charges (e.g. colloidal particles) as a fixed background $q(\mathbf{r})$, the Hamiltonian that describes the electrostatic and hard-core interactions of a system of N_+ cations and N_- anions is given by

$$H_{N_+,N_-} = K + \Phi + \mathcal{V}, \quad (2.2)$$

with K the kinetic energy, Φ the ion-ion interaction, and \mathcal{V} the electrostatic interaction with the fixed density $q(\mathbf{r})$ and with the hard-core potential \mathcal{V}_{HC} . The kinetic

energy is given by

$$K = \sum_{i=1}^{N_+} \frac{\mathbf{p}_{+i}^2}{2m_+} + \sum_{i=1}^{N_-} \frac{\mathbf{p}_{-i}^2}{2m_-}, \quad (2.3)$$

where m_{\pm} is the mass of the concerned ion species, and $\mathbf{p}_{\pm i}$ are the linear momenta. By approximating the cations(+) and anions(-) as charged hard-core particles with respective particle radii a_+ and a_- , the interactions between the ions can be described as

$$\Phi = \sum_{i=1}^{N_+} \sum_{j=1}^{N_-} \Phi_{+-}(|\mathbf{r}_{+i} - \mathbf{r}_{-j}|) + \sum_{i<j}^{N_+} \Phi_{++}(|\mathbf{r}_{+i} - \mathbf{r}_{+j}|) + \sum_{i<j}^{N_-} \Phi_{--}(|\mathbf{r}_{-i} - \mathbf{r}_{-j}|), \quad (2.4)$$

where

$$\Phi_{\alpha\alpha'}(r) = \begin{cases} \infty & \text{if } r < a_{\alpha} + a'_{\alpha'}; \\ \alpha\alpha' \frac{e^2}{\epsilon r} & \text{if } r \geq a_{\alpha} + a'_{\alpha'}. \end{cases} \quad (2.5)$$

The interactions of the ions with the fixed charges can be regarded as an interaction with an external potential at this point. They are given by

$$\mathcal{V} = \sum_{i=1}^{N_+} \mathcal{V}_+(\mathbf{r}_{+i}) + \sum_{i=1}^{N_-} \mathcal{V}_-(\mathbf{r}_{-i}), \quad (2.6)$$

where

$$\mathcal{V}_{\pm}(\mathbf{r}) = \mathcal{V}_{\text{HC}}(\mathbf{r}) + \int d\mathbf{r}' \frac{e^2 \pm q(\mathbf{r}')}{\epsilon |\mathbf{r} - \mathbf{r}'|}. \quad (2.7)$$

Here, $q(\mathbf{r})$ is the charge density of the fixed charges and $\mathcal{V}_{\text{HC}}(\mathbf{r})$ is a hard-core potential that is needed because the charge distribution may occupy a certain volume that is therefore impenetrable to ions. More explicitly, for a system of M spherical colloidal particles at positions \mathbf{r}_{ci} and charge Z (in the centers) these functions are

$$q(\mathbf{r}) = \sum_{i=1}^M Z \delta^3(\mathbf{r} - \mathbf{r}_{ci}), \quad (2.8)$$

and

$$\beta \mathcal{V}_{\text{HC}}(\mathbf{r}) = \sum_{i=1}^M \begin{cases} \infty & \text{if } |\mathbf{r} - \mathbf{r}_{ci}| < a, \\ 0 & \text{if } |\mathbf{r} - \mathbf{r}_{ci}| > a, \end{cases} \quad (2.9)$$

where $\beta = 1/k_{\text{B}}T$, with k_{B} the Boltzmann constant and T the temperature. In Eq. (2.9), a is the colloidal radius. However, $q(\mathbf{r})$ and $\mathcal{V}_{\text{HC}}(\mathbf{r})$ can also be chosen to represent any other (colloidal) distribution of charges and will therefore be kept in their general forms in the remainder of this derivation. We consider the grand-partition function of the ions

$$\Xi = \text{Tr}_{\text{cl}} \exp[-\beta(H_{N_+,N_-} - \mu_+ N_+ - \mu_- N_-)], \quad (2.10)$$

where μ_{\pm} are the ionic chemical potentials and in which the grand-canonical classical trace involves the usual integrals over all phase-space and sums over all numbers of ions,

$$\text{Tr}_{\text{cl}} = \sum_{N_+=1}^{\infty} \sum_{N_-=1}^{\infty} \frac{1}{N_+!N_-!h^{3(N_++N_-)}} \int d\mathbf{p}^{N_++N_-} d\mathbf{r}^{N_++N_-}. \quad (2.11)$$

The average $\langle \hat{\mathcal{A}} \rangle$ of any operator that depends on the phase-space variables $(\mathbf{r}_{i\pm}, \mathbf{p}_{i\pm})$ can be expressed as

$$\langle \hat{\mathcal{A}} \rangle = \text{Tr}_{\text{cl}} f_0 \mathcal{A}, \quad (2.12)$$

with

$$f_0(\mathbf{r}_{i\pm}, \mathbf{p}_{i\pm}; N_+, N_-) = \frac{1}{\Xi} \exp[-\beta(H_N - \mu_+ N_+ - \mu_- N_-)] \quad (2.13)$$

the normalised equilibrium distribution. It is useful to define the *intrinsic local chemical potential*,

$$\Psi_{\pm}(\mathbf{r}) = \mu_{\pm} - \mathcal{V}_{\pm}(\mathbf{r}), \quad (2.14)$$

which depends on the chemical potential and the interaction potential with the fixed charge density. By introducing a short notation for the evaluation of this local chemical potential at the positions of the ions

$$\Psi_{N\pm} = \sum_{i=1}^{N_{\pm}} \Psi_{\pm}(\mathbf{r}_{\pm i}), \quad (2.15)$$

we are able to write $H_N - \mu_+ N_+ - \mu_- N_- = K + \Phi - \Psi_{N_+} - \Psi_{N_-}$. Considering now an infinitesimal variation $\delta\Psi_{\pm}(\mathbf{r})$ of the local chemical potential of one ion species, one finds that the corresponding change in the grand potential $\Omega = -k_B T \log \Xi$ is

$$\begin{aligned} \Omega[\Psi_{\pm} + \delta\Psi_{\pm}] - \Omega[\Psi_{\pm}] &= -k_B T \log \frac{\Xi[\Psi_{\pm} + \delta\Psi_{\pm}]}{\Xi[\Psi_{\pm}]} \\ &= -k_B T \log \frac{\text{Tr}_{\text{cl}} \exp[-\beta(H_N - \mu_+ N_+ - \mu_- N_- - \delta\Psi_{N\pm})]}{\text{Tr}_{\text{cl}} \exp[-\beta(H_N - \mu_+ N_+ - \mu_- N_-)]} \\ &= -k_B T \log \frac{\text{Tr}_{\text{cl}} \exp[-\beta(H_N - \mu_+ N_+ - \mu_- N_-)] (1 + \beta \delta\Psi_{N\pm})}{\Xi} \\ &= -k_B T \log(1 + \beta \langle \delta\Psi_{N\pm} \rangle) = -\langle \delta\Psi_{N\pm} \rangle \\ &= - \int d\mathbf{r} \tilde{\rho}_{\pm}(\mathbf{r}) \delta\Psi_{\pm}(\mathbf{r}), \end{aligned} \quad (2.16)$$

in which $\tilde{\rho}_{\pm}(\mathbf{r}) = \text{Tr}_{\text{cl}} f_0 \hat{\rho}_{\pm}(\mathbf{r})$ is the local equilibrium density profile of the concerned ion species which can be found by applying the density operator $\hat{\rho}_{\pm}(\mathbf{r}) = \sum_{i=1}^{N_{\pm}} \delta(\mathbf{r}_{\pm i} - \mathbf{r})$ to Eq. (2.13). It follows that Eq. (2.16) can be written as a functional derivative,

$$\frac{\delta\Omega[\Psi_{\pm}]}{\delta\Psi_{\pm}(\mathbf{r})} = -\tilde{\rho}_{\pm}(\mathbf{r}). \quad (2.17)$$

With $\tilde{\rho}_{\pm}(\mathbf{r})$ thus being the conjugate to $\Psi_{\pm}(\mathbf{r})$, it is possible to perform a Legendre transformation in which the independent functions $\Psi_{\pm}(\mathbf{r})$ are replaced by the equilibrium densities $\tilde{\rho}_{\pm}(\mathbf{r})$. The intrinsic Helmholtz free energy is obtained,

$$F[\tilde{\rho}_+, \tilde{\rho}_-] = \Omega[\Psi_+, \Psi_-] + \int d\mathbf{r} \tilde{\rho}_+(\mathbf{r})\Psi_+(\mathbf{r}) + \int d\mathbf{r} \tilde{\rho}_-(\mathbf{r})\Psi_-(\mathbf{r}). \quad (2.18)$$

It can be proven [11] that (I) $F[\rho_+(\mathbf{r}), \rho_-(\mathbf{r})]$ is a functional only of the functions $\rho_{\pm}(\mathbf{r})$ and therefore is independent of $\Psi_{\pm}(\mathbf{r})$, and (II) the functional

$$\Omega[\rho_+, \rho_-] = F[\rho_+, \rho_-] - \int d\mathbf{r} \rho_+(\mathbf{r})\Psi_+(\mathbf{r}) - \int d\mathbf{r} \rho_-(\mathbf{r})\Psi_-(\mathbf{r}), \quad (2.19)$$

is minimised if both $\rho_{\pm}(\mathbf{r})$ equal the equilibrium densities $\tilde{\rho}_{\pm}(\mathbf{r})$ for given $\Psi_+(\mathbf{r})$ and $\Psi_-(\mathbf{r})$. The minimum value is the equilibrium grand potential of the system.

2.3 Mean-field theory

By construction, the intrinsic Helmholtz free-energy functional (2.18) does not depend explicitly on the interactions with fixed charges. Therefore, applying a mean-field approximation and using an ideal-gas reference system for both ion species we may estimate this free energy by

$$F[\rho_+, \rho_-] = F_{\text{id}}[\rho_+, \rho_-] + \frac{1}{2} \iint d\mathbf{r} d\mathbf{r}' \frac{e^2 (\rho_+(\mathbf{r}) - \rho_-(\mathbf{r}))(\rho_+(\mathbf{r}') - \rho_-(\mathbf{r}'))}{\epsilon |\mathbf{r} - \mathbf{r}'|}, \quad (2.20)$$

in which the second term governs the interactions between the ions as in Eq. (2.4) and the first term is the ideal-gas contribution

$$\beta F_{\text{id}}[\rho_+, \rho_-] = \sum_{\alpha=\pm} \int d\mathbf{r} \rho_{\alpha}(\mathbf{r}) \left(\log \rho_{\alpha}(\mathbf{r}) \Lambda_{\pm}^3 - 1 \right). \quad (2.21)$$

The grand-potential functional follows from Eq. (2.19),

$$\beta \Omega[\rho_+, \rho_-] = \beta \Omega_{\text{id}}[\rho_+, \rho_-] + \beta \Omega_{\Phi}[\rho_+, \rho_-] - \beta \Omega_{\nu}[\rho_+, \rho_-]. \quad (2.22)$$

The ideal-gas term is

$$\beta \Omega_{\text{id}}[\rho_+, \rho_-] = \sum_{\alpha=\pm} \int d\mathbf{r} \rho_{\alpha}(\mathbf{r}) \left(\log \frac{\rho_{\alpha}(\mathbf{r})}{\rho_s} - 1 \right), \quad (2.23)$$

for which it was used that $\mu_{\pm} = k_B T \log \rho_s \Lambda_{\pm}^3$, with ρ_s being the bulk density of both species. The terms that govern the ion-ion interaction and the interaction with the fixed charges yield

$$\beta \Omega_{\Phi}[\rho_+, \rho_-] = \sum_{\alpha=\pm} \sum_{\alpha'=\pm} \frac{1}{2} \iint d\mathbf{r} d\mathbf{r}' \lambda_B \frac{\rho_{\alpha}(\mathbf{r}) \rho_{\alpha'}(\mathbf{r}')}{|\mathbf{r} - \mathbf{r}'|}, \quad (2.24)$$

and

$$\beta\Omega_{\mathcal{V}}[\rho_+, \rho_-] = - \sum_{\alpha=\pm} \iint \mathrm{d}\mathbf{r} \mathrm{d}\mathbf{r}' \lambda_{\mathrm{B}} \frac{q(\mathbf{r})\rho_{\alpha'}(\mathbf{r}')}{|\mathbf{r}-\mathbf{r}'|} - \int \mathrm{d}\mathbf{r} (\rho_+(\mathbf{r}) + \rho_-(\mathbf{r}))\beta\mathcal{V}_{\mathrm{HC}}(\mathbf{r}), \quad (2.25)$$

respectively, with $\lambda_{\mathrm{B}} \equiv \beta e^2/\epsilon$ the so-called Bjerrum length. By introducing the total charge density $Q(\mathbf{r}) = q(\mathbf{r}) + \rho_+(\mathbf{r}) - \rho_-(\mathbf{r})$ and the dimensionless electrostatic potential

$$\phi(\mathbf{r}) = \int \mathrm{d}\mathbf{r}' \lambda_{\mathrm{B}} \frac{Q(\mathbf{r}')}{|\mathbf{r}-\mathbf{r}'|}, \quad (2.26)$$

it is possible to rewrite Eq. (2.22) as

$$\beta\Omega[\rho_+, \rho_-] = \beta\Omega_{\mathrm{id}}[\rho_+, \rho_-] + \frac{1}{2} \int \mathrm{d}\mathbf{r} Q(\mathbf{r})\phi(\mathbf{r}) + \int \mathrm{d}\mathbf{r} (\rho_+(\mathbf{r}) + \rho_-(\mathbf{r}))\beta\mathcal{V}_{\mathrm{HC}}(\mathbf{r}). \quad (2.27)$$

Note that the latter equation includes an extra constant term (w.r.t. to the ion densities ρ_{\pm}) which describes the direct interaction of the charge distribution $q(\mathbf{r})$ with itself. Eq. (2.27) is the Poisson-Boltzmann grand potential which can be used to find the effective electrostatic energy of a charge configuration $q(\mathbf{r})$ as we will see now.

2.4 The Poisson-Boltzmann equation

Up to now we considered the charge distribution $q(\mathbf{r})$ and the associated hard-potential $\mathcal{V}_{\mathrm{HC}}$ as being fixed and calculated the grand potential as a functional of the ion-density profiles $\rho_{\pm}(\mathbf{r})$. In the remainder of the chapter we will minimise Eq. (2.27) w.r.t. the ion densities $\rho_{\pm}(\mathbf{r})$ in order to obtain the effective electrostatic energy as a functional of the charge distribution $q(\mathbf{r})$. The ion densities can be regarded as 'integrated out' at that point. A functional derivative of Eq. (2.27) shows that the ion densities $\rho_{\pm}(\mathbf{r})$ are minimised by

$$\rho_{\pm}(\mathbf{r}) = \begin{cases} \rho_{\mathrm{s}} \exp[\mp\phi(\mathbf{r})] & \text{if } \beta\mathcal{V}_{\mathrm{HC}}(\mathbf{r}) = 0, \\ 0 & \text{if } \beta\mathcal{V}_{\mathrm{HC}}(\mathbf{r}) = \infty. \end{cases} \quad (2.28)$$

which in combination with Eq. (2.26) in differential form gives the Poisson-Boltzmann equation,

$$\nabla^2 \phi(\mathbf{r}) = -4\pi\lambda_{\mathrm{B}}q(\mathbf{r}) + \begin{cases} \kappa^2 \sinh \phi(\mathbf{r}) & \text{if } \beta\mathcal{V}_{\mathrm{HC}}(\mathbf{r}) = 0, \\ 0 & \text{if } \beta\mathcal{V}_{\mathrm{HC}}(\mathbf{r}) = \infty, \end{cases} \quad (2.29)$$

with $\kappa = \sqrt{8\pi\lambda_{\mathrm{B}}\rho_{\mathrm{s}}}$ the Debye screening parameter.

Inserting the resulting ion-density profiles we note that Eq. (2.27) yields the effective Hamiltonian $H[\rho_{\pm}[q, \mathcal{V}_{\text{HC}}], q, \mathcal{V}_{\text{HC}}]$ for a system with charge distribution $q(\mathbf{r})$ and hard-core potential $\mathcal{V}_{\text{HC}}(\mathbf{r})$. The effective Hamiltonian can be written as

$$\beta H[q, \mathcal{V}_{\text{HC}}] = 2\rho_s \int_{V_{\text{out}}} d\mathbf{r} \left(\frac{1}{2} \phi(\mathbf{r}) \sinh \phi(\mathbf{r}) - \cosh \phi(\mathbf{r}) \right) + \frac{1}{2} \int d\mathbf{r} q(\mathbf{r}) \phi(\mathbf{r}), \quad (2.30)$$

where the first integral concerns the electrostatic energy and entropy of the ions, therefore we only integrate over V_{out} , which is the volume that is not excluded by the hard cores and therefore available for ions.

We may take the total functional derivative w.r.t. q of Eq. (2.27),

$$\frac{dH[\rho_{\pm}[q, \mathcal{V}_{\text{HC}}], q, \mathcal{V}_{\text{HC}}]}{dq(\mathbf{r})} = \sum_{\alpha=\pm} \frac{\delta H[\rho_{\pm}[q, \mathcal{V}_{\text{HC}}], q, \mathcal{V}_{\text{HC}}]}{\delta \rho_{\pm}[q, \mathcal{V}_{\text{HC}}]} \frac{\delta \rho_{\pm}[q, \mathcal{V}_{\text{HC}}]}{\delta q(\mathbf{r})} \quad (2.31)$$

$$+ \frac{\delta H[\rho_{\pm}[q, \mathcal{V}_{\text{HC}}], q, \mathcal{V}_{\text{HC}}]}{\delta q(\mathbf{r})} = k_{\text{B}} T \phi(\mathbf{r}). \quad (2.32)$$

Note that the first term on the right side vanished because the grand potential is in a minimum w.r.t. to the ion densities, $\frac{\delta H[\rho_{\pm}[q, \mathcal{V}_{\text{HC}}], q, \mathcal{V}_{\text{HC}}]}{\delta \rho_{\pm}[q, \mathcal{V}_{\text{HC}}]} = 0$. Although the existence of the conjugate pair q and ϕ of Eq. (2.32) might have been expected, Eq. (2.32) turns out to be very useful in order to calculate the effective energy of a charge configuration, as we will see later.

2.5 Planar geometry

In planar geometry with cartesian coordinate z in the normal direction, the PB equation (2.29) is a one-dimensional differential equation,

$$\phi''(z) = \kappa^2 \sinh \phi(z) - 4\pi\lambda_{\text{B}} q(z), \quad (2.33)$$

with a prime denoting the derivative w.r.t. z . If we consider a solid half space at $z < 0$ with a charge density $e\sigma$ on its surface at $z = 0$, then the charge distribution and hard-core potential are given by

$$q(z) = \sigma \delta(z), \quad (2.34)$$

$$\beta \mathcal{V}_{\text{HC}}(z) = \begin{cases} 0 & \text{if } z \geq 0; \\ \infty & \text{if } z < 0. \end{cases} \quad (2.35)$$

The PB equation (2.33) is analytically solvable in this case and one finds for $z > 0$

$$\phi(z) = \log \frac{1 + \gamma \exp[-\kappa z]}{1 - \gamma \exp[-\kappa z]}, \quad (2.36)$$

where the integration constant γ follows from the boundary conditions (Gauss' law) on the interface at $z = 0$, such that

$$4\pi\sigma\lambda_B\kappa^{-1} \equiv y \Rightarrow \gamma = \frac{\sqrt{1+(y/2)^2}-1}{y/2}. \quad (2.37)$$

The associated ion densities follow from Eq. (2.28). Inside the plate, $z < 0$, the electric field vanishes as otherwise the electrostatic potential would diverge for $z \downarrow -\infty$.

Recall that Eq. (2.32) gives that $\partial H[q, \mathcal{V}_{\text{HC}}]/\partial q(z) = k_B T \phi(z)$, such that for an infinitesimal change $\Delta q(z) = \Delta\sigma\delta(z-0)$ the corresponding change in the energy of the system is $\beta\Delta H = \int_z \phi(z)\Delta q(z) = \phi(0)\Delta\sigma$. The electrostatic energy per unit plate area that is needed to charge the plate reads

$$\begin{aligned} H(\sigma) - H(0) &= k_B T \int_0^\sigma d\sigma' \phi(0) = \int_0^\sigma d\sigma' \log \frac{1+\gamma}{1-\gamma} \\ &= k_B T \frac{\kappa}{2\pi\lambda_B} \left(y \sinh^{-1} \left(\frac{y}{2} \right) + 2 - \sqrt{4+y^2} \right). \end{aligned} \quad (2.38)$$

The latter equation can for example be used to study the effect of a changing salt concentration on the electrostatic energy of a charged plate. For weakly charged plates, $y \ll 1$, we obtain $H(\sigma) - H(0) \approx k_B T 2\pi\lambda_B \kappa^{-1} \sigma^2$. This is the same expression one finds for a plate capacitor with plate distance κ^{-1} , the typical distance of the ions in the layer of countercharge that screen the charge of the plate. As y becomes larger one finds that the differential capacitance per unit area,

$$C = \beta e^2 \frac{d\sigma}{d\phi(0)} = \frac{1}{4\pi} \kappa \sqrt{1 + \frac{y^2}{4}} \quad (\text{Gaussian units}), \quad (2.39)$$

increases. We thus observe that due to nonlinear screening effects the layer of ionic countercharge shrinks. This is known as counterion condensation [12–15].

2.6 Linear PB and DLVO theory

In this section we will derive the electrostatic part of DLVO theory, which can be applied to calculate the electrostatic interactions of colloidal particles with moderate charges at lower volume fractions. We will first describe the interaction of colloidal particles *without* hard cores, after which we will 'freeze' the ions that are inside the cores of the particles to obtain equations that describe the electrostatic interactions between charged colloidal particles *with* hard cores. We start by considering a system that consists of M equally charged point particles, given by the charge distribution of Eq. (2.8). We consider the approximation $\log(\rho_\pm(\mathbf{r})/\rho_s) \approx \rho_\pm(\mathbf{r})/\rho_s - 1$ to Eq. (2.23), which is known as the Debye–Hückel approximation, and corresponds

to the case that the ion densities do not significantly vary from ρ_s . The effective Hamiltonian of such a system becomes

$$\beta H[q] = \int d\mathbf{r} \sum_{\alpha=\pm} \rho_{\pm}(\mathbf{r}) \left(\frac{\rho_{\pm}(\mathbf{r})}{\rho_s} - 2 \right) + \frac{1}{2} \int d\mathbf{r} (\rho_+(\mathbf{r}) - \rho_-(\mathbf{r}) + q(\mathbf{r})) \phi(\mathbf{r}). \quad (2.40)$$

We do not question the validity of the Debye-Hückel approximation yet and therefore derive ion densities that follow as $\rho_{\pm}(\mathbf{r}) = \rho_s(1 \mp \phi(\mathbf{r}))$. The PB-equation takes the form

$$\nabla^2 \phi(\mathbf{r}) = \kappa^2 \phi(\mathbf{r}) - 4\pi\lambda_B \sum_{i=1}^M Z \delta(\mathbf{r} - \mathbf{r}_{ci}), \quad (2.41)$$

where Z is the charge of the colloidal particles that are at positions \mathbf{r}_{ci} . This is the linearised PB-equation for point particles. Since the latter differential equation is linear it can be easily solved. The solution is given by

$$\phi(\mathbf{r}) = \sum_{i=1}^M \phi_1(|\mathbf{r} - \mathbf{r}_{ci}|; Z), \quad (2.42)$$

with $\phi_1(r; Z) = Z\lambda_B \exp(-\kappa r)/r$. Recall that Eq. (2.32) gives that $\partial H[q]/\partial q(\mathbf{r}) = k_B T \phi(\mathbf{r})$, such that for an infinitesimal change $\Delta q(\mathbf{r}) = \Delta Z \sum_{i=1}^M \delta^3(\mathbf{r} - \mathbf{r}_{ci})$ the corresponding change in the electrostatic energy is $\beta \Delta H = \int d\mathbf{r} \phi(\mathbf{r}) \Delta q(\mathbf{r}) = \sum_i \phi(\mathbf{r}_{ci}) \Delta Z$. The total electrostatic energy is thus given by

$$\beta H = \int_{Z'=0}^Z dZ' \sum_{i \neq j}^M \phi_1(|\mathbf{r}_{ci} - \mathbf{r}_{cj}|; Z') = \sum_{i < j}^M Z^2 \lambda_B \frac{\exp(-\kappa R_{ij})}{R_{ij}}, \quad (2.43)$$

where $R_{ij} \equiv |\mathbf{r}_i - \mathbf{r}_j|$, and the constant and infinite self-energy part is subtracted that would otherwise follow from choosing $i = j$ in the latter equation. Eq. (2.43) is the well-known interaction potential for point-Yukawa particles. The direct applicability of this pair-potential is however limited as for point-particles the Debye-Hückel approximation obviously does not hold: close to the particles the electrostatic potential (and therefore the ion densities) diverges. However, the Debye-Hückel approximation is safely applicable to sufficiently large particles, since the hard-core of the colloidal particles forbids the ions to enter a regime where Debye-Hückel fails. We only need to account for the hard cores in a proper manner. This will be derived next.

Starting with the obtained solution for the electrostatic potential and ion densities for point particles we imagine a spherical cell of radius a around each point charge, and assume that the positions of these charges in $q(r)$ is chosen such that there are no overlapping cells. The entire volume can be split into the volume V_{out} that consists of all points that are outside these cells, $|\mathbf{r} - \mathbf{r}_{ci}| > a$ for all i , and the volume V_{in} of points that are inside one of these cells, which is the complement of V_{out} . We define $\rho_{\pm, \text{out}}(\mathbf{r})$ and $\rho_{\pm, \text{in}}(\mathbf{r})$ such that $\rho_{\pm, \text{out}}(\mathbf{r}) + \rho_{\pm, \text{in}}(\mathbf{r}) = \rho_{\pm}(\mathbf{r})$

and $\rho_{\pm,\text{out}}(\mathbf{r}) = 0$ for \mathbf{r} inside V_{in} and $\rho_{\pm,\text{in}}(\mathbf{r}) = 0$ for \mathbf{r} inside V_{out} . It is possible to rewrite Eq. (2.40) as

$$\begin{aligned} \beta H[q] &= \int_{V_{\text{out}}} d\mathbf{r} \sum_{\alpha=\pm} \rho_{\pm,\text{out}}(\mathbf{r}) \left(\frac{\rho_{\pm,\text{out}}(\mathbf{r})}{\rho_s} - 2 \right) + \int_{V_{\text{in}}} d\mathbf{r} \sum_{\alpha=\pm} \rho_{\pm,\text{in}}(\mathbf{r}) \left(\frac{\rho_{\pm,\text{in}}(\mathbf{r})}{\rho_s} - 2 \right) \\ &\quad + \frac{1}{2} \int d\mathbf{r} (\rho_{+,\text{out}}(\mathbf{r}) - \rho_{-,\text{out}}(\mathbf{r}) + \tilde{q}(\mathbf{r})) \phi(\mathbf{r}), \end{aligned} \quad (2.44)$$

with $\tilde{q}(\mathbf{r}) = q(\mathbf{r}) + \rho_{+,\text{in}}(\mathbf{r}) - \rho_{-,\text{in}}(\mathbf{r})$ and

$$\phi(\mathbf{r}) = \int d\mathbf{r}' \lambda_B \frac{\rho_{+,\text{out}}(\mathbf{r}') - \rho_{-,\text{out}}(\mathbf{r}') + \tilde{q}(\mathbf{r}')}{|\mathbf{r} - \mathbf{r}'|}. \quad (2.45)$$

Considering the ion density in a cell V_i around point charge i , we find

$$\rho_{\pm,\text{in}}(\mathbf{r}) = \rho_s \left(1 \mp \sum_{j=1}^M \phi_1(|\mathbf{r} - \mathbf{r}_j|) \right) \approx \rho_s \left(1 \mp \phi_1(|\mathbf{r} - \mathbf{r}_i|) \right), \quad (2.46)$$

where it is assumed that ion density around point charge i is only determined by the contribution to the potential of the point charge i itself. The latter approximation is (apart from the Debye–Hückel approximation) the key assumption to be made in order to obtain (the electrostatic part of) DLVO theory [16, 17], and obviously only holds if the other charges are sufficiently far away from the cell around point i . Under the approximation (2.46) that the second integral in Hamiltonian (2.44) becomes constant with respect to the positions of the charges ρ_{ci} . The total charge \bar{Z} inside the volume around particle i is

$$\begin{aligned} \bar{Z} &= Z + \int_{|\mathbf{r} - \mathbf{r}_i| < a} d\mathbf{r} \rho_{+,\text{in}}(\mathbf{r}) - \rho_{-,\text{in}}(\mathbf{r}) = Z + \int_0^a dr 4\pi r^2 2\rho_s Z \lambda_B \frac{\exp(-\kappa r)}{r} \\ &= Z \exp(-\kappa a) (1 + \kappa a), \end{aligned} \quad (2.47)$$

such that Eq.2.40 can be written, up to a constant, as

$$\beta H[q] = \int_{V_{\text{out}}} d\mathbf{r} \sum_{\alpha=\pm} \rho_{\pm}(\mathbf{r}) \left(\frac{\rho_{\pm}(\mathbf{r})}{\rho_s} - 2 \right) + \frac{1}{2} \int d\mathbf{r} (\rho_+(\mathbf{r}) - \rho_-(\mathbf{r}) + \bar{q}(\mathbf{r})) \phi(\mathbf{r}) \quad (2.48)$$

with the restriction that $\rho_{\pm}(\mathbf{r}) = 0$ as $|\mathbf{r} - \mathbf{r}_i| < a$ and

$$\bar{q}(\mathbf{r}) = \sum_{i=1}^M \bar{Z} \delta(\mathbf{r} - \mathbf{r}_{ci}). \quad (2.49)$$

In Eq. (2.48) we immediately recognise the Hamiltonian for hard-core particles with radius a and charge \bar{Z} that one finds after applying the Debye–Hückel approximation

in Eq. (2.27) to the ion densities in the volume V_{out} outside the particles. By combining Eqs. (2.43) and (2.47) we thus conclude that the effective electrostatic interaction between these hard particles must be given by

$$\beta H = \left(\frac{\bar{Z} \exp(\kappa a)}{1 + \kappa a} \right)^2 \lambda_{\text{B}} \sum_{i < j}^M \frac{\exp(-\kappa R_{ij})}{R_{ij}}, \quad (2.50)$$

which is known as the electrostatic part of DLVO theory. We think this derivation gives a good impression of the physical model behind DLVO theory, which incorporates a low-density approximation for ion-exclusion effects. We have not observed a similar derivation anywhere else in the literature. Note that since DLVO theory is derived from a linearised theory, Eq. (2.50) is valid only in case the Debye-Hückel approximation holds in the volume V_{out} outside the colloidal particles.

In case of strongly charged colloidal particles, a charge-renormalisation procedure could be applied in order to correct DLVO theory for nonlinear behaviour close to the colloidal surfaces. This will extend the range of its applicability [15, 18–21]. In Chapter 5 we will generalise DLVO theory towards colloidal particles with an inhomogenous distribution of charge.

2.7 Spherical cell theory and charge renormalisation

Consider the charge distribution (2.8) of M colloidal particles with associated hard-core potential (2.9). The electrostatic interaction energy between all particles $H[q, \mathcal{V}_{\text{HC}}]$ that follows from evaluating Eq. (2.27) at its minimum w.r.t. the ion densities $\rho_{\pm}(\mathbf{r})$ can be approximated by $H[q, \mathcal{V}_{\text{HC}}] \approx MH_1[q_1]$, with $H_1[q_1]$ the Hamiltonian of one of the particles, placed at the center of a spherical cell volume $V_1 = \frac{4}{3}\pi R^3$, with radius R . The latter volume is such that the summed volume of all cells equals the system's volume, $V_1 = m^{-1}$, with $m \equiv M/V$ the colloidal density, and global charge neutrality demands the individual cells to be charge neutral as well. This reduces the problem to solving the nonlinear PB equation just outside one colloidal particle, which is known as the spherical Wigner-Seitz spherical cell model, introduced by Alexander *et al.* in 1984 [18]. The ion densities and electrostatic potential in this model become rotationally symmetric and the PB equation with boundary conditions takes the form

$$\partial_r^2 \phi(r) + \frac{2}{r} \partial_r \phi(r) = \kappa^2 \sinh \phi(r) \quad \text{if } r \geq a. \quad (2.51)$$

$$\partial_r \phi(r)|_{(r=a)} = -Z\lambda_{\text{B}}/a^2; \quad \partial_r \phi(r)|_{(r=R)} = 0, \quad (2.52)$$

where the second boundary condition implies charge neutrality. For the PB equation in spherical symmetry there is no known general analytic solution available but it can be solved almost instantly, with very high precision, on a desktop computer.

A very useful application of Wigner-Seitz spherical cell theory is that it enables one to calculate renormalised charges Z^* and screening parameters $\tilde{\kappa}$, which can be used to correct the Debye-Hückel approximation in DLVO-theory. After one finds the electrostatic potential that solves Eqs. (2.51) and (2.51), one linearises Eq. (2.51) around the obtained potential at the cell boundary $\tilde{\phi} = \phi(R)$, such that the right-hand part of the PB equation becomes

$$\sinh \phi(r) = \sinh \tilde{\phi} + \cosh \tilde{\phi} (\phi(r) - \tilde{\phi}) + \mathcal{O} \left((\phi(r) - \tilde{\phi})^2 \right) \quad (2.53)$$

The effective screening parameter can be defined as $\tilde{\kappa}^2 = \kappa^2 \cosh \tilde{\phi}$ and one finds the linearised PB equation

$$\partial_r^2 \phi_l(r) + \frac{2}{r} \partial_r \phi_l(r) = \tilde{\kappa}^2 \phi_l(r) - \tilde{\kappa}^2 (\tilde{\phi} - \tanh \tilde{\phi}). \quad (2.54)$$

By matching the electric field and the potential with the solution of the nonlinear problem, $\phi_l(R) = \tilde{\phi}$ and $\partial_r \phi_l(r)|_{(r=R)} = 0$, the solution of the linearised differential equation (2.54) equals the full nonlinear solution far away from the particle but will start deviating as one gets closer to the colloidal surface. The solution to the linearised equation is

$$\phi_l(r) = \tilde{\phi} + \tanh \tilde{\phi} \left(\frac{\tilde{\kappa}R + 1}{2\tilde{\kappa}r} \exp(\tilde{\kappa}r - \tilde{\kappa}R) + \frac{\tilde{\kappa}R - 1}{2\tilde{\kappa}r} \exp(\tilde{\kappa}R - \tilde{\kappa}r) - 1 \right). \quad (2.55)$$

The associated linearised charge follows from $Z^* = -a^2 (\partial_r \phi_l(r))_{r=a} / \lambda_B$, which reads

$$Z^* = \frac{\tanh \tilde{\phi}}{\tilde{\kappa} \lambda_B} \left\{ \left(\tilde{\kappa}^2 a R - 1 \right) \sinh(\tilde{\kappa}R - \tilde{\kappa}a) + (\tilde{\kappa}R - \tilde{\kappa}a) \cosh(\tilde{\kappa}R - \tilde{\kappa}a) \right\}. \quad (2.56)$$

It follows from Poisson-Boltzmann theory that the charge-renormalisation procedure can be written in terms of only 3 independent parameters, for example κa , κR , and $y = Z \lambda_B / (\kappa a^2)$ (as in Eq. (2.37)). The renormalised charge then follows as $y^* = Z^* \lambda_B / (\kappa a^2)$. By using these parameters it is possible to show all important features of charge renormalisation for $\kappa R \gg \kappa a$ in a single graph, as Fig. 2.1 shows. We have not observed a graphical representation that is similar to Fig. 2.1 in the literature, although the charge-renormalisation procedure itself has been described by many other authors, e.g. [15, 18–21]. The figure shows that renormalisation is only significant for $y > 1$, such that y can be used as a nonlinearity parameter. The horizontal asymptotes show that y^* approaches a constant as a function of very large κa . This is the planar limit, where the curvature of the colloid becomes unimportant. On the other hand, the vertical asymptotes in Fig. 2.1 indicate that y^* also approaches a constant as a function of very large y : the renormalised charge saturates at a value that is determined by κa . There is no analytical expression for the saturation value of y^* as a function of κa , however it follows from Eqs. (2.36) and (2.37) that within planar geometry ($\kappa a \gg 1$) the renormalised charge saturates at $y^* = 4$. The vertical asymptotes in Fig. 2.1 furthermore show that the saturation value of y^* increases for smaller κa .

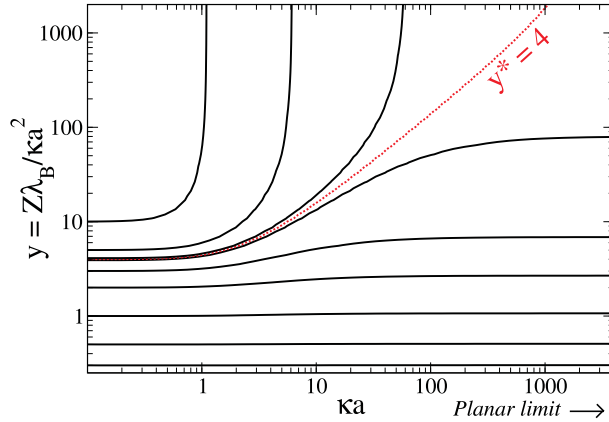


Figure 2.1: Charge renormalisation for dilute systems: a contour plot of the dimensionless renormalised charge $y^* = Z^*\lambda_B/(\kappa a^2)$ as a function of the bare charge and the relative colloidal radius κa for cell size $\kappa R - \kappa a \gg 1$. The contour values are given by the intersections of the line with the left y-axis. The dotted line corresponds $y^* = 4$, which is the maximal renormalised charge for a single charged surface in planar geometry.

2.8 Discussion

Density functional theory (DFT) allows us to calculate the electrostatic energy of a charge configuration without an explicit consideration of the degrees of freedom of the solvent and the ions in the electrolyte. It enables us to calculate the relation between the surface charge density and the electrostatic potential throughout the system, and this relation can be used to find the ion-density profiles in the system. Within a mean-field approximation and for low ion densities the DFT description reduces to Poisson-Boltzmann (PB) theory, which leads generally to a non-linear differential equation for the electrostatic potential. The crucial step in finding the electrostatic energy of a charge configuration is therefore solving the PB equation within the particular geometry of the system. Although there is no general analytic solution for the PB equation, in some geometries a solution exists. Most notably is the planar geometry. In Chapter 3 we will calculate the electrostatic energy that is needed to charge flat electrodes in water, and vary the salt concentration at constant charge to show that energy in principle can be *reversibly* extracted from a salinity gradient. The main focus of the remainder of the thesis will be on spherical colloidal particles. As we saw, the (electrostatic part of the) DLVO equation can be used to calculate the effective electrostatic energy of a configuration of homogeneously charged particles. However, DLVO theory is only valid in case the surface potential is small with respect to the thermal voltage, $k_B T/e \approx 25.6$

mV. A charge renormalisation procedure can be applied in case of stronger charged particles. In Chapters 5 and 6 we will generalise the DLVO interaction and charge renormalisation to inhomogeneously charged particles and in Chapter 8 we will introduce a simple and proper method to account for the fact that the charge itself actually originates from a chemical equilibrium with the electrolyte and therefore can not always be regarded as constant, leading to induced inhomogeneities in the surface charge density.

Chapter 3

Reversible ‘Blue energy’ by cyclic double-layer (de-)compression

Abstract

*A huge amount of entropy is produced at places where fresh water and seawater mix, for example at river mouths. This mixing process is a potentially enormous source of sustainable energy, provided it is harvested properly, for instance by a cyclic charging and discharging process of porous electrodes immersed in salt and fresh water, respectively [D. Brogioli, Phys. Rev. Lett. **103**, 058501 (2009)]. Here we employ a modified Poisson-Boltzmann free-energy density functional to calculate the ionic adsorption and desorption onto and from the charged electrodes, from which the electric work of a cycle is deduced. We propose optimal (most efficient) cycles for two given salt baths involving two canonical and two grand-canonical (dis)charging paths, in analogy to the well-known Carnot cycle for heat-to-work conversion from two heat baths involving two isothermal and two adiabatic paths. We also suggest a slightly modified cycle which can be applied in cases that the stream of fresh water is limited.*

3.1 Introduction

Where river water meets the sea, an enormous amount of energy is dissipated as a result of the irreversible mixing of fresh and salt water. The dissipated energy is about 2 kJ per liter of river water, *i.e.* equivalent to a waterfall of 200m [22]. It is estimated that the combined power from all large estuaries in the world could take care of approximately 20% of today’s worldwide energy demand [23]. Extracting or storing this energy is therefore a potentially serious option that our fossil-fuel burning society may have to embrace in order to become sustainable. However, interesting scientific and technical challenges are to be faced. So far pressure-retarded osmosis (PRO) [24–28] and reverse electrodialysis (RED) [28–32] have been the two main and best-investigated techniques in this field of so-called ‘blue energy’, or salinity-gradient energy. In PRO the osmotic pressure difference across a semi-permeable membrane is used to create a pressurised solution from incoming fresh and salt

water, which is able to drive a turbine [24–28]. In RED stacks of alternating cation- and anion-exchange membranes are used to generate an electric potential difference out of a salinity gradient [28–32]. These techniques enable the generation of (electrical) work at the expense of the mixing of streams with different salinity. Actually, PRO and RED can be thought of as the inverse processes of reverse osmosis and electrodialysis, where one has to supply (electrical) work in order to separate an incoming salt-water stream in a saltier and a fresher stream.

The applicability of PRO and RED are currently being explored: a 1–2 kW prototype plant based on PRO was started up in 2009 in Norway [33], and a 5 kW RED device is planned to be upscaled to a 50 kW demonstration project in The Netherlands [34]. Interestingly, the bottleneck to large-scale applications of both these techniques is often *not* the available fuel —there is a lot of fresh and salt water— but rather the very large membranes that are required to operate at commercially interesting power outputs. Tailoring such membranes with a very high transport capacity and minimal efficiency losses due to biofouling requires advanced membrane technology.

Recently, however, a solid-state device *without* membranes was constructed by Brogioli [7], who directly extracts energy from salinity differences using porous carbon electrodes immersed in an aqueous electrolyte. Due to the huge internal surface of porous carbon, of the order of 10^3 m² per gram of carbon, the capacitance of a pair of electrolyte-immersed porous carbon electrodes can be very large, allowing for large amounts of ionic charge to be stored in the diffuse part of the double layers of the electrolytic medium inside the pores [35]. In fact, although the energy that is stored in the charged state of such large-area electrodes is somewhat lower than that in modern chargeable batteries, the power uptake and power delivery of these ultracapacitors is comparable or even larger [35]. The capacitance of these devices not only scales with the contact area between the electrode and the electrolyte, but also with the inverse distance between the electronic charge on the electrode and the ionic charge in the diffuse part of the double layer, i.e. the capacitance increases with the inverse of the thickness of the ionic double layer. As a consequence, the capacitance increases with increasing salinity, or, in other words, the potential increases at fixed electrode charge upon changing the medium from salt to fresh water. This variability of the capacity was used by Brogioli [7], and also more recently by Brogioli *et al.* [36], to extract electric work from salinity gradients without membranes. Although Sales *et al.* showed that the combination of membranes and porous electrodes has some desirable advantages [37], we will focus here on Brogioli's experiment.

The key concept of Ref. [7] is a four-stage cycle ABCDA of a pair of porous electrodes, together forming a capacitor, such that

- (AB) the two electrodes, immersed in sea water, are charged up from an initial state A with low initial charges $\pm Q_A$ to a state B with higher charges $\pm Q_B$;

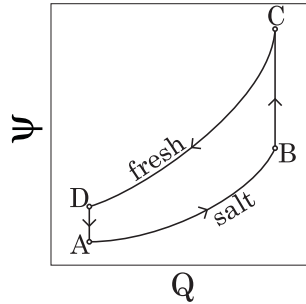


Figure 3.1: A schematic plot of the electrostatic potential as a function of the electrode charge during the four stages in the cycle used by Brogioli [7].

- (BC) the salt water environment of the two electrodes is replaced by fresh water at fixed electrode charges $\pm Q_B$, thereby increasing the electrostatic potential of the electrodes from $\pm\psi_B$ to $\pm\psi_C$;
- (CD) the two highly charged electrodes, now immersed in fresh water in state C, are discharged back to $\pm Q_A$ in state D, and finally
- (DA) the fresh water environment of the electrodes is replaced by salt water again, at fixed electrode charges $\pm Q_A$, thereby lowering the electrode potentials to their initial values $\pm\psi_A$ in state A.

This cycle, during which a net transport of ions from salt to fresh water takes place, renders the salt water fresher and the fresh water saltier —although only infinitesimally so if the reservoir volumes are infinitely large. As a consequence, the ionic entropy has increased after a cycle has been completed, and the associated free-energy reduction of the combined device and the two electrolyte reservoirs equals the electric work done by the device during the cycle, as we will see in more detail below. Brogioli extrapolates an energy production of 1.6 kJ per liter of fresh water in his device [7], equivalent to a waterfall of 160 m, quite comparable to current membrane-based techniques. These figures are promising in the light of possible future large-scale blue-energy extraction.

Below we investigate the (free) energy and the performed work of electrolyte-immersed supercapacitors within a simple density functional that gives rise to a modified Poisson-Boltzmann (PB) equation for the ionic double layers. By seeking analogies with the classic Carnot cycle for heat engines with their maximum efficiency to convert heat into mechanical work given the two temperatures of the heat baths, we consider modifications of Brogioli's cycle that may maximise the conversion efficiency of ionic entropy into electric work given the two reservoir salt concentrations. Our modification does *not* involve the trajectories AB and CD of the cycle where the (dis)charging electrodes are in diffusive contact with an electrolytic reservoir. In fact, we will argue that the grand-canonical trajectories AB and CD at constant ionic chemical potential are the analogue of the isotherms in the Carnot cycle. Rather we consider to modify the constant-charge trajectories BC and DA

(which correspond to isochores in a heat-engine as we will argue) by a continued (dis)charging process of the electrodes at a constant number of ions (which corresponds to an adiabatic (de)compression in the heat engine). In other words, we propose to disconnect the immersed electrodes from the ion reservoirs in BC and DA, treating the salt ions canonically while (dis)charging the electrodes, thereby affecting the ion adsorption and hence the bulk concentration from salty to fresh (BC) and *vice versa* (DA). Finally, we will consider a (dis)charging cycle in the (realistic) case of a finite volume of available fresh water, such that the ion exchange process renders this water brackish; the heat-engine analogue is a temperature rise of the cold bath due to the uptake of heat.

Similar cycles were already studied theoretically by Biesheuvel [38], although not in this context of osmotic power but its reverse, capacitive desalination. The ‘switching step’ in Biesheuvel’s cycle, where the system switches from an electrolyte with a low salt concentration to an electrolyte with a higher salt concentration, appears to be somewhat different from our proposal here, e.g. without a direct heat-engine analogue.

3.2 System and thermodynamics

We consider two electrodes, one carrying a charge Q and the other a charge $-Q$. The electrodes, which can charge and discharge by applying an external electric force that transports electrons from one to the other, are both immersed in an aqueous monovalent electrolyte of volume $2V$ at temperature T . We denote the number of cations and anions in the volume $2V$ by $2N_+$ and $2N_-$, respectively. Global charge neutrality of the two electrodes and the electrolyte in the volume $2V$ is guaranteed if $2N_+ = 2N_-$. If the two electrodes are separated by a distance much larger than the Debye screening length—a condition that is easily met in the experiments of Ref. [7]—then each electrode and its surrounding electrolyte will be separately electrically neutral such that $Q/e = N_- - N_+$, where e is the proton charge and where we assume $Q > 0$ without loss of generality. Note that this ‘local neutrality’ can only be achieved provided $Q/e \leq N_+ + N_- \equiv N$, where the extreme case $Q/e = N$ corresponds to an electrode charge that is so high that all $2N_-$ anions in the volume $2V$ are needed to screen the positive electrode and all $2N_+$ cations to screen the negative one. For $Q/e \leq N$, which we assume from now on, we can use Q and N as independent variables of a neutral system of the positive electrode immersed in an electrolyte of volume V at temperature T , the Helmholtz free energy of which is denoted by $F(Q, N, T, V)$. At fixed volume and temperature we can write the differential of the free energy of the positive electrode and its electrolyte environment as

$$dF = \mu dN + \Psi dQ, \quad (3.1)$$

with $\mu = (\mu_+ + \mu_-)/2$ the average of the ionic chemical potentials μ_{\pm} and Ψ the electrostatic potential of the electrode. The last term of Eq. (3.1) is the electric work *done on* the system if the electrode charge is increased by dQ at fixed N , and hence the electrostatic work *done by* the electrode system is $dW \equiv -\Psi dQ$. Given that F is a state function, such that $\oint dF = 0$ for any cycle, the total work *done by* the system during a (reversible) cycle equals

$$W \equiv \oint dW = - \oint \Psi dQ = \oint \mu dN. \quad (3.2)$$

In order to be able to *calculate* W we thus need explicit cycles *and* the explicit equations-of-state $\mu(Q, N, T, V)$ and/or $\Psi(Q, N, T, V)$, for which we will use a simple density functional theory to be discussed below.

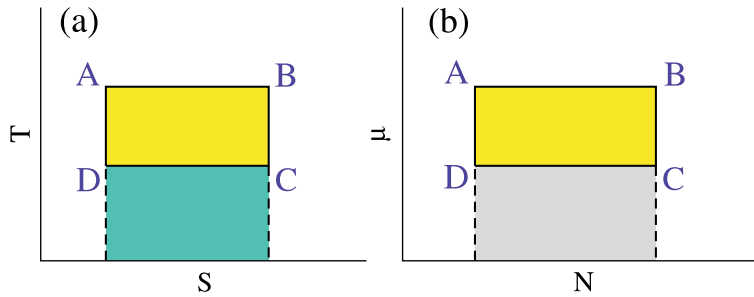


Figure 3.2: A schematic comparison of (a) the entropy-temperature (S, T) representation of the Carnot cycle of a gas that extracts mechanical work from exchanging heat (and thus entropy) between heat baths at two fixed temperatures and (b) the (N, μ) representation (see text) of a cycle to extract electric work from exchanging ions between ionic reservoir at two fixed chemical potentials.

However, before performing these explicit calculations a general statement can be made, because there is an interesting analogy to be made with mechanical work $W_m = \oint p dV$ *done by* a fixed amount of gas at pressure p that cyclically changes its volume V and entropy S (by exchanging heat). In that case the differential of the thermodynamic potential reads $dU = T dS - p dV$ with U a state function denoting the internal energy. Since $\oint dU = 0$ we then find $W_m = \oint T dS$. If the exchange of heat takes place between two heat baths at given high and low temperatures T_H and T_L , it is well known that the most-efficient cycle—the cycle that produces the maximum work per adsorbed amount of heat from the hotter bath—is the Carnot cycle with its two isothermal and two adiabatic (de-)compressions [6]. If we transpose all the variables from the gas performing mechanical work to the immersed electrodes performing electric work, we find $U \Leftrightarrow F$, $S \Leftrightarrow N$, $T \Leftrightarrow \mu$, $V \Leftrightarrow Q$, and $-p \Leftrightarrow \Psi$, where all pairs preserve the symmetry of being both extensive or both intensive. The analogue of high and low temperatures are thus high and low ionic chemical potentials μ_H and μ_L (corresponding to sea and river water, respectively),

the analogue of the isothermal volume change is thus the (dis)charging at constant μ , and the analogue of an adiabatic volume change is (dis)charging at constant N . Therefore, the analogue of the most efficient gas cycle is the electric cycle consisting of (grand)canonical (dis)charging processes. Indeed, the trajectories (AB) and (CD) of the experimental cycle of Ref. [7], as discussed earlier, are of a grand-canonical nature with the electrode in contact with a salt reservoir during the (dis)charging. However, the processes (BC) and (DA) take place at constant Q , i.e. they are equivalent to isochores in a gas cycle, instead of adiabats. Efficiency is thus to be gained, at least in principle, by changing BC and DA into canonical charging processes. Whether this is experimentally easily implementable is, at this stage for us, an open question that we will not answer here.

For the most efficient cycles, which are schematically shown in Fig. 3.2 in the (S, T) and the (N, μ) representation, we can easily calculate the work performed during a cycle. For the mechanical work of the gas one finds $W_m = \Delta S \Delta T$, with $\Delta T = T_H - T_L$ the temperature difference and ΔS the entropy that is exchanged between the heat baths during the isothermal compression and decompression. The analogue for the work W delivered by the electrode is given by $W = \Delta \mu \Delta N$, with $\Delta \mu = \mu_H - \mu_L$ and ΔN the number of exchanged ions between the reservoirs during the grand-canonical (dis)charging processes. This result also follows directly from Eq. (3.2). Below we will calculate ΔN and hence W from a microscopic theory. Moreover, we will also consider several other types of cycles.

In the context of the thermodynamics that we discuss here, it is also of interest to analyse the 'global' energy flow that gives rise to the work W that the immersed porous electrodes deliver per (reversible) cycle. For this analysis it is crucial to realise that the device and the two salt reservoirs at chemical potentials μ_H and μ_L are considered to be at constant temperature T throughout, which implies that they are thermally coupled to a heat bath (that we call the 'atmosphere' here for convenience) at temperature T . We will show that with every completed cycle, during which $\Delta N > 0$ ions are being transported from the sea to the river water, a net amount of heat $Q > 0$ flows from the atmosphere to the two salt reservoirs, and that $W = Q$ in the limit that the ion clouds do not store potential energy due to multi-particle interactions. This may at first sight contradict Kelvin's statement of the Second Law ("no process is possible whose sole result is the complete conversion of heat into work" [39]), but one should realise that the cycle *also* involves the transport of ions from the sea to the river; the word 'sole' in Kelvin's statement is thus crucial, of course. The analysis is based on the entropy changes ΔS_d , ΔS_H and ΔS_L of the device, the highly-concentrated salt reservoir and the one with low salt concentration, respectively, upon the completion of a cycle. Given that the device returns to its initial state after a complete cycle, its entropy change vanishes and $\Delta S_d = 0$. This implies that the device, at its fixed temperature, does not adsorb or desorb any net amount of heat. During a cycle the 'river' gains ΔN ions, and hence its (Helmholtz or Gibbs) free energy changes by $\Delta F_L = \mu_L \Delta N$, while the 'sea' loses ΔN ions such that $\Delta F_H = -\mu_H \Delta N$. Now the basic identity $F = E - TS$ implies

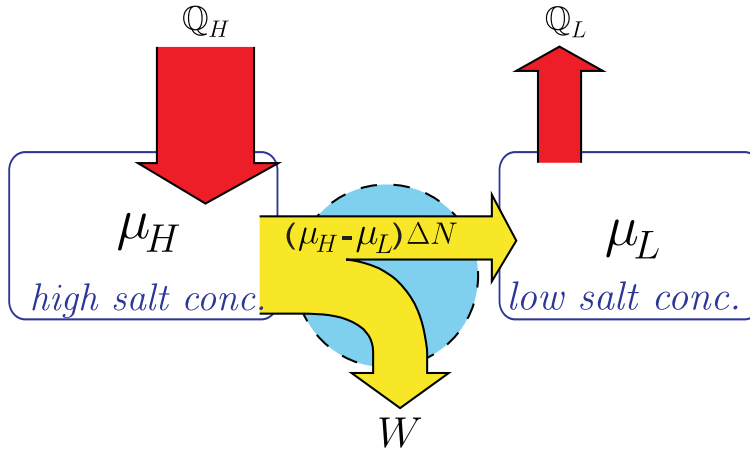


Figure 3.3: A scheme which illustrates the generation of reversible work due to a flow of ΔN particles through the device from a reservoir with a high salt concentration to a reservoir with a low salt concentration. The difference in chemical potential between the two reservoirs enables for the extraction of an amount of reversible work $W = (\mu_H - \mu_L)\Delta N$, which equals the decrease of the net free energy of the reservoirs. The increase of entropy due to this controlled mixing process is caused by an inflow $Q = Q_H - Q_L$ of heat from the atmosphere, which means that the system tends to cool down as it performs work. Note that the division of this heat into two flows of different directions is purely suggestive, as in general there is a transport of heat through the device as well.

that $\Delta F_H = -\epsilon\Delta N - T\Delta S_H$ and $\Delta F_L = \epsilon\Delta N - T\Delta S_L$, where $\epsilon = E/N$ is the average energy (or enthalpy if F denotes the Gibbs free energy) per particle. We assume ϵ to be independent of density, which physically corresponds to the case that there are no multi-particle contributions to the internal energy of the reservoirs, as is the case for hard-core systems or ions treated within Poisson-Boltzmann theory as ideal gases in a self-consistent field. The total energy in the reservoirs therefore remains constant during mixing, such that the entropy changes of the salt reservoirs are $T\Delta S_H = (\mu_H - \epsilon)\Delta N$ and $T\Delta S_L = -(\mu_L - \epsilon)\Delta N$. As a consequence of the global preservation of entropy in the reversible cycle, the ion exchange actually drives a heat exchange whereby the sea extracts a net amount of heat $Q_H = T\Delta S_H$ from the atmosphere, while the river dumps a net amount of heat $Q_L = -T\Delta S_L$ into the atmosphere. Of course the transport of ions itself is also accompanied with a heat exchange in between the reservoirs, the only relevant flow is therefore the net flow of heat out of the atmosphere, which is $Q = Q_H - Q_L = \Delta\mu\Delta N = W$. The energy flow and the particle flow of the device and reservoirs are tentatively illustrated in Fig. 3.3, where one should realise that the distribution of the heat flow from the atmosphere into the sea (Q_H) and the river ($-Q_L$) depends on the heat-flow from river to sea or *vice versa*, which we have not considered here in any detail;

only the net heat flow $Q_H - Q_L$ is fixed by global thermodynamic arguments. This identification of Q with W would have the interesting implication that the conversion of this work into heat again, e.g. by using it to power a laptop, would *not* contribute to (direct) global warming since the released heat has previously been taken out of the atmosphere [40]. It is not clear to us, however, to what extent this scenario is truly realistic and relevant, given that rivers, seas, and the atmosphere are generally *not* in thermal equilibrium such that other heat flows are to be considered. In this study we do not consider the heat fluxes at all, and just consider systems that are small enough for the temperature to be fixed.

3.3 Microscopic model and density functional theory

In order to calculate $\mu(Q, N, T, V)$ and $\Psi(Q, N, T, V)$ of a charged electrode immersed in an electrolyte of volume V , we need a microscopic model of the electrode and the electrolyte. We consider a positively charged porous electrode with a total pore volume V_e , total surface area A , and typical pore size L . We write the total charge of the positive electrode as $Q = e\sigma A$ with σ the number of elementary charges per unit area. The negative electrode is the mirror image with an overall minus sign for charge and potential, see also Fig. 3.4. The volume of the electrolyte surrounding this electrode is $V = V_e + V_o$, with V_o the volume of the electrolyte outside the electrode. The electrolyte consists of (i) water, viewed as a dielectric fluid with dielectric constant ϵ at temperature T , (ii) an (average) number $N_- = (N + Q/e)/2$ of anions with a charge $-e$ and (iii) an (average) number $N_+ = (N - Q/e)/2$ of cations with a charge $+e$. The finite pore size L inside the electrodes is taken into account here only qualitatively by regarding a geometry of two laterally unbounded parallel half-spaces representing the solid electrode, both with surface charge density $e\sigma$, separated by a gap of thickness L filled with the dielectric solvent and an inhomogeneous electrolyte characterised by concentration profile $\rho_{\pm}(z)$. Here z is the Cartesian coordinate such that the charged planes are at $z = 0$ and $z = L$. The water density profile $\rho_w(z)$ is then, within a simple incompressibility approximation $(\rho_w(z) + \rho_+(z) + \rho_-(z))v = 1$ with v a molecular volume that is equal for water and the ions, given by $\rho_w(z) = 1/v - \rho_+(z) - \rho_-(z)$. If the electrolyte in the gap is in diffusive contact with a bulk electrolyte with chemical potentials μ_+ and μ_- of the cations and anions, we can write the variational grand-potential as a functional

$\Omega[\rho_+, \rho_-]$ given by

$$\begin{aligned} \frac{\Omega[\rho_{\pm}]}{Ak_B T} = & \int_0^{L/2} dz \left[\rho_+(z) \left(-1 + \ln \rho_+(z) \Lambda_+^3 - \frac{\mu_+}{k_B T} \right) \right. \\ & + \rho_-(z) \left(-1 + \ln \rho_-(z) \Lambda_-^3 - \frac{\mu_-}{k_B T} \right) \\ & + \rho_w(z) \left(-1 + \ln \rho_w(z) v \right) \\ & \left. + \frac{\phi(z)q(z)}{2} \right]. \end{aligned} \quad (3.3)$$

Here the first two lines denote the ideal-gas grand potential of the two ionic species, with Λ_{\pm} the ionic thermal wavelengths. The third line is the ideal water-entropy, which effectively accounts for ionic excluded volume interactions as it restricts the total local ion concentration to a maximum equal to $1/v$ [41–43]. The last line of Eq. (3.3) denotes the mean-field approximation of the electrostatic energy in terms of the total charge number density $q(z) = \rho_+(z) - \rho_-(z) + \sigma(\delta(z) + \delta(z-L))$ and the electrostatic potential $\psi(z) = k_B T \phi(z)/e$. Note that $\psi(z)$ is a functional of $\rho_{\pm}(z)$ through the Poisson equation $\phi''(z) = -4\pi\lambda_B q(z)$ with $\lambda_B = e^2/\epsilon k_B T$ the Bjerrum length of water, and that $\psi(0) \equiv \Psi$ is the electrode potential. A prime denotes a derivative with respect to z .

The Euler-Lagrange equations $\delta\Omega/\delta\rho_{\pm}(z) = 0$ describes the equilibrium concentration profiles. In a bulk fluid, with $\phi(z) = 0$ and $\rho_+(z) = \rho_-(z) = \rho_s$ we find $\mu_{\pm} \equiv k_B T \ln(\rho_s \Lambda_{\pm}^3/(1-\eta_0))$, with ρ_s the bulk reservoir salt concentration and $\eta_0 = 2\rho_s v$ the ionic packing fraction in the reservoir. In the geometry in between the charged electrodes, the Euler-Lagrange equations combined with the Poisson equation yield the modified Poisson-Boltzmann (PB) equation with boundary conditions (BCs)

$$\phi''(z) = \frac{\kappa^2 \sinh \phi(z)}{1 - \eta_0 + \eta_0 \cosh \phi(z)}; \quad (3.4)$$

$$\phi'(z) \Big|_{z=0} = -4\pi\lambda_B \sigma; \quad (3.5)$$

$$\phi'(z) \Big|_{z=L/2} = 0, \quad (3.6)$$

with $\kappa^{-1} = (8\pi\lambda_B\rho_s)^{-1/2}$ the Debye screening length of the bulk electrolyte. BC (3.5) follows from Gauss' law on the surface of the electrode, and BC (3.6) from charge-neutrality and the symmetry with respect to the midplane of the gap. Note that this equation with accompanying BC's was already studied in Ref. [44–46]. Eq. (3.4) reduces to the standard PB equation if $v = 0$, and the large-gap case $L \rightarrow \infty$ was studied in Ref. [43]. Eq. (3.4) with its BC's (3.5) and (3.6) forms a closed set, and once its solution is found, numerically in general or analytically in the special case that $\eta_0 = 0$ and $\kappa L \rightarrow \infty$, the required equation of state of the electrode potential

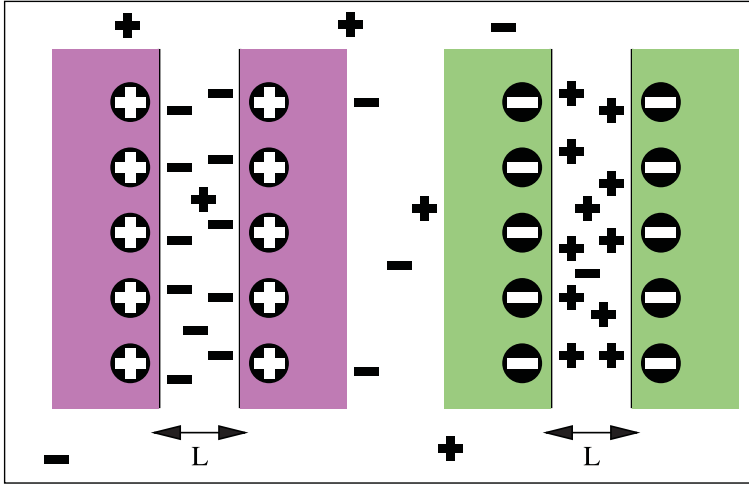


Figure 3.4: A sketch of the two electrodes under consideration, one positively charged and the other one negatively charged, both in contact with an electrolyte with a compensating ionic charge. The porosity of the electrodes is modeled by a slit of width L filled with electrolyte in between two solid half spaces with surface charge density $e\sigma$ for the positive electrode and $-e\sigma$ for the negative one, as represented by the encircled plus and minus signs. The ions in the gap, represented by bare plus and minus signs, are free to migrate throughout the pores and also to the volume outside the electrodes towards the other electrode.

follows from $\Psi(\rho_s, \sigma) = k_B T \phi(0)/e$. Moreover, the equilibrium density profiles can be used to calculate the cationic and anionic adsorption, i.e. the excess number of ions per unit surface area, defined by

$$\Gamma_{\pm}(\sigma, \rho_s) = \int_{z=0}^{z=L/2} dz \left(\rho_{\pm}(z) - \rho_s \right). \quad (3.7)$$

Note that we integrate the profile up to $z = L/2$ as required, and that our 'local charge neutrality' assumption implies that $\sigma = \Gamma_{-}(\sigma, \rho_s) - \Gamma_{+}(\sigma, \rho_s)$. Interestingly, the total surface excess of ions, defined by

$$\Gamma(\sigma, \rho_s) = \Gamma_{+}(\sigma, \rho_s) + \Gamma_{-}(\sigma, \rho_s), \quad (3.8)$$

is related to the total number of ions in the volume $V = V_e + V_o$ by

$$N = 2\rho_s V + A\Gamma(\rho_s, \sigma). \quad (3.9)$$

Below we will use expression (3.7) and (3.8) for $\Gamma(\rho_s, \sigma)$ to calculate $N(\rho_s, \sigma)$ from Eq. (3.9), or to calculate $\rho_s(N, \sigma)$ by solving Eq. (3.9) for ρ_s at given N and σ .

Before discussing our numerical results, it is useful to consider the limiting case $\kappa L \gg 1$ and $\eta_0 \ll 1$, which is in fact the classic Gouy-Chapman (GC) problem of a single, planar, charged wall in contact with a bulk electrolyte of point ions. In this case the PB equation can be solved analytically [9, 47], and the resulting total adsorption is given by

$$\begin{aligned} \Gamma_{GC}(\sigma, \rho_s) &= \sqrt{\sigma^2 + \frac{\kappa^2}{4\pi^2\lambda_B^2}} - \frac{\kappa}{2\pi\lambda_B} \\ &= \begin{cases} \frac{\sigma^2}{2\sigma^*}, & \sigma \ll \sigma^*; \\ \sigma, & \sigma \gg \sigma^*, \end{cases} \end{aligned} \quad (3.10)$$

with the crossover surface charge $\sigma^* = \frac{\kappa}{2\pi\lambda_B}$. The crossover behaviour from $\Gamma \propto \sigma^2$ at low σ to $\Gamma = \sigma$ at high σ signifies a qualitative change from the linear screening regime, where the double layers exchange co- for counter ions keeping the total ion concentration fixed (such that Γ is small), to the nonlinear screening regime where counterion condensation takes place. For the alleged most-efficient (dis)charging cycle of current interest, operating between two ionic reservoirs with a high salt concentration $\rho_s = \rho_H$ and a low one $\rho_s = \rho_L$ such that $\Delta\mu = \mu_H - \mu_L = k_B T \ln(\rho_H/\rho_L)$, and for which we argued already that the electric work per cycle reads $W = \Delta N \Delta\mu$, the GC result (3.10) allows for the calculation of the ionic uptake $\Delta N = A(\Gamma(\rho_H, \sigma_B) - \Gamma(\rho_H, \sigma_A))$ during the grand-canonical charging from a low charge density σ_A to a high one σ_B . In the limit of highly charged surfaces we thus find $\Delta N = A(\sigma_B - \sigma_A)$, and hence the optimal work per unit area within the GC limit reads

$$\frac{W_{GC}}{A} = k_B T (\sigma_B - \sigma_A) \ln \frac{\rho_H}{\rho_L} \quad \text{for } \sigma_A \gg \sigma^*. \quad (3.11)$$

With the typical numbers $\sigma_B - \sigma_A$ of the order of nm^{-2} , $A = 10^3 \text{ m}^2$ per gram of porous carbon, and $\rho_H/\rho_L = 100$ one arrives at $W_{GC} = 10 \text{ J}$ per gram of carbon. Interestingly, this is substantially higher than Brogioli's experimental findings of only $\approx 20 \text{ mJ/gram}$ per cycle. We will discuss this difference below. The GC limit also yields an analytic expression for the surface potential Ψ_{GC} given by

$$\frac{e\Psi_{GC}}{k_B T} = 2 \operatorname{arcsinh} \left(\frac{\sigma}{\sigma^*} \right) \simeq \begin{cases} \frac{\sigma}{2\sigma^*}, & \sigma \ll \sigma^*; \\ 2 \ln \frac{2\sigma}{\sigma^*}, & \sigma \gg \sigma^*. \end{cases} \quad (3.12)$$

With typical Debye lengths $\kappa^{-1} \simeq 1 \text{ nm}$ and $\lambda_B = 0.72 \text{ nm}$ we find for the typical crossover surface charge density $\sigma^* \simeq 0.2 \text{ nm}^{-2}$, which corresponds to a surface potential $\Psi \simeq 50 \text{ mV}$. For completeness we also mention the differential capacitance $C = dQ/d\Psi$ of an immersed electrode, which within the GC limit was already written

by Chapman [48] as

$$\frac{C_{GC}}{A} = \left(\frac{1}{e} \frac{d\Psi_{GC}}{d\sigma} \right)^{-1} = \frac{\kappa\epsilon}{4\pi} \cosh \left[\frac{e\Psi}{2k_B T} \right], \quad (3.13)$$

which corresponds to a two-plate capacitor with spacing $\kappa^{-1}/\cosh(e\Psi/(2k_B T))$ in a dielectric medium characterised by its relative dielectric constant ϵ . This result shows that the capacity indeed increases with the salt concentration, in agreement with observations that the electrode potential rises at fixed charge upon desalinating the surrounding water [7].

Useful insights can be obtained from these analytic GC expressions. Moreover, practical linear approximations [49, 50] and even (almost) analytical solutions [16, 17, 51, 52] for the PB equation exist in the case of small pore size L . Nevertheless, the pointlike nature of the ions gives rise to surface concentrations of counterions that easily become unphysically large, e.g. far beyond 10M for the parameters of interest here. For this reason we consider the steric effects through the finite ionic volume v and the finite pore size L below, at the expense of some numerical effort.

3.4 Numerical results

The starting point of the explicit calculations is the numerical solution of Eq. (3.4) with BC's (3.5) and (3.6) on a discrete z -grid of 5000 equidistant points on the interval $z \in [0, L/2]$, which we checked to be sufficient for all values of κL that we considered. Throughout the remainder of this text we set $v = a^3$ with $a = 0.55$ nm, which restricts the total local ion concentration $\rho_+(z) + \rho_-(z)$ to a physically reasonable maximum of 10 M. The Bjerrum length of water is set to $\lambda_B = 0.72$ nm.

We first consider a positive electrode immersed in a huge ($V \gg V_e$) ionic bath at a fixed salt concentration ρ_s , such that the ions can be treated grand-canonically. In Fig. 3.5 we plot (a) the electrode potential Ψ and (b) the total ion adsorption Γ , both as a function of the electrode charge number density σ , for three reservoir salt concentrations $\rho_s = 1, 10, \text{ and } 100$ mM from top to bottom, where the full curves represent the full theory with pore size $L = 2$ nm, the dashed curves the infinite pore limit $\kappa L \gg 1$, and the dotted curve the analytic Gouy-Chapman expressions (for $\kappa L \gg 1$ and $v = 0$) of Eqs. (3.10) and (3.12). The first observation in Fig. 3.5(a) is that GC theory breaks down at surface charge densities beyond 1 e nm^{-2} , where steric effects prevent too dense a packing of condensing counterions such that the actual surface potential rises much more strongly with σ than the logarithmic increase of GC theory (see Eq. (3.12)). This rise of the potential towards $\simeq 1$ V may induce (unwanted) electrolysis in experiments, so charge densities exceeding, say, 5 e nm^{-2} should perhaps be avoided. A second observation is that the finite pore size L hardly affects the $\Psi(\sigma)$ relation for $\sigma > 1 \text{ nm}^{-2}$, provided the steric effects are taken into account. The reason is that the effective screening length is substantially smaller

than L in these cases due to the large adsorption of counterions in the vicinity of the electrode. A third observation is that the full theory predicts, for the lower salt concentrations $\rho_s = 1$ and 10 mM, a substantially larger Ψ at low σ , the more so for lower ρ_s . This is due to the finite pores size, which is *not* much larger than κ^{-1} in these cases, such that the ionic double layers must be distorted: by increasing Ψ a Donnan-like potential is generated in the pore that attracts enough counterions to compensate for the electrode charge in the small available volume. Interestingly, steric effects do *not* play a large role for $\Gamma(\sigma)$ in Fig. 3.5(b), as the full curves of the full theory with $\nu = a^3$ are indistinguishable from the full theory with $\nu = 0$. The finite pore size appears to be more important for $\Gamma(\sigma)$, at least at first sight, at low σ , where Γ_{GC} appears substantially lower than Γ from the full calculation in the finite pore. However, this is in the linear regime where the adsorption is so small that only the logarithmic scale reveals any difference; in the nonlinear regime at high σ all curves for Γ coincide and hence the GC theory is accurate to describe the adsorption.

We now consider the (reversible) Ψ - σ cycle ABCDA shown in Fig. 3.6(a), for an electrode with pore sizes $L = 4$ nm that operates between two salt reservoirs at high and low salt concentrations $\rho_s = \rho_H = 0.6$ M (sea water) and $\rho_s = \rho_L = 0.024$ M (river water), respectively, such that $\Delta\mu/k_B T = 3.3$. For simplicity we set $V_o = 0$ such that the total electrolyte volume equals the pore volume $V_e = AL/2$. The trajectory AB represents the charging of the electrode from an initial charge density $\sigma_A = 1$ nm $^{-2}$ to a final charge density $\sigma_B = 2$ nm $^{-2}$ at $\rho_s = \rho_H$, which involves an increase in the number of ions per unit area $\Delta N/A = \Gamma(\sigma_B, \rho_H) - \Gamma(\sigma_A, \rho_H) = 0.7$ nm $^{-2}$ using Eqs. (3.8) and (3.9) which we calculate numerically with (3.7). The trajectory BC is calculated using the fixed number of particles in state B, $N = N_B = 2\rho_H V + A\Gamma(\rho_H, \sigma_B)$, calculating a lower and lower value for ρ_s for increasing σ 's using Eq. (3.9) until $\rho_s = \rho_L$ at $\sigma = \sigma_C = 2.81$ nm $^{-2}$. Then the discharging curve CD, at fixed $\rho_s = \rho_L$ is traced from surface charges σ_C down to $\sigma_D = 1.97$ nm $^{-2}$ for which $\Gamma(\sigma_D, \rho_L) - \Gamma(\sigma_C, \rho_L) = -\Delta N/A$, i.e. the discharging continues until the number of expelled ions equals their uptake during the charging process AB. The final trajectory, DA, is characterised by the fixed number of particles in state D (which equals that in A), and is calculated by numerically finding higher and higher ρ_s -values from Eq. (3.9) for surface charges σ decreasing from σ_D to σ_A , where $\rho_s = \rho_H$ at $\sigma = \sigma_A$ such that the loop is closed. Note that all four trajectories involve numerical solutions of the modified Poisson-Boltzmann problem and some root-finding to find the state points of interest, and that the loop is completely characterised by ρ_H , ρ_L , σ_A , and σ_B . Fig. 3.6(b) shows the concentration profiles of the anions (full curve) and cations (dashed curves) in the states A, B, C, and D, (i) showing an almost undisturbed double layer in A and B that reaches local charge neutrality and a reservoir concentration $\rho_{\pm}(z) = \rho_H$ in the center of the pore, (ii) an increase of counterions at the expense of a decrease of coions in going from B to C by a trade off with the negative electrode, accompanied by the saturation of counterion concentration at 10 M close to the electrode in state C and the (almost) complete absence of co-ions in the low-salt states C and D, and (iii) the trading of

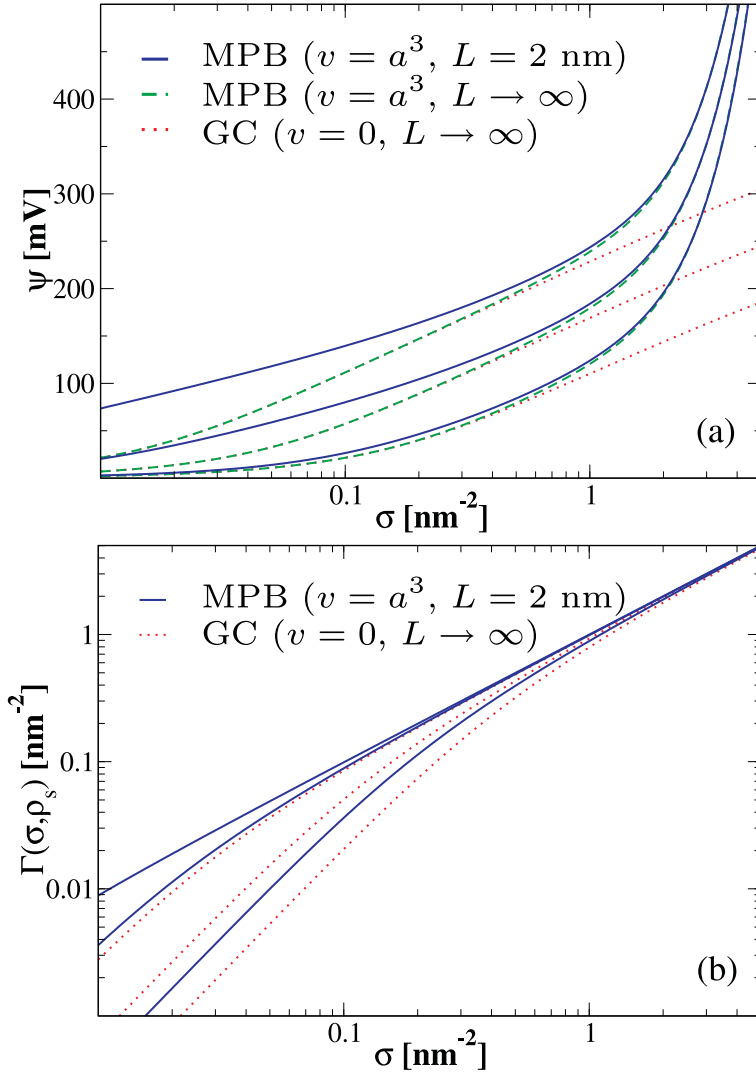


Figure 3.5: (a) The surface potential Ψ and (b) the ionic adsorption Γ , both as a function of the surface charge density σ , for a porous electrode with a pore size $L = 2$ nm immersed in an aqueous electrolyte of monovalent cations and anions at reservoir salt concentrations $\rho_s = \{1\text{mM}, 10\text{mM}, 100\text{mM}\}$ from top to bottom. The labels denote results stemming from the modified Poisson-Boltzmann (MPB) and Gouy-Chapman theory, with the corresponding molecular volume v and the (finite) pore size L .

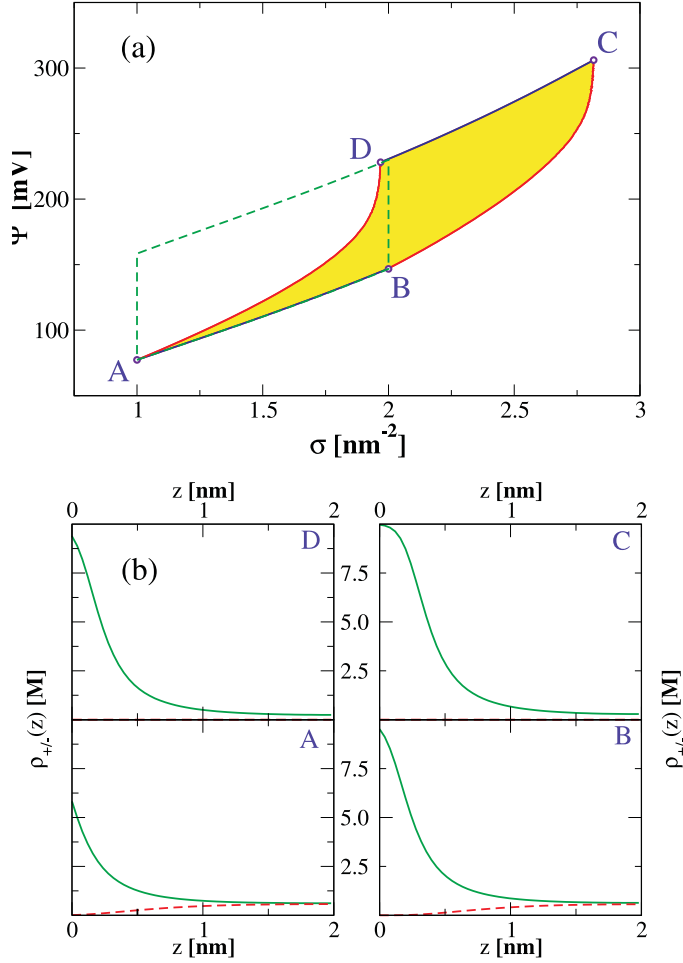


Figure 3.6: (a) A cycle ABCDA of the surface potential Ψ and the surface charge density σ of an electrode with pore size $L = 4$ nm, charging up (AB) in contact with an electrolyte reservoir with a high salt concentration $\rho_s = \rho_H = 0.6\text{M}$ from $\sigma_A = 1$ nm^{-2} to $\sigma_B = 2$ nm^{-2} , discharging (CD) in contact with an electrolyte at low salt concentration $\rho_s = \rho_L = 0.024\text{M}$, while being disconnected from the reservoirs (so with a fixed number of ions) during the additional charging (BC) and discharging (DA). The dashed cycle ABC'D'A, for which the surface charge remains fixed upon the transfer between the two reservoirs, resembles the cycle of the experiments of Ref. [7]. (b) Counter- and co-ion concentration profiles $\rho_{-}(z)$ (full curves) and $\rho_{+}(z)$ (dashed curves), respectively, in the four states A, B, C, and D of (a).

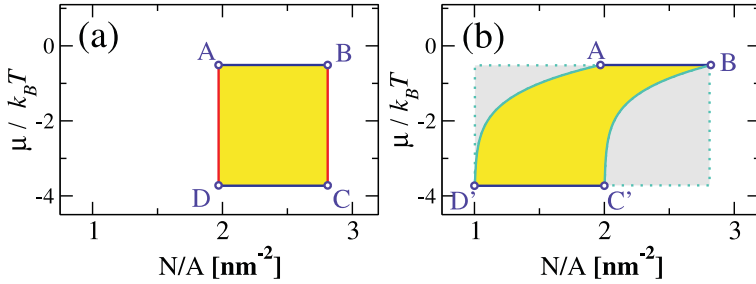


Figure 3.7: The same two cycles as shown in Fig. 3.6(a), but now in the number of ions and chemical potential (N - μ) representation (see text), showing the constant- N trajectories of BC and DA in (a) and a much larger spread in N for the cycle ABC'D'A in (b). Whilst the solid areas represent the work performed during a cycle, the dashed areas in (b) denote losses due to the non-optimal characteristics of the cycle for the given range of N . The enclosed areas give the amount of work that is extracted per cycle and per unit electrode area.

counterions for coions from D to A at fixed overall ion concentration. The work done during the cycle ABCDA follows from either the third or the fourth term of Eq. (3.2), yielding $W/A = 2.3k_B T \text{ nm}^{-2}$ or, equivalently, $W/\Delta N = 3.3k_B T$ for the present set of parameters. The enclosed area of the cycle ABCDA in Fig. 3.6 corresponds to the amount of extracted work (up to a factor (eA)), and equals the net decrease of free energy of the reservoirs.

In order to compare the presently proposed ‘Carnot’ type of cycle ABCDA with the ‘Stirling without a regenerator’ type used in the experiments of Brogioli [7], where ‘isochores’ at constant σ rather than ‘adiabats’ at constant N were used to transit between the two salt baths, we also numerically study the dashed cycle ABC'D'A of Fig. 3.6(a). This cycle has exactly the same trajectory AB characterised by $(\rho_H, \sigma_A, \sigma_B)$ as before. State point C' at ρ_L and $\sigma_{C'} = \sigma_B$ has, however, a much smaller number of ions $N_{C'} = 2\rho_L V + A\Gamma(\rho_L, \sigma_B)$ than $N_B = N_C$ in state B and C, because its surface charge $\sigma_{C'} < \sigma_C$. Trajectory C'D' at fixed ρ_L is quite similar to CD but extends much further down to $\sigma_{D'} = \sigma_A$, where the number of ions in D' is even further reduced to the minimum value in the cycle $N_{D'}/A = 1.0 \text{ nm}^{-2}$. Finally, at fixed $\sigma_{D'}$ the number of ions increases up to N_A by gradually increasing ρ_s from ρ_L to ρ_H . So also this cycle is completely determined by ρ_H, ρ_L, σ_A , and σ_B . The electric work W' done during the cycle ABC'D'A follows from Eq. (3.2) and reads $W'/A = 3.2k_B T \text{ nm}^{-2}$, which is equivalent to $W'/\Delta N' = 1.8k_B T$ where $\Delta N' = N_{B'} - N_{D'}$ is the number of ions that was exchanged between the two reservoirs during the cycle.

Clearly, $W' > W$, i.e. the Brogioli-type cycle with the ‘isocharges’ BC' and D'A produces more work than the presently proposed ABCDA cycle with canonical trajectories BC and DA. However, the efficiency of ABCDA, defined as $W/\Delta N$, indeed

exceeds the efficiency $W'/\Delta N'$ of the ABC'D'A cycle. This is also illustrated in Fig. 3.7, where the two cycles ABCDA (a) and ABC'D'A (b) are shown in the N - μ representation. Whereas the total area of (b) is larger than that of (a), so $W' > W$ according to Eq. (3.2), the larger spread in $\Delta N'$ compared to ΔN renders the efficiency of (b) smaller. The work W' is therefore less than the decrease of the free energy of the reservoirs combined. The hatched area of Fig. 3.7(b) denotes the work that could have been done with the number $\Delta N'$ of exchanged ions, if a cycle of the type ABCDA had been used.

The fact that $W' > W$ while $W/\Delta N > W'/\Delta N'$ proves to be the case for all charge densities σ_A and σ_B for which we calculated W (of an ABCDA-type cycle) and W' (of an ABC'D'A-type cycle), at the same reservoirs ρ_H and ρ_L and the same pore size L as above. This is illustrated in Table 1, which lists W and W' per unit area and per transported ion for several choices of σ_A and σ_B . The data of Table 1 shows that $W' > W$ by up to a factor 2, while $W/\Delta N > W'/\Delta N'$ by up to a factor of three for $V_o = 0$, and a factor 8 for $V_o = V_e$. We thus conclude that the choice for a particular cycle to generate electric work depends on optimization considerations; our results show that maximum work or maximum efficiency do not necessarily coincide.

Table 1 not only shows the work per area and per ion, but in the last column also $W'/A\Delta\sigma$ with $\Delta\sigma = \sigma_B - \sigma_A$, *i.e.* the work per charge that is put on the electrode during the charging of trajectory AB. Interestingly, in these units the work is comparable to $\Delta\mu = 3.3k_B T$ provided $\sigma_A \gg \sigma^*$, as also follows from Gouy-Chapman theory for highly charged surfaces. Note that the work per transported charge does *not* equal the amount of performed work per transported ion as $\Delta N/A$ is typically much larger than $\Delta\sigma$. Nevertheless, the fact that $W' \simeq \Delta\mu A(\sigma_B - \sigma_A)$ gives us a handle to link our results with the experiments of Brogioli [7]. During the experiment, the charge on the electrodes varies by $\delta Q = Ae(\sigma_B - \sigma_A) \approx 0.25 \text{ mC}$, such that one arrives at an expected work of $6 \mu\text{J}$ per electrode. This agrees reasonably well with the obtained value of $5 \mu\text{J}$ out of the entire system. Unfortunately, the relation between the electrostatic potential and the charge in the experiments differs significantly from that of our theory by at least hundreds of millivolts; at comparable electrostatic potentials the charge density in Brogioli's experiments is almost two orders of magnitude smaller than our theoretical estimates. Therefore a qualitative comparison with the Brogioli-cycle is at this point very hard. The relatively low experimental charge densities clarify the lower amount of work produced per gram of electrode, which was noted earlier in the text. Including the Stern layer may be a key ingredient that is missing in the present analysis [36].

σ_A [nm ⁻²]	σ_B [nm ⁻²]	W/A [k _B T / nm ²]	$W/\Delta N$ [k _B T]	W'/A [k _B T / nm ²]	$W'/\Delta N'$ [k _B T]	$W'/(A\Delta\sigma)$ [k _B T]
1.0	2.0	2.3	3.3	3.2	1.8 – 1.0	3.2
1.0	2.75	4.9	3.3	5.6	2.3 – 1.5	3.2
0.5	1.0	1.1	3.3	1.5	1.0 – 0.5	3.0
0.1	0.55	0.6	3.3	1.1	0.7 – 0.4	2.4

Table 3.1: The work W and W' of cycles ABCDA and ABC'D'A, respectively, as illustrated in Figs.3.6(a) and 3.7, for several choices of surface charges σ_A and σ_B in states A and B, for systems operating between electrolytes with high and low salt concentrations $\rho_H = 0.6$ M and $\rho_L = 0.024$ M, for electrodes with pore size $L = 4$ nm. We converted W and W' to room temperature thermal energy units $k_B T$, and not only express them per unit electrode area A but also per exchanged number of ions ΔN and $\Delta N'$ during the two cycles, respectively. Note that $W/\Delta N$ is a property of the two reservoirs, not of the charge densities of the cycle. Also note that $W'/\Delta N'$ depends on the volume V_o of electrolyte outside the electrodes, here we successively give values for the optimal situation $V_o = 0$ as well as for the situation $V_o = V_e$.

3.5 Limited fresh water supply

Of course many more cycles are possible. The two cycles ABCDA and ABC'D'A considered so far generate electric work out of the mixing of two very large reservoirs of salt and fresh water, taking up ions from high-salt water and releasing them in fresh water. Due to the large volume of the two reservoirs the ionic chemical potentials μ_H and μ_L , and hence the bulk salt concentrations ρ_H and ρ_L in the reservoirs, do not change during this transfer of a finite number of ions during a cycle. However, there could be relevant cases where the power output of an osmo-electric device is limited by the finite inflow of fresh water, which then becomes brackish due to the mixing process; usually there is enough sea water to ignore the opposite effect that the sea would become less salty because of ion drainage by a cycle. In other words, the volume of fresh water cannot always be regarded as infinitely large while the salt water reservoir is still a genuine and infinitely large ion bath. The cycle with a limited fresh water supply is equivalent to a heat-engine that causes the temperature of its cold 'bath' to rise due to the release of rest heat from a cycle, while the hot heat bath does not cool down due to its large volume or heat capacity. Here we describe and quantify a cycle ABCA that produces electric work by reversibly mixing a finite volume of fresh water with a reservoir of salt water.

We consider a finite volume $\Delta V = 0.75V$ of fresh water with a low salt concentration $\rho_L = 0.024$ M, such that the number of ions in this compartment equals $2\rho_L\Delta V$. This fresh water is assumed to be available at the beginning of a (new) cycle; its fate at the end of the cycle is to be as salty as the sea by having taken up $2(\rho_H - \rho_L)\Delta V$ ions from the electrode (which received them from the sea), with $\rho_H = 0.6$ M the salt concentration in the sea. The cycle, which is represented in

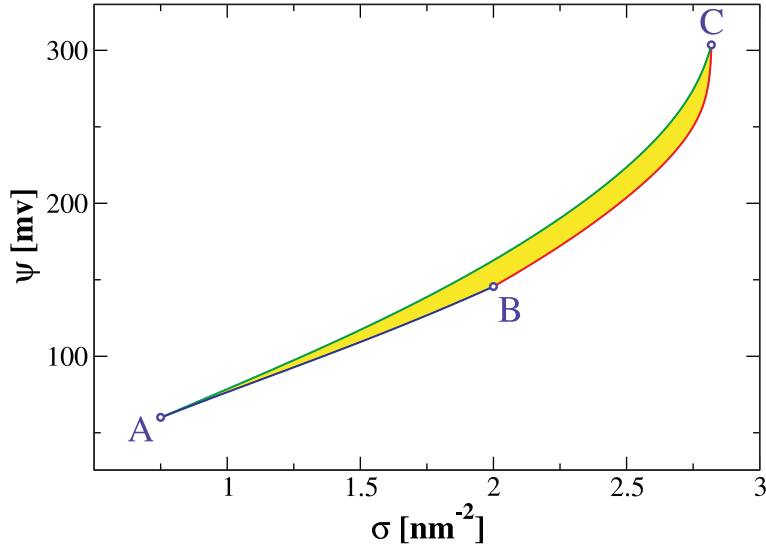


Figure 3.8: Electrode potential Ψ versus electrode charge density σ representation of a charging–discharging cycle ABCA of an electrode with pore size $L = 4$ nm (see text). The trajectory AB represents a grand-canonical charging process during which the system is connected to a ‘sea’ with a fixed high salt concentration $\rho_H = 0.6$ M, the electrolyte in the pores taking up ions. The number of ions during trajectory BC is kept fixed by disconnecting the electrodes from any ionic bath, such that further charging leads to more ionic adsorption at the expense of the bulk concentration, which has reduced to the fresh water concentration $\rho_L = 0.024$ M in C. Trajectory CA describes the discharging of the electrodes in contact with a finite volume $\Delta V = 0.75$ V of initially fresh water at concentration ρ_L , which becomes saltier due to the uptake of electrode–released ions until the sea concentration of salt ρ_H is reached in A.

Fig. 3.8, starts with the electrodes connected to a large volume of sea water at concentration ρ_H , charged up in state A at a charge density $\sigma_A = 0.75$ nm⁻². During the first part AB of the cycle, the electrodes are further charged up until the positive one has taken up $2(\rho_H - \rho_L)\Delta V$ ions in its pores, which fixes the surface charge $\sigma_B = 2.0$ nm⁻² in state B. Then the electrodes are to be disconnected from the sea, after which the charging proceeds in trajectory BC such that the increasing ion adsorption at a fixed total ion number reduces the salt chemical potential down to μ_L (and hence the salt concentration far from the electrode surface down to ρ_L) at $\sigma_C = 2.8$ nm⁻² in state C. The system can then be reversibly coupled to the finite compartment of initially fresh water, after which the discharging process CA takes place such that the released ions cause the fresh water to become more salty, reaching a charge density σ_A when the salt concentration in the compartment of volume ΔV equals ρ_H . The cycle can then be repeated by replacing the compartment ΔV by fresh water

again.

The relation between the surface potential Ψ , the charge density on the electrodes σ , and the ion reservoir concentration ρ_s or the ion number N , was numerically calculated using the modified PB-equation (3.4) with BC's (3.5) and (3.6), combined with the adsorption relation (3.8), with the same parameters $v = a^3$, $a = 0.55$ nm, $L = 4$ nm, and $V = V_e = AL/2$ as before. The enclosed area in Fig. 3.8 gives, using Eq. (3.2), the net amount of (reversible) work W performed during a cycle, which again equals the decrease of the free energy of the salt water reservoir and fresh water volume combined. In fact, this work can be calculated analytically as

$$W = \Delta V[(\rho_H - \rho_L)k_B T - \rho_L(\mu_H - \mu_L)], \quad (3.14)$$

where $\mu_H - \mu_L = k_B T \ln(\rho_H/\rho_L)$. This result agrees with the prediction by Pattle [22] for very small ρ_L . For the parameters of the cycle discussed here, we find $W/\Delta V = 1.2$ kJ per liter of fresh water, or $W/A = 0.45k_B T$ nm⁻². The figures show that the amount of work per ion that is transported is typically smaller than what we found for the Carnot-like cycle, of course.

We may compare this reversible cycle with the one proposed by Biesheuvel for the reverse process, which is called desalination. This cycle is very similar to ours, except that Biesheuvel's switching step from sea-to river water and v.v. is actually an iso- Γ trajectory instead of our iso- N trajectory. This iso-adsorption trajectory does not seem to have a reversible heat engine analogue, as the degree of reversibility depends on the extent to which the electrolyte can be drained out of the micropores before. Nevertheless, we find agreement with the work that must be provided in the case of only a relatively small output volume of fresh water, and the expression found by Biesheuvel exactly equals Eq. (3.14). The point we would like to stress is that irreversible mixing during the switching step can be prevented by introducing a canonical(iso- N) part into the cycle which enables the system to adapt to a new salt concentration in a time-reversible fashion, such that maximal efficiency is preserved.

3.6 Discussion

Although substantial attempts to extract renewable energy from salinity gradients go back to the 1970's, there is considerable recent progress in this field stemming from the availability of high-quality membranes [32] and large-area nanoporous electrodes [53] with which economically interesting yields of the order of 1 kJ per liter of fresh water can be obtained —equivalent to a waterfall of one hundred meter. The key concept in the recent experiments of Brogioli [7] is to cyclically (dis)charge a supercapacitor composed of two porous electrodes immersed in sea (river) water. In this chapter we have used a relatively simple density functional, based on mean-field electrostatics and a lattice-gas type description of ionic steric repulsions, to study the relation between the electrode potential Ψ , the electrode surface charge

density σ , the ion adsorption Γ , the ion chemical potential μ , and the total number of ions N in a (slit-like) pore of width L that should mimic the finite pores of the electrodes. With this microscopic information at hand, we have analysed several cycles of charging and discharging electrodes in sea and river water. By making an analogy with heat engines, for which the most-efficient cycle between two heat baths at fixed temperatures is the Carnot cycle with isothermal and adiabatic (de)compressions, we considered cycles composed of iso- μ and iso- N (dis)charging processes of the electrodes. We indeed found that these cycles are maximally efficient in the sense that the work per ‘consumed’ ion that is transported from the sea to the river water during this cycle is optimal, given the salt concentrations in the river- and sea water. However, although the cycles used by Brogioli, with two iso- μ and two iso- σ trajectories (where the latter are analogous to isochores in the heat-engine) are less efficient per transported ion, the total work of a ‘Brogioli-cycle’ is larger, at least when comparing cycles that share the iso- μ charging in the sea water trajectory. We find, for electrode potentials $\Psi \simeq 100 - 300$ mV and electrode charge densities $\sigma \simeq 1 - 2$ nm⁻³ in electrolytes with salt concentrations $\rho_{\text{H}} = 0.6$ M (sea water) and $\rho_{\text{L}} = 0.024$ M (river water), typical amounts of delivered work of the order of several $k_{\text{B}}T$ per transported ion, which is equivalent to several $k_{\text{B}}T$ per nm² of electrode area or several kJ per liter of consumed fresh water.

Our calculations on the Brogioli type of cycle agree with experiments regarding the amount of performed work per cycle with respect to the variance in the electrode charge during (dis-) charging; each unit charge is responsible for an amount of work that is given by the difference in chemical potential between the two reservoirs. However, the experimental data concerning the electrostatic potential could *not* be mapped onto our numerical data. This could very well be due to the fact that the pore size in the experiments by Brogioli is very small such that ion desolvation, ion polarisability, and image-charge effects may be determining the relation between the surface charge and electrostatic potential. Models which go beyond the present mean-field description are probably required for a quantitative description of this regime. Another ingredient in a more detailed description must involve the finite size of the ions combined with the microscopic roughness of the carbon. The ions in the solvent and the electrons (holes) in the electrode material cannot approach infinitely closely, and the resulting charge free zone can be modeled by a Stern capacitance. Standard Gouy-Chapman-Stern (GCS) theory has successfully been applied to fit charge-voltage curves for porous carbon capacitive cells [36, 54] within the context of osmo-electrical and capacitive desalination devices. Extensions to GCS theory are currently being developed which include finite pore sizes, in order to obtain a physically realistic and simultaneously accurate model of the Stern layer within this geometry.

Throughout this work we (implicitly) assumed the cycles to be reversible, which implies that the electrode (dis)charging is carried out sufficiently slowly for the ions to be in thermodynamic equilibrium with the instantaneous external potential

imposed by the electrodes. This reversibility due to the slowness of the charging process has the advantage of giving rise to optimal conversion from ionic entropy to electric work in a given cycle. However, if one is interested in optimizing the *power* of a cycle, *i.e.* the performed work per unit time, then quasistatic processes are certainly not optimal because of their inherent slowness. Heuristically one expects that the optimal power would result from the trade-off between reversibility (slowness) to optimise the work per cycle on the one hand, and fast electronic (dis)charging processes of the electrodes and fast fluid exchanges on time scales below the relaxation time of the ionic double layers on the other. An interesting issue is the diffusion of ions into (or out of) the porous electrode after switching on (or off) the electrode potential [55, 56]. Ongoing work in our group employs dynamic density functional theory [57–59] to find optimal-power conditions for the devices and cycles studied in this chapter, e.g. focussing on the delay times between the electrode potential and the ionic charge cloud upon voltage ramps.

Acknowledgement We thank Marleen Kooiman and Maarten Biesheuvel for useful discussions.

Charge reversal of porous silica colloids by proton uptake

Abstract

The effect of porosity in Stöber silica colloids is studied using a modified Poisson-Boltzmann theory, with a focus on the case that the porous colloids are suspended in a non-aqueous solvent. The acidity of this solvent is controlled by osmotic contact with an aqueous reservoir of which the pH can be determined. Our numerical results suggest that the colloid charge should be unaffected by the presence of porosity in environments of intermediate acidity. However at sufficiently high acidity a substantial amount of positive charge in the form of absorbed protons changes the net charge of the colloids. A small volume fraction of pores suffices to induce a point of zero charge at $pH \approx 4$. Based on the difference in Donnan potential between the porous medium and the solvent a relation can be constructed that describes the location of the point of zero charge. The accuracy of this relation is confirmed by numerical calculations.

4.1 Introduction

Surfaces of objects that are immersed in a liquid are able to exchange ions with this liquid in order to increase entropy and/or to reduce (electro-)static energy. The nature of this exchange can either be dissociative, in which the surface releases ions into the liquid, or associative, in which the surface adsorbs ions from the liquid. In either case this exchange results in the situation that the object gains an electrostatic charge. For objects in water this charging is typically significant because the high polarity of this particular solvent enables it to contain a high number of ions. In less polar solvents both charging mechanisms are less efficient such that the acquired charge is typically significantly weaker than in water. A colloidal suspension is therefore often more stable against flocculation in water than in organic liquids, as in water the surfaces repel each other more strongly at small distances. The competition between (dissociative) proton release and (associative) protonisation in

metal hydroxide surfaces like rutile, goethite, and silica leads to a point of zero charge (pzc) that varies over a broad pH range between these materials [60]. For all pH below the pzc of these surfaces, their net charge becomes positive due to the predominant protonisation of the surface.

The pzc of silica stays nevertheless a point of discussion as this point is found at very low pH (≈ 2) and its location seems to be dependent on the method used for measuring [61]. Besides, the presence of some particular ion species has proven to be important as well. For example it was shown that the presence of chloride ions shifts the pzc to higher pH [62]. Kosmulski *et al.* even argue that the presence of a pzc is hard to detect [63] in absence of chloride ions.

Labib and Williams [64, 65] investigated the effect of acidity on solids that are immersed in organic liquids instead of water. They discovered that the presence of trace amounts of moisture can be very important for the location of the pzc. They showed that their carefully dried samples displayed a stronger acid-like behaviour than their not-so-dry ones. Accordingly, they introduced three regions along the acidity scale of the liquid: (I) low acidity causes the surface to charge negatively, (II) a range in acidity where the sign of the charge is sensitive to the presence of water, and (III) high acidity causes the surface to charge positively.

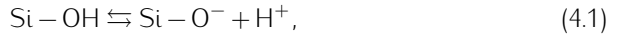
In this chapter, we will introduce a model for the effect of moisture on the electrostatic charge of Stöber silica colloids. These colloids, synthesised by hydrolysing tetraethyl-orthosilicate, are very well-known and have been investigated for many decades now [66]. The porosity of Stöber silica is about 10% [67, 68] and the form of the porous network allows water to move in [69]. Walcarius *et al.*, as well as Labrosse and Burneau [67], found an average pore diameter of 0.3 nm for Stöber silica. Walcarius *et al.* [70] showed that this microporous structure is so fine that ion-exclusion effects take place; large ions cannot enter the microporous structure, whilst the smaller ones (e.g. H^+ , OH^- or Na^+) easily can [71]. This ion-exclusion effect is also well known for crystalline zeolites. It was shown for microporous silica colloids that the selective uptake of alkali anions can increase the amount of negative charge of the particles, although the addition of larger anionic species did not have the same result since these were not able to enter the microstructure [72]. In the case that the added electrolyte is an acid, the size of the hydrated protons is typically (much) smaller than that of the anions. Therefore there could be a tendency for the particles to charge positively due to a presumed selective uptake of positive charge. Using a theoretical framework to calculate the ion densities in equilibrium we will study suspensions of 'wet' porous silica colloids in oil. The influence of acidity on the point of zero charge and the magnitude of the charge in such suspensions is investigated.

4.2 Theory

The dispersion under consideration consists of monodisperse Stöber-silica beads that are dispersed in oil. In our description the oil is a low-dielectric solvent that is immiscible with water. All beads have a radius a , chosen to be in the colloidal size regime which is somewhere in between several nanometers and a micron. The porosity χ of the particles is defined as the fraction of empty volume inside the beads. It is assumed that the pores are shaped like cylinders with diameter D and we propose that water is able to reside inside these pores, even if the colloids are suspended in oil. This water could be a remnant of the particle synthesis, moist collected from the air, or could come from trace amounts of water that is present in the oil. The strong hydrophilicity of the silica ensures that the water that resides in the pores is not replaced by oil. As it will turn out, the containment of water can be important for the net charge of the beads as the wet porous structure might gain a significant amount of charge. This can happen either by charging of the silinol groups inside the pores or by an uptake of ions [72]. Within the model we consider the silica particle being completely wetted by water such that all surface is in contact with water instead of oil. This enables one to calculate all surface chemistry as it is known for a silica-water interface.

4.2.1 Dissociation of silica

Regarding silica-water interfaces, the charging mechanism of the surface groups at pH values well above 2 is mainly dissociative and causes the silica to charge negative. The release of protons from silinol (Si-OH) groups from the surface can be described by



where H^+ denotes a proton and Si-O^- a charged surface group. In water, the corresponding dissociation constant to Eq. (4.1),

$$K_w = \frac{[\text{Si-O}^-][\text{H}^+]}{[\text{Si-OH}]}, \quad (4.2)$$

was measured to be 32nM [60]. Given a local cation (proton) density in the water phase close to the surface, $\rho_{w,+}(\mathbf{r})$, the local charge density $\sigma_w(\mathbf{r})$ of silica can be calculated via

$$\sigma_w(\mathbf{r}) = \sigma_0 \frac{K_w}{\rho_{w,+}(\mathbf{r})}, \quad (4.3)$$

with σ_0 the site density of silinol groups. In Eq. (4.3) it is assumed that the fraction of silinol groups that actually charges is very small compared to the number of available sites, $[\text{Si-OH}] \approx \sigma_0$, such that the charge density is proportional to the inverse of the proton density [73]. The latter turns out to be a safe approximation for the parameters that we consider since the site density of silinol groups on Stöber

silica is high, around 5 sites/nm² [60, 70, 74]. This number agrees well with the assumption that all silicium atoms at the surface carry a silinol group. For the silica-water interface inside the porous silica the same charge mechanism applies as for the outer surface, the porous structure can therefore in principle enable the silica particle to gain more negative charge. However, as we will see next, preferential uptake of protons in the porous structure counteracts the gain of negative charge due to the silinol groups in the pores.

4.2.2 Preferential ion uptake

Due to its high polarity, water is a solvent that reduces the electrostatic self-energy of ions that reside inside it, which is caused by the water molecules that orient their dipole towards or away from charged objects. This makes water a preferential solvent for ions. The polarisability of a solvent can be quantified by the value of the relative dielectric constant, which we will refer to as ϵ_w and ϵ_o for water and oil, respectively. Typically, ϵ_w is an order of magnitude larger than ϵ_o ; ions tend to move from an oil phase to a water phase in order to reduce their self-energy. Therefore the concentration of ions in aqueous parts of a system is in general much higher than in a coexisting oil phase. This is directly related to the well-known fact that salts dissolve typically much better in water than in oil. In units of $k_B T$, the self-energy difference that a cation (+) and an anion (-) experience can be estimated via the Born approximation [9],

$$\beta F_{\pm} = \frac{1}{2a_{\pm}}(\lambda_{B,o} - \lambda_{B,w}), \quad (4.4)$$

where the radii of the (hydrated) ions are denoted by a_{\pm} , and where $\lambda_{B,o} \equiv e^2/(\epsilon_o k_B T)$ and $\lambda_{B,w} \equiv e^2/(\epsilon_w k_B T)$ are the Bjerrum lengths in the oil and water, respectively, with e the elementary charge. The densities of the ion species in the oil phase are determined by the local electrostatic potential $\psi(\mathbf{r})$ and the self-energy differences F_{\pm} via the Boltzmann relation

$$\rho_{o,\pm}(\mathbf{r}) = \rho_w \exp(\mp \beta e \psi(\mathbf{r}) - \beta F_{\pm}), \quad (4.5)$$

where $\beta^{-1} = k_B T$ is the temperature in Boltzmann units and ρ_w is the ion density in bulk water. Due to charge neutrality the salt concentration in bulk oil necessarily becomes $\rho_o = \sqrt{\rho_{o,+}\rho_{o,-}} = \rho_w \exp\left(\frac{-\beta}{2}(F_+ + F_-)\right)$, with corresponding oil-phase Donnan potential

$$\psi_{D,o} = \frac{1}{2e}(F_- - F_+), \quad (4.6)$$

such that the ion densities in this phase can be expressed as

$$\rho_{o,\pm}(\mathbf{r}) = \rho_o \exp(\mp \beta e(\psi(\mathbf{r}) - \psi_{D,o})), \quad (4.7)$$

Because the bulk ion concentration in oil is orders of magnitude smaller than in water, ionic screening will be relatively inefficient; the screening length is much larger than in water. Since the positive ions are typically the smallest ion species, we find that $F_- - F_+ < 0$, such that the Donnan potential of the oil phase (4.6) is negative. This implies that the water-oil interface appears to be positively charged observed from the oil phase, and vice versa that this interface seems to be negatively charged observed from the water phase [75]. Close to oil-water interfaces one observes an excess of negative ions in the oil phase and an excess of positive ions in the water phase. These ions screen the apparent charge of the interface.

The theory above applies to a bulk water phase in contact with a bulk oil phase, each of these two solvents having its own bulk ion concentration and Donnan potential. However, water inside the micropores of the silica must be treated different than bulk water due to the presence of the porous structure. Therefore the interior of the colloid can be regarded as a new solvent species having its own bulk ion concentration and Donnan potential as we will see later. As was shown by Walcarius *et al.* [70, 76], ions with (bare) diameters larger than about 0.3 nm cannot react with the silinol groups inside the porous microstructure, they are too large. In this chapter it is therefore assumed that the anionic species that are present in the system are too large to move into the porous structure, such that cations are the only ions that are able to move from the oil into the micropores and vice versa [77]. The effective cation density inside the colloidal particles can, similarly to Eq. (4.7), be expressed as

$$\rho_{c,+}(\mathbf{r}) = \rho_w \chi \exp(-\beta e \psi(\mathbf{r})). \quad (4.8)$$

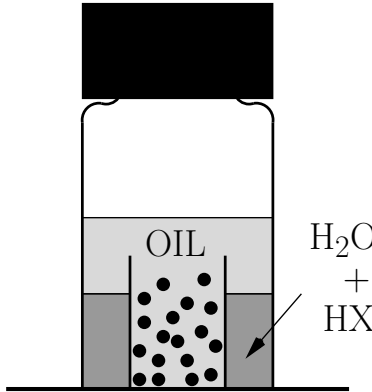


Figure 4.1: A schematic view of the described system. The water reservoir is separated from the oil in the center of the set-up via a glass wall. The colloids, which are suspended in oil at the other side of this wall can be observed from below. The pH of the water is controlled by adding an acid HX to the water reservoirs.

The only source of negative charge inside the colloids is formed by the silinol groups. The density of silinol charge follows from Eq. (4.3) and relates to the electrostatic potential as

$$q(\mathbf{r}) = \frac{\chi \sigma_0}{d} \frac{K_w}{\rho_w \exp(-\beta e \psi(\mathbf{r}))}, \quad (4.9)$$

where $d = V_{\text{pore}}/A_{\text{pore}}$ is the volume to surface ratio of the pores. We estimate the pores to be cylindrical such that $d = D/4$. We remark that, like the exact value for D , this particular choice for the pore geometry is not critical for the results we obtain.

The ion concentration in any part of the system (either in the oil phase or inside the colloids) depends on the total number of ions that is present in the system. Therefore our model in principle asks for a canonical treatment that considers all sources of ions in the system (e.g. due to the dissociation of silinol groups or added acid). This is unfavorable as there could be unknown sources of ions due to for example impurities. However, one can get around this problem by assuming that the oil phase is connected to a water phase of sufficient size that acts as an ion reservoir, see Fig. 4.1. The acidity and therefore the bulk ion concentration in this water reservoir is assumed to be controlled by the addition of some acid HX which dissociates into H^+ and X^- and fixes the bulk ion concentration via $\rho_w = 10^3 N_A 10^{-\text{pH}}$, with N_A Avogadro's constant and ρ_w expressed in m^{-3} . The possibility of the addition of extra salt to this reservoir, like NaCl, that changes the bulk ion concentrations but does not participate in the charging of the silinol groups is not considered here.

4.2.3 Cell-model approximation

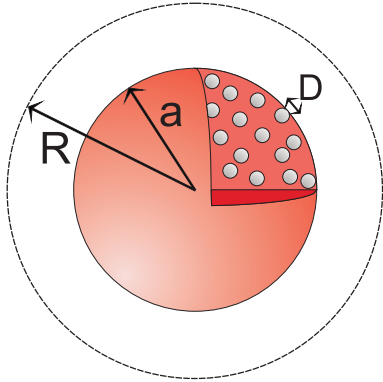


Figure 4.2: In order to find the charge on the porous particle, a spherical cell of radius R is drawn around the colloid with radius a . Note that the pores of diameter D are in fact a lot smaller than pictured above, they actually form a very fine structure inside the colloid.

A Wigner-Seitz spherical cell model is used, as was introduced by Alexander *et al.* in Ref. [18] to find the ion-density profiles both inside and outside the colloid. This is done by defining a spherical cell around each colloid and assuming that all cells are identical and globally charge neutral, see Fig. 4.2. The combined volume of all the cells should equal the volume of the entire system, such that the packing fraction η of the colloids is related to the cell radius via $R = a\eta^{-1/3}$. Because of the spherical shape of the cell it is possible to make the problem rotationally symmetric. However, the porous structure is not rotationally symmetric a priori as the pores have a finite size and induce an inhomogeneity to the interior of the colloid. To be

able to neglect this inhomogeneity, the typical length scale of the porous network inside the colloids must be small compared to the correlation length of electrostatic interactions inside the pores, which is the Debye screening length in water. It can be calculated that this turns out to be the case for Stöber silica. The coordinate r , which is the distance to the center of the colloid, is therefore the only remaining spatial parameter in the theory. The surface and the cell boundary are located at $r = a$ and $r = R$ respectively, as is shown in Fig. 4.2. Continuity of the electric field and charge neutrality of the cell translate to boundary conditions on the electrostatic potential as

$$\psi'(0) = \psi'(R) = 0, \quad (4.10)$$

where $\psi'(r)$ denotes the derivative of the electrostatic potential with respect to r . Since the interior of the colloid effectively consists of a water-silica mixture this part of the cell must be described by a dielectric constant that is in between that of both media. The effective dielectric constant of the mixture is estimated by $\epsilon_{\text{eff}}^{-1} = \chi \epsilon_w^{-1} + (1 - \chi) \epsilon_s^{-1}$. Here ϵ_s and ϵ_w are the dielectric constant of silica and water, respectively. The latter approximation follows from an analysis of a fine mixture in which the interfaces between the two components are perpendicular to the direction of the electric field. In practice the problem is much more complicated, also because the dielectric constant of confined water is much lower than in bulk. However, our results will turn out to be only weakly dependent on ϵ_{eff} , such that a more detailed approximation is not performed here.

The Poisson equation in spherical geometry

$$\psi''(r) + \frac{2}{r} \psi'(r) = \frac{-4\pi e}{\epsilon(r)} [\rho_+(r) - \rho_-(r) - q(r)], \quad (4.11)$$

relates the divergence of the electrostatic potential to the ion densities ρ_{\pm} and the silinol charge density $q(r)$ (4.9). The function $\epsilon(r)$ is a step function which has the value ϵ_{eff} for $r < a$ and ϵ_0 for $r > a$. The associated dielectric interface at the colloidal surface is not described by the Poisson equation in this form. This jump is captured by demanding continuity of the electrostatic potential and by introducing the boundary condition

$$\lim_{r \uparrow a} \epsilon_{\text{eff}} \psi'(r) - 4\pi e \sigma_s(r) = \lim_{r \downarrow a} \epsilon_0 \psi'(r), \quad (4.12)$$

where σ_s is the silinol charge at the colloidal surface ($r = a$), which is given like Eq. 4.3 by

$$\sigma_s = \sigma_0 \frac{K_w}{\rho_+(a)}, \quad (4.13)$$

with the cation density at the surface given by $\rho_+(a) = \rho_w \exp(-\beta e \psi(a))$. In the oil phase, $r > a$, the ion densities are related to the electrostatic potential via $\rho_{\pm}(r) = \rho_w \exp(\mp \beta e \psi(r) - F_{\pm})$. The next section will focus on finding the ion densities both inside and outside the colloid.

4.3 Results and discussion

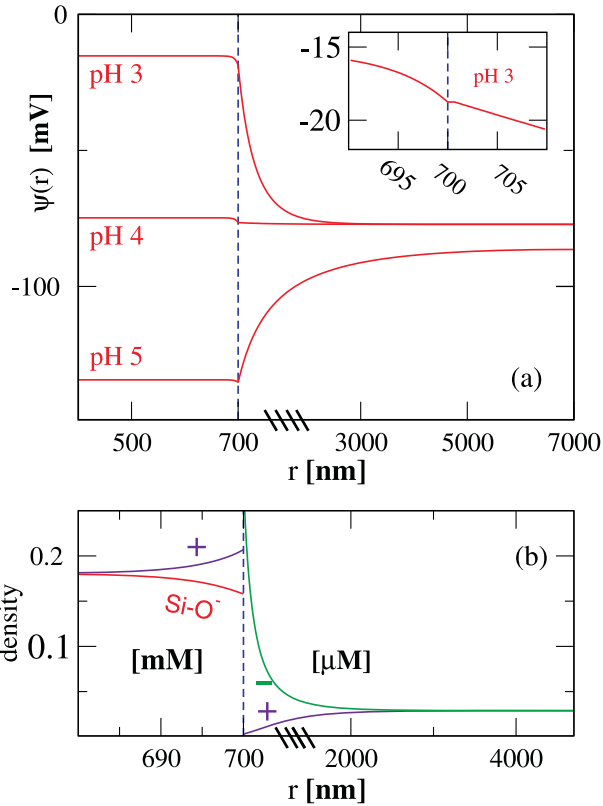


Figure 4.3: (a) The electrostatic potential as a function of the radial coordinate r , plotted for a particle with radius $a = 700$ nm below, around and above the pzc , corresponding to pH 3, 4 and 5, respectively. The inset shows this potential for pH 3 again, now for r close to the interface to demonstrate the relatively thin double layer inside the particle. In (b) the densities of the three different charge generating species (cation/anion/silanol) are shown for pH 3 at both sides of the interface, inside the colloid in mM, outside in μM . Note that in both figures the length scale along the x-axis changes at $r = a$.

Eq. (4.9), (4.8), and (4.11) can be solved numerically with help of the boundary conditions (4.10) and (4.12) in order to find the charge densities and the electrostatic potential everywhere in the Wigner-Seitz cell. The parameters that were used are given in Table 4.1. The colloidal charge Ze follows from the sum of the charge inside the particle and the charge on the outside surface, but can also be found via

η	10^{-3}	ϵ_o	7.5
a	700 nm	σ_0	4.6nm^{-2}
D	0.3 nm	K_w	32 nM
χ	0.10	σ_+	0.25 nm
ϵ_s	4.0	σ_-	0.45 nm
ϵ_w	80.0		

Table 4.1: The values for the parameters that are used in our numerical calculations, unless stated differently. Here η is the colloidal packing fraction, a the colloid radius, D the pore size, χ the pore volume fraction, σ_0 the surface density of silinol groups, K_w the equilibrium constant that describes charging of the silinol groups, σ_{\pm} the ion diameters, and ϵ_s , ϵ_w and ϵ_o the dielectric constants of silica, water and oil, respectively.

Gauss' law,

$$Z = \lim_{r \downarrow a} \frac{-\epsilon_o r^2 \psi'(r)}{e}. \quad (4.14)$$

For an illustrative example of a typical solution for the electrostatic potential we refer to Fig. 4.3(a). The relative small screening length in the colloid phase is due to the water in the pores, and is at most tens of nanometers for the whole range in pH that is investigated here. In contrary, the screening length in the oil phase is very large. The electric field in oil does only decay to zero over distances that are of the order of a micron, as can be seen in Fig. 4.3. The equilibrium (Donnan) potential inside the colloid, $\psi_{D,c}$, at which the colloidal interior is locally charge neutral, observably depends on the pH because the latter determines the proton fugacity. The difference between the Donnan potential inside the colloid and the surrounding oil phase is crucial as it turns out to give a good approximation of the point of zero charge (pzc). If the difference is negative the colloid will be negatively charged, and if it is positive the particle will be positively charged. Equal Donnan potential is found at a pH that is given by

$$\text{pH}_{(\psi_{D,o}=\psi_{D,c})} = -\log_{10} \sqrt{\exp(F_- - F_+) \frac{\sigma_0 K_w}{d 10^3 N_A}}. \quad (4.15)$$

From Eq. (4.15) one finds a pzc at pH 3.9 for the parameters used. However, the latter equation does not take account for the silinol groups on the colloidal surface at $r = a$. This source of negative charge slightly lowers the net charge of the colloid such that the pzc is not exactly found at equal Donnan potential but at a lower pH. The difference in the pzc found by a comparison of Donnan potentials and the pzc found by solving the modified PB equation is however only of the order of 0.1.

Fig. 4.3(b) shows the ion-density profiles at pH 3. As the figure shows, there is no silinol charge in the oil phase and no anionic charge in the colloidal phase. As one expects, deep inside the colloid, the silinol groups do dissociate, although

there is no net transport of counterions away from the pores. The pores therefore stay charge neutral on average; the electrostatic potential is at its Donnan value. Closer to the colloidal surface we observe a layer of higher cation density, which is due to protons that have moved from the oil phase towards the colloid in order to reduce their Born self-energy. The latter can only occur in a layer close to the colloidal surface as the opposite charge species, which are the anions in the oil phase and also the negatively charged colloidal outside, are not so far away here. The electrostatic 'cost' of charge separation can therefore compete with the gain in Born self-energy. It can be concluded from Fig. 4.3(b) that the net charge in the porous volume only resides in a layer close to the surface, having a thickness of several nanometers, which is consistent with the assumption that the charge on many silica surfaces is located in a layer of finite thickness that is easily permeable for some specific ion species [77–78].

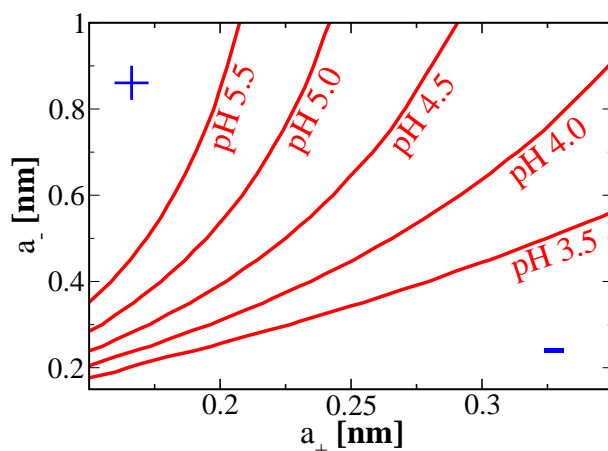


Figure 4.4: The relation between isoelectric point and the (hydrated) ion radii that determine the Born self-energy differences between the oil and the water phase. We assume that the cationic species are always able to move in to the pores, whilst the anions are excluded.

Since charge reversal is driven by (an excess) uptake of protons inside the silica, the self-energy difference that the protons experience by crossing the oil–water interface is of great importance for the location of the pzc. Fig. 4.4 shows the numerical results for the location of the pzc as a function of the cation and anion radii. It demonstrates that also the anion size is of importance as well. The pzc shifts to higher pH for smaller cation radii because of the increase in self-energy difference such that the protons have a greater tendency to enter the silica. Note that a smaller cation shifts the pzc to lower pH as this raises the Donnan potential of the oil phase (4.6).

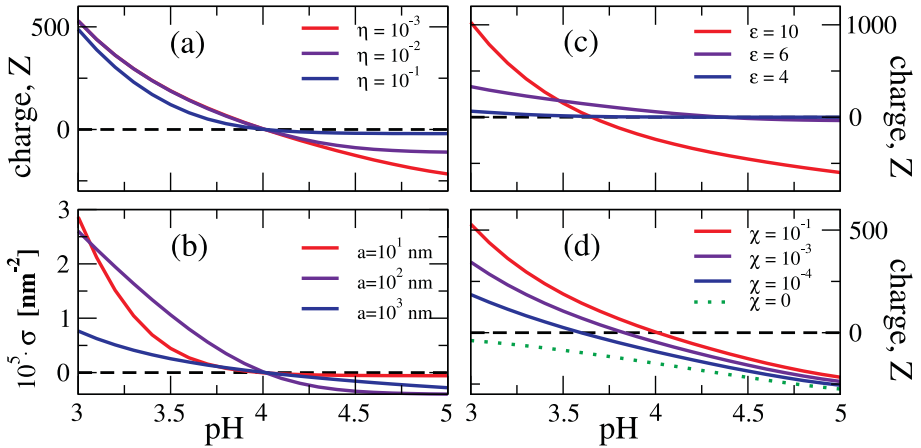


Figure 4.5: Behaviour of the net charge on the silica particle as a function of the pH for (a) various packing fractions η ; (b) three decades in colloidal radius a , showing the charge density $\sigma = Z/(4\pi a^2)$ along the vertical axis; (c) three values of the dielectric constant of the oil phase; and (d) a wide regime in porosity χ , also showing the charge for a non-porous particle as a dotted line. Note that the line $\chi = 10^{-2}$ is not plotted here.

We have argued that the difference in Donnan potential between the porous silica and the oil phase is the main factor that determines the pzc. Therefore, the pzc will not strongly depend on the colloidal density nor on the colloidal radius. Fig. 4.5(a) and (b) confirm this. In (a) we plot the charge for various packing fractions. The effect on the magnitude of the charge is small, however we observe discharging at increasing packing fraction for higher pH. At lower pH, the charge is relatively uninfluenced by the colloidal packing fraction, this is because the ion concentration in the oil phase becomes relatively large such that enhanced ionic screening prevents the colloids from electrostatic interaction with each other. In our Wigner-Seitz cell model this means that the electrostatic potential takes the value of the Donnan potential at the cell's boundary ($r = R$). Fig. 4.5(b) shows the apparent charge density $Z/(4\pi a^2)$ on the colloid for different values of the colloidal radius a . We observe that the highest charge density at both sides of the pzc is expected at intermediate colloid sizes. This optimum is due to a competition between decreasing surface curvature and increasing interparticle distance as a increases while η is kept constant.

In Fig. 4.5(c) and (d) we vary the dielectric constant of the oil and the porosity respectively in order to investigate the dependence of the charge on some of the parameters that can be changed experimentally. By changing the dielectric properties of the solvent we observe (I) that the pzc shifts to lower pH as the dielectric constant of the oil ϵ_0 increases, and (II) the magnitude of the charge (at both sides

of the pzc) increases with ϵ_0 . Both observations can be explained by the higher affinity of ions for the oil phase at increasing ϵ_0 . Observation (I) can be explained by the tendency of the protons to move from the oil phase towards the silica decreases, whilst (II) is more general; the electrostatic energy that is needed to charge a colloid in a more polar medium is less such that higher charges are easier attained.

In Fig. 4.5(d) the porosity is varied, this can be realised experimentally for example by slowing down the growth rate during the Stöber synthesis process [79]. Within the present model we assume that all the pores are accessible for ions in the surrounding oil phase, at least in a layer within tens of nanometers from the surface, as Fig. 4.3(a) shows. It might have been appropriate to introduce an effective porosity that only accounts for pores that are accessible for the cations in the oil phase. In Fig. 4.5(d) we show, however, that the exact value of the porosity is not crucial for the behaviour of the colloids. The figure shows that a small fraction of chargeable pores suffices to find the pzc close to the pH that is predicted by Eq. 4.15, which does not depend on the porosity. The value of χ therefore does affect the pzc, but the dependence is only minor. From Fig. 4.5(d) we observe that the pH shift in the pzc is of the order of 0.1–0.2 if the porosity is changed by a factor 10. The figure tells us that only a very tiny amount of absorbed water is enough to generate a pzc close to pH 4. In order to generate a significant amount of positive charge at a pH below the pzc, a certain amount of porosity is of importance, however the porosity does not play a role for the amount of charge for a pH significantly above the pzc. The latter is limited to pH 7, as the ion species described here only allow for an acidic environment.

4.4 Silica in water

We briefly consider the case that the colloids are suspended in water instead of in oil, such that the Born self-energy difference (4.4) between the oil phase and the silica vanishes. Now, the only mechanism that can generate a pzc is the selective exclusion of anions from the porous silica. By applying Eq. (4.15) using $F_{\pm} = 0$, we find the pzc at pH 2.7, which is close to the alleged value for the pzc of silica in water [60]. Note that proton adsorption to the surface was not included to the model, i.e. no extra chemical equilibrium is added to the calculations. Nevertheless, a reasonable pzc comes out using preferential uptake of protons, which shows that microporosity in Stöber silica particles in water can under certain circumstances compete with ion adsorption at the colloidal surface.

4.5 Discussion

Colloidal Stöber silica is known to have a significant amount of porosity. It was unknown to what extent this porosity could contribute to the net charge of these col-

loids in non-polar solvents. To get a better understanding of how the electrostatic interactions of these colloids are affected one needs to find a relation that describes the density profiles of the different charge-generating species inside the porous structure. A model on the level of Poisson-Boltzmann theory was developed here in order to find the distribution of charges both inside and outside the silica particle. The suspension was assumed to be connected to a water reservoir such that the pH of the system could be defined in a natural way. The pores were assumed to be completely filled with water, which is often a reasonable assumption for experimental situations. We take account for the fact that ions prefer to reside in polar media such as water, and correspondingly find a low and a high screening parameter in the oil phase and the porous silica, respectively. Although the porosity significantly increases the amount of chargeable silinol groups the particle's net charge turns out not be influenced by the porosity at higher pH values, ($\text{pH} > 5$). However at lower pH protons which enter the porous network in order to reduce their self-energy do affect the net amount of charge. This gain of positive charge may become dominant over the dissociation of the silinol groups, such that a point of zero charge is induced. This point was found to be somewhere close to 4.0 for the parameters used in this study. An analytic expression (4.15) can be obtained to estimate the location of the pzc. It turns out that this equation does not depend on the parameters χ and D . Numerical data indeed confirms a very weak dependence on the amount of porosity. The reported value in the literature for χ , which is about 10%, turns out to be high enough to get good agreement between the analytical approximation and the more accurate numerical results. The case that the silica colloids are suspended in water is considered briefly as well. Although the Born self-energy difference that the ions experience vanishes, a possible exclusion of anions from the porous network could still trigger a charge reversal. For the parameters used in this research, this point is found at pH 2.7. Although the latter pH is low, it shows that proton adsorption might be able to compete with proton adsorption at the silinol groups as they can both trigger a pzc at low pH.

Acknowledgement We thank Peter van Oostrum and Alfons van Blaaderen for sharing their preliminary experimental results on silica particles in CHB with us, which inspired the study reported in this chapter.

Chapter 5

Electrostatic interactions between Janus particles

Abstract

We investigate the range in parameter space where Poisson-Boltzmann theory can be used to accurately describe the electric double layer around a perfectly antisymmetric spherical Janus particle in a dielectric medium with added salt. The screening-ion density profiles, obtained by ensemble averaging in Primitive Model NVT Monte Carlo simulations, form the basis for comparison. The electrostatic dipole is the most important mode regarding the ion-density profiles around these Janus particles. We derive equations that describe the colloid-colloid interactions as a function of the monopole and the dipole moment of these particles. The latter can be regarded as an extension of the electrostatic part of DLVO theory towards the interaction of Janus particles.

5.1 Introduction

In this chapter we will investigate the applicability of Poisson-Boltzmann (PB) theory to inhomogeneously charged spherical particles, in particular ‘Janus’ particles, with a differently charged upper- and lower hemisphere. As is known for homogeneously charged particles and surfaces, the regime of applicability of PB to colloidal systems includes a wide range of solvents, ion concentrations and charges [80]. PB theory is therefore the most common method to calculate electrostatic interactions between colloids. Often, the effective interaction that follows from a PB analysis can be approximated by a DLVO sum, as we saw in Chapter 2, making calculations even easier. However, PB theory is based on a mean-field approach, which means in particular that direct ion-ion correlations are ignored. A well-known breakdown of PB theory is therefore the case that the electrolyte contains multivalent ions [81–84]. In this situation the direct ion-ion correlations easily becomes dominant as the pair-interaction energy scales quadratically with the valency of the ions. It turns out that even attractions between like-charged colloids then become possible [85]. Other discrepancies between PB and experiments are often induced by additional

(dielectric) properties of the solvent molecules and the ions. For example, recently it was shown that a difference in polarisability of the solvent molecules and the ions leads to unexpected behaviour at high colloid charges. Close to the colloidal surface the abundance of ions results in a local polarisability that is significantly different from the bulk solvent, which can be very important for the shape and thickness of the double-layer in aqueous systems [86]. Other possible important effects include steric interactions and non-bulk behaviour of solvents close to surfaces. All these could especially be important in aqueous solvents. Several other approaches than classical PB exist [20, 87–95], among which are modifications of the traditional PB theory accounting for finite ion size.

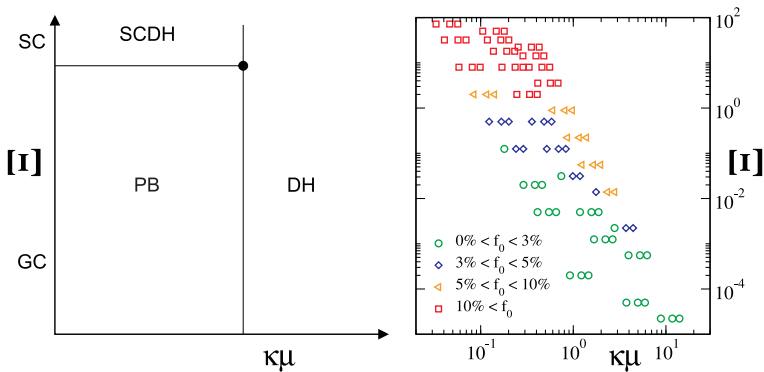


Figure 5.1: (a) The field-theoretical prediction by Punkkinen separates the parameter space in three regimes: Debye-Hückel, Poisson-Boltzmann, and a Strong-Coupling regime. (b) A comparison between Monte-Carlo and Poisson-Boltzmann data for monopoles in terms of the comparison parameter f_0 , showing for these methods the deviations in the distribution of charge in the ionic double layer.

Theoretical studies have been performed investigating the parameter regime in which PB theory gives trustworthy results regarding the effective interactions between homogeneously charged (colloidal) surfaces. Punkkinen *et al.* used a field-theoretic study [80] to show that the parameter space for point ions can effectively be divided into three regions using the parameters $\kappa\mu = 2/\gamma$ and $\Xi = (\gamma/2)\kappa\lambda_B$, with $\gamma = 4\pi\sigma\lambda_B/\kappa$ the nonlinearity parameter and σ the charge density in units of the elementary charge e . As is shown in Fig 5.1(a) they found (I) a region where Debye-Hückel theory holds, the screening is linear, (II) a region where the charge of the surfaces becomes higher, one has to solve the non-linear Poisson-Boltzmann equation to find the effective electrostatic interactions, and (III) a region in which the ion correlations close to the surface require Strong-Coupling (SC) theory [85, 96].

In this chapter we will explore the parameter space (I & II) for which PB theory is an accurate description for the charge profiles in the double layer around

charged Janus particles. To this extent Monte–Carlo (MC) simulations of the ion-density profiles around a single colloid are performed and these will be compared with results of a Poisson–Boltzmann approach. Unlike Punkkinen *et al.* we will use nonvanishing ionic radii in order to check whether the ion radius (which does influence neither $\kappa\mu$ nor Ξ) is important. As antisymmetric Janus particles do not have a net charge we cannot use the average charge density to calculate the parameters used by Punkkinen *et al.*, as one finds vanishing Ξ and infinite $\kappa\mu$ in this case. Therefore parameters are introduced that depend on the absolute amount of charge on the particles, instead of the net amount. The latter allows for the parameterisation of a charge distribution with a strong dipolar component. In order to compare the charge-density profiles between PB and MC we will expand both profiles using Legendre polynomials, allowing for an analysis of the monopole, dipole, quadrupole, and higher order modes.

The second part of this chapter will deal with calculating the effective interactions between Janus particles within the Debye–Hückel approximation. Because Janus particles lack spherical symmetry, DLVO theory cannot be applied in its well-known form. In the literature, models that have been applied instead include approximations in which the charged hemisphere as a finite number of point charges that interact with point charges on another particle via Yukawa potentials [97]. However, this generally results in an expensive calculation of the pair interaction of two colloids as a function of their orientations and separation, such that simplifications have to be applied for practical purposes such as MC simulations. Above that it is unknown how one should properly account for the hard cores of the colloidal particles within this point-charge model; scaling all charges with a factor $\exp(\kappa a)/(1 + \kappa a)$, similar to DLVO theory for monopoles, unfortunately will turn out not to be the proper way to go here. We will show that DLVO theory itself can be generalised to inhomogeneously charged particles. Especially the addition of a ‘Yukawa dipole’ to the properties of a colloid gives a reasonable approximation to the ion distributions around the Janus colloid, compared to full PB simulations. The expression for the dipole–dipole interaction that we will derive is therefore expected to give good results in describing interacting Janus particles.

5.2 Method

A single colloidal particle of radius a , placed in the center of a volume V , is considered. The distribution of charge on the surface of the particle is such to represent a Janus particle, namely two different charge densities on each hemisphere. In our calculations we will consider perfectly antisymmetric Janus particles; having a charge $Ze/2$ on the upper hemisphere and a charge $-Ze/2$ on the lower hemisphere. Unless stated differently, we will choose $Z = 100$ throughout the chapter. The number of monovalent ions $N \equiv N_+ + N_-$ in the system is fixed and the balance between positive and negative ions is chosen such that the net charge of the colloid

and the ions vanishes, which means in this case that $N_+ = N_-$. Throughout our derivations we will assume that the dielectric constants of the particle, ions, and medium are equal. This eliminates any boundary conditions from the electrostatic potential related to dielectric discontinuities and image charges [98–101].

5.2.1 Ewald Sums in the Canonical Ensemble

We consider a cubic simulation box of length $L = 50d$, where d is the ion diameter. The ribs of the box are aligned parallel to the axes of a standard Cartesian coordinate frame and we locate the origin of the system in the center of the box. Periodic boundary conditions are imposed. The particle's charge is distributed over the surface in $Z/2$ positive and $Z/2$ negative monovalent charge points at a distance $a - d/2$ from the center of the particle, spaced as equidistantly as possible. See the 100 point optimal-packing-coordinate file in Ref. [102] for the relevant distribution. The interaction potential between two ions at positions \mathbf{r}_i and \mathbf{r}_j is given by

$$\mathcal{V}(\mathbf{r}_i, \mathbf{r}_j) = \frac{q_i q_j e^2}{4\pi\epsilon} \frac{1}{|\mathbf{r}_i - \mathbf{r}_j|} + \begin{cases} \infty & : |\mathbf{r}_i - \mathbf{r}_j| \leq d \\ 0 & : |\mathbf{r}_i - \mathbf{r}_j| > d \end{cases}, \quad (5.1)$$

with ϵ the relative dielectric constant of the medium in which the ions are solvated, $q_i = \pm 1$ the sign of the i -th ion's charge. The interaction potential between a charge site of the particle, located at \mathbf{r}_i , and an ion located at \mathbf{r}_j is given by

$$\mathcal{V}(\mathbf{r}_i, \mathbf{r}_j) = \frac{q_i q_j e^2}{4\pi\epsilon} \frac{1}{|\mathbf{r}_i - \mathbf{r}_j|} + \begin{cases} \infty & : |\mathbf{r}_j| \leq a + d/2 \\ 0 & : |\mathbf{r}_j| > a + d/2 \end{cases}, \quad (5.2)$$

where $q_i = +1$ and $q_j = \pm 1$, depending on the charge of ion j . For the single central charge particle we have $i = 1$, $\mathbf{r}_i = \mathbf{0}$, and $q_i = +100$. To sample phase space a restricted primitive model Monte Carlo (MC) simulation is performed in the canonical (NVT) ensemble. Only single particle moves for the ions are considered. Periodicity and the long ranged nature of the interaction potentials, Eqs. (5.1) and (5.2), are taken into account by using Ewald Sums (ES) with conductive boundary conditions [103].

5.2.2 Poisson-Boltzmann Approach

The particle of radius a in a cubic box models a system with colloid/macroion volume fraction

$$\eta = \frac{4\pi}{3} \left(\frac{a}{L}\right)^3. \quad (5.3)$$

To study the PB theory equivalent of the above MC system we consider a spherical Wigner-Seitz cell model [18, 104–106] with radius

$$R = \sqrt[3]{\frac{3L^3}{4\pi}} = a\eta^{-1/3}, \quad (5.4)$$

to ensure that the volumes, and therefore the average densities of ions, in both methods are the same. We will apply PB theory to find the dimensionless electrostatic potential $\phi(\mathbf{r})$ and the associated ion densities $\rho_{\pm}(\mathbf{r})$ around the colloid. By using a spherical hard-core exclusion volume \mathcal{V}_{HC} with radius $a + d/2$ and a charge density $q(\mathbf{r})$ that will be defined below we find the PB equation

$$\nabla^2 \phi(\mathbf{r}) = 4\pi\lambda_{\text{B}}q(\mathbf{r}) + \begin{cases} 0 & \text{if } |\mathbf{r}| \leq a + d/2 \\ \kappa^2 \sinh(\phi) & \text{if } |\mathbf{r}| > a + d/2, \end{cases} \quad (5.5)$$

where $q(\mathbf{r})$ is the colloidal charge distribution and $\kappa^2 = 8\pi\lambda_{\text{B}}\rho_s$, with ρ_s the (yet unknown) bulk ion density. The cell boundary condition

$$\nabla \phi(\mathbf{r}) \cdot \hat{\mathbf{r}}|_{r=R} = 0 \quad (5.6)$$

ensures that the normal component of the electric field vanishes at the cell boundary. To be able to solve the Poisson-Boltzmann equation for the Janus particle, the charge density and the electrostatic potential of interest are expanded as

$$q(\mathbf{r}) = \sum_{\ell} \sigma_{\ell} \delta(r - a) P_{\ell}(x); \quad (5.7)$$

$$\phi(\mathbf{r}) = \sum_{\ell} \phi_{\ell}(r) P_{\ell}(x), \quad (5.8)$$

using $x = \mathbf{r} \cdot \hat{\mathbf{z}}$, with $\hat{\mathbf{z}}$ the orientation of the colloid and P_{ℓ} the Legendre polynomials. The nonlinear PB equation (2.29) can likewise be written mode-by-mode by expanding the sinh term around the monopole potential $\phi_0(z)$. Mode couplings are induced as the higher-order expansion coefficients contain products of Legendre polynomials $P_{\ell}P_{\ell'}$, which must be rewritten as a sum of other Legendre polynomials $P_{\ell''}$. Because of these mode couplings one needs to consider a significant number of multipoles even if for example only the dipole mode is of interest. As we derived in Section 2.7, such nonlinear behaviour becomes only important if the nonlinearity parameter γ is locally (much) larger than unity. An effective method to handle couplings in the sinh term will be discussed in Chapter 8. The expansion parameters σ_{ℓ} corresponding to the charge distribution of the Janus particle will be considered in Chapter 6. Since PB theory is a grand-canonical theory it requires to specify a bulk ion density ρ_s , this relates to the chemical potential of the ions. However, in the present case we are dealing with a canonical problem, the number of ions is fixed. Therefore, $\rho_{s,\text{PB}}$ must be determined from a fit procedure; by calculating

$$N_{\pm,\text{PB}} = 4\pi \int d\mathbf{r} \rho_{\pm,\text{PB}}(\mathbf{r}). \quad (5.9)$$

We determine ρ_s iteratively by demanding $N_{\pm,\text{PB}} = N_{\pm}$. All PB calculations were performed using a grid of size 2000 in the radial direction, and a Taylor expansion of the sinh term up to the 5th power using 6 multipole modes.

5.3 Results

All in all 99 systems are considered. Three particle radii are used, $a = 5d, 10d,$ and $15d$. For each a , three salt concentrations are studied, i.e., we choose $N_{\pm} = 175, 300,$ and 425 . For each a and N_{\pm} combination, we consider 11 Bjerrum lengths $\lambda_B/d = 0.01, 0.05, 0.1, 0.25, 0.5, 1.0, 2.0, 4.0, 6.0, 8.0,$ and 10.0 .

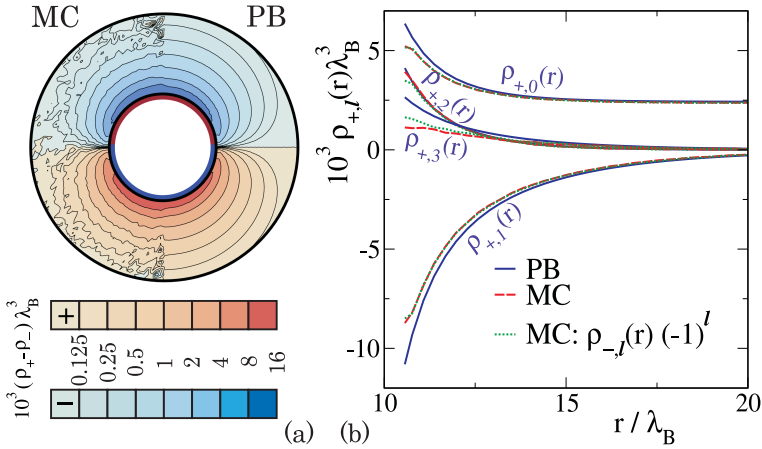


Figure 5.2: A comparison between MC and PB showing the ion densities around the Janus particle for $N_{\pm} = 300$, $\lambda_B = d$, and $a = 10\lambda_B$. In (a) a contour plot shows the net charge density $\rho_+(r) - \rho_-(r)$, on the left side the MC result and on the right the nonlinear PB solution. In (b) a mode expansion of the charge density $\rho_{\pm,\ell}(r)$ shows the same data. Note that the negative modes in (b) can in this case be mapped onto the positive modes by multiplication with $(-1)^\ell$.

Fig. 5.2 gives the results for a typical set of parameters that were tested for the antisymmetric Janus particle. In Fig. 5.2(a) the net ion density that is obtained from both MC and PB considerations are compared with each other. For this the azimuthal average of the MC ion densities is calculated. Fluctuations at the poles are therefore somewhat larger. We find good agreement between both methods, which also reflects in (b) which shows the first few components of the ion-density profiles $\rho_{\pm,\ell}(r)$. The local dimensionless charge density is $y = \pm 5.2$ in this case, which implies that mode couplings should occur. Indeed the monopole modes $\rho_{\pm 0}(r)$ can be observed to increase close to the colloidal surface although the charge net charge density had no monopole component. Also the nonvanishing quadrupole modes $\rho_{\pm 2}(r)$ are completely induced by couplings of other modes with each other. We observe that the same mode couplings also follow implicitly from MC simulations.

In order to quantify the difference in results between MC and PB, functions f_ℓ

can be defined which quantify the difference in the ℓ 'th mode of the ion distributions around the colloid. For a general Janus particle with Z_N unit charges on the upper hemisphere and Z_S unit charges on the lower hemisphere, we propose

$$f_\ell = \frac{4\pi}{|Z_N| + |Z_S|} \int dr r^2 |\rho_{\ell,MC}(r) - \rho_{\ell,PB}(r)|, \quad (5.10)$$

with the charge-density profiles $\rho_\ell(r) = \rho_{+, \ell}(r) - \rho_{-, \ell}(r)$. Eq. (5.10) vanishes if MC and PB charge profiles match, as required. Since the countercharge in the double layer should compensate for the net charge on a colloid, Eq. (5.10) has been normalised with the total amount of colloidal charge such that for a pure monopole (a homogeneously charged particle) $f_0 \rightarrow 2$ in case there is maximum disagreement between MC and PB on the distribution of countercharge, for example if the MC method would predict a total condensation of counter ions in a very small region close to the surface whilst PB theory would find the countercharge located in a diffuse layer of significant width. The extension to higher order f_ℓ , $\ell > 0$, is such that the range $(0 - 2)$ gives a good indication of the (weighed) integrated difference in the charge-density profiles due to the particular mode.

In order to test our method, we start by calculating MC and PB charge profiles for homogeneously charged particles with $Z = 100$, using the same range in λ_B/d and a as for the Janus particles. The results for f_0 are shown in Fig. 5.1(b). Good agreement is found at lower values of Ξ , whilst the value of $\kappa\mu$ is of minor importance as Debye-Hückel theory is just the low-charge limit of PB. By defining $\Xi = 10$ as the onset of strong coupling [80], one finds $f_0 \approx 10\%$ as the upper boundary for the PB regime.

Fig. 5.3 shows f_ℓ for $\ell = 0, 1, 2$, and 3 for the antisymmetric Janus particles of interest. We use modified parameters, defined by $y_\Sigma = 2/(\kappa\mu_\Sigma) \equiv (|Z_N| + |Z_S|)/(\kappa a^2)$ and $\Xi_\Sigma \equiv (y_\Sigma/2)\kappa\lambda_B$. Note that instead of the net charge of the particle these parameters rely on the sum of the absolute amount of charge on each hemispheres; for pure monopoles this will reduce to the conventional parameters y and Ξ . Although mode couplings do occur, the antisymmetry of the problem for the particles under consideration should cause the charge-density profiles ρ_ℓ to vanish for even ℓ . This can indeed be observed from the low values of f_ℓ for the monopole and quadrupole modes in Fig. 5.3. However some noise in the MC data at high Ξ_Σ for the quadrupole mode is present. As this is a minor contribution, noise is expected to be negligible as well for the odd modes plotted here. The dipole mode is the first order of interest for our comparison. We observe similar trends as was observed for the monopole. Observed is that if Ξ_Σ becomes (much) larger than unity, the agreement between MC and PB results weakens. This is likely caused by strong-coupling interactions which are not included within PB. However, a clear regime can be distinguished where PB gives accurate results regarding the charge profiles in the double layer. Approximately the same parameter regime holds for the octopole ($\ell = 8$) mode, and we also observed a similar regime of validity for $\ell = 5$ (not plotted). The modified

parameter Ξ_Σ can therefore be used as a parameter that can be meaningful to value the validity of PB for these antisymmetric Janus particles, with $\Xi_\Sigma \approx 1$ the upper bound. Its definition allows this parameter to be applied for different Janus particles that are not antisymmetric in charge but also have a monopole-charge component as well.

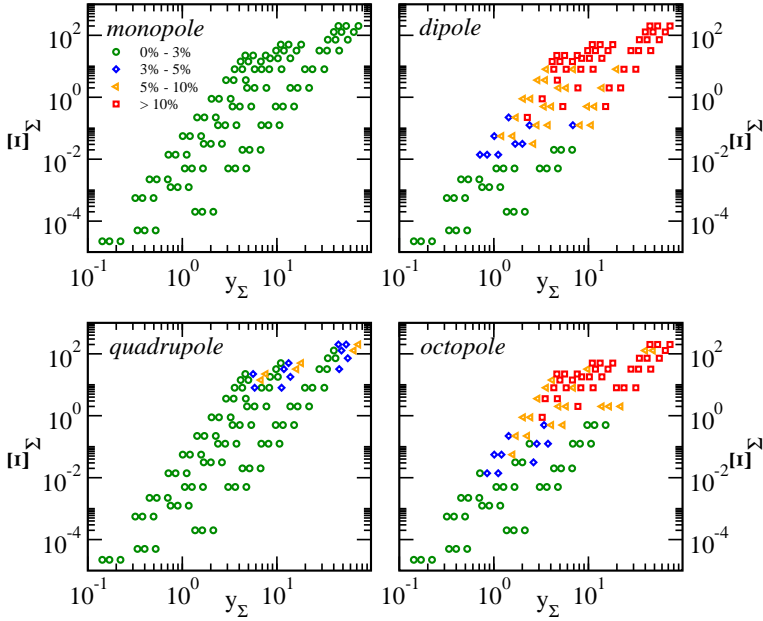


Figure 5.3: The deviations f_ℓ as defined in Eq.(5.10) in the double-layer charge profiles between MC and PB methods as a function of the dimensionless charge density, y_Σ which can be interpreted as the nonlinearity parameter, and the strong-coupling parameter Ξ_Σ . The subgraphs show the calculated difference parameter f_ℓ for $\ell = 0, 1, 2, 3$ corresponding to the monopole, dipole, quadrupole and octopole respectively.

5.4 DLVO theory for dipolar colloids

As we saw, the mode expansion up to $\ell = 6$ gives good agreement between MC and PB in a well-defined regime of parameters. For Janus particles in general the most dominant charge multipoles are the monopole and/or the dipole, but for the antisymmetric particles that we considered in this chapter the monopole vanishes. Fig. 5.2 shows the PB result regarding the charge densities for such a Janus particle, using a smaller charge ($Z = 10$) to make sure that the Debye-Hückel approximation holds. Note that the amount of ions added to the system, $N_\pm = 425$, corresponds to $\kappa a = 2.8$ and $y = 0.36$ here. The left side shows the solution up to $\ell = 6$, which

we showed to be sufficient for good correspondence with MC results, whereas the right side only shows the dipole mode. The differences are therefore due to the missing $\ell = 3$ and $\ell = 5$ terms. Note that the dipole approximation overestimates the electrostatic potential in the axial direction, whilst it underestimates the electrostatic potential in the perpendicular direction. However performance is reasonably good. Therefore, the dipole will probably capture most of the physics regarding the interacting Janus particles, certainly at larger distances. We will generalise the derivation of DLVO theory, as was performed in Chapter 2, to inhomogeneously charged particles. This will allow us to find explicit equations for the dipole-dipole interaction energy between Janus particles as a function of their orientation, in a similar form as what is known for dipoles without screening.

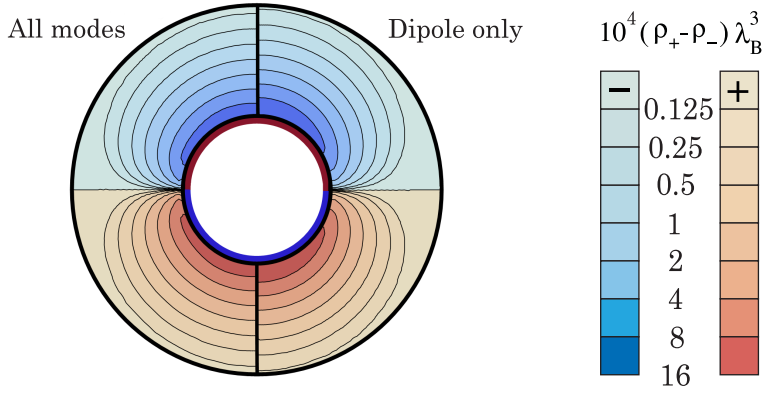


Figure 5.4: A contour plot of the net charge density $\rho_+(\mathbf{r}) - \rho_-(\mathbf{r})$ around an antisymmetric Janus particle for the parameters $Z = 10$, $N_{\pm} = 425$, $\lambda_B = d$, and $a = 10\lambda_B$, showing left the profile that follows from a mode expansion up to $\ell = 6$, whilst right only the dipole mode is plotted.

In Chapter 2 we applied the Debye-Hückel approximation to the effective electrostatic interaction energy of a charge configuration $q(\mathbf{r})$ without hard-core volumes. It was found that

$$\beta H[q] = \int d\mathbf{r} \sum_{\alpha=\pm} \rho_{\alpha}(\mathbf{r}) \left(\frac{\rho_{\alpha}(\mathbf{r})}{\rho_s} - 2 \right) + \frac{1}{2} \int d\mathbf{r} (\rho_+(\mathbf{r}) - \rho_-(\mathbf{r}) + q(\mathbf{r})) \phi(\mathbf{r}), \quad (5.11)$$

with ion densities $\rho_{\pm}(\mathbf{r})$ and $\phi(\mathbf{r})$ given by

$$\phi(\mathbf{r}) = \int d\mathbf{r}' \lambda_B \frac{\rho_+(\mathbf{r}') - \rho_-(\mathbf{r}') + q(\mathbf{r}')}{|\mathbf{r} - \mathbf{r}'|}. \quad (5.12)$$

Instead of point charges we will now consider a collection of charge distributions localised around points \mathbf{r}_{ci} . We define M volumes V_i around \mathbf{r}_{ci} , with $i \leq M$, and

suppose that the charge density $q(\mathbf{r})$ of Eq. (5.11) can be written as a sum of M individual, non-overlapping charge distributions $q_i(\mathbf{r})$,

$$q_i(\mathbf{r}) = \begin{cases} q(\mathbf{r}) & \text{if } \mathbf{r} \text{ is inside } V_i; \\ 0 & \text{otherwise,} \end{cases} \quad (5.13)$$

such that $q(\mathbf{r}) = \sum_{i=1}^M q_i(\mathbf{r})$. Note that we do not include hard-cores yet. Furtheron, $q_i(\mathbf{r})$ will be the effective charge density that is corrected for the ion-exclusion from the hard-core of colloid i with hard-core volume V_i . At this point the ion densities therefore follow from Eq. (5.11) as $\rho_{\pm}(\mathbf{r}) = \mp \sum_{i=1}^M \phi_i(\mathbf{r})$, with

$$\phi_i(\mathbf{r}) = \int_{V_i} d\mathbf{r}' q_i(\mathbf{r}') \frac{\exp(-\kappa|\mathbf{r}' - \mathbf{r}|)}{|\mathbf{r}' - \mathbf{r}|}. \quad (5.14)$$

By assuming that the charges within each V_i are at fixed distances from each other, Eq. (5.11) can be written, up to a self-energy constant, as

$$\beta H[q] = \sum_{i < j} \int_{V_i} d\mathbf{r} \int_{V_j} d\mathbf{r}' q_i(\mathbf{r}) q_j(\mathbf{r}') \frac{\exp(-\kappa|\mathbf{r}' - \mathbf{r}|)}{|\mathbf{r}' - \mathbf{r}|}. \quad (5.15)$$

The latter equation was derived within the Debye-Hückel approximation and therefore gives appropriate results only in case the dimensionless electrostatic potential $\phi(\mathbf{r})$ remains sufficiently small w.r.t. unity. We will use the result of Eq. (5.15) to obtain an analogous theory for charge distributions that do have associated hard-core volumes. This is done by 'freezing' the ions inside the volumes V_i and add their charges to the charge configuration $q(\mathbf{r})$, such that the Hamiltonian for hard-core particles with 'new' charge distributions $\tilde{q}_i(\mathbf{r})$ is found. The latter charge density will be defined below.

Starting with the obtained ion densities for the system without hard cores, we split the entire volume into V_{out} , consisting of all points \mathbf{r} outside the volumes V_i for all i , and the volume V_{in} of points that are inside one of these cells. Note that V_{in} is the complement of V_{out} . The ion densities are also split into $\rho_{\pm, \text{out}}(\mathbf{r})$ and $\rho_{\pm, \text{in}}(\mathbf{r})$ such that $\rho_{\pm, \text{out}}(\mathbf{r}) + \rho_{\pm, \text{in}}(\mathbf{r}) = \rho_{\pm}(\mathbf{r})$ and $\rho_{\pm, \text{out}}(\mathbf{r}) = 0$ for all \mathbf{r} inside V_{in} , and $\rho_{\pm, \text{in}}(\mathbf{r}) = 0$ for all \mathbf{r} inside V_{out} . Eq (5.11) may therefore be rewritten as

$$\begin{aligned} \beta H[q] &= \int_{V_{\text{out}}} d\mathbf{r} \sum_{\alpha=\pm} \rho_{\alpha, \text{out}}(\mathbf{r}) \left(\frac{\rho_{\alpha, \text{out}}(\mathbf{r})}{\rho_s} - 2 \right) + \int_{V_{\text{in}}} d\mathbf{r} \sum_{\alpha=\pm} \rho_{\alpha, \text{in}}(\mathbf{r}) \left(\frac{\rho_{\alpha, \text{in}}(\mathbf{r})}{\rho_s} - 2 \right) \\ &+ \frac{1}{2} \int d\mathbf{r} (\rho_{+, \text{out}}(\mathbf{r}) - \rho_{-, \text{out}}(\mathbf{r}) + \tilde{q}(\mathbf{r})) \phi(\mathbf{r}), \end{aligned} \quad (5.16)$$

with

$$\phi(\mathbf{r}) = \int d\mathbf{r}' \lambda_B \frac{\rho_{+, \text{out}}(\mathbf{r}') - \rho_{-, \text{out}}(\mathbf{r}') + \tilde{q}(\mathbf{r}')}{|\mathbf{r} - \mathbf{r}'|}, \quad (5.17)$$

and

$$\tilde{q}(\mathbf{r}) = q(\mathbf{r}) + \rho_{+,in}(\mathbf{r}) - \rho_{-,in}(\mathbf{r}) \quad (5.18)$$

$$= \sum_{i=1}^M \tilde{q}_i(\mathbf{r}), \quad (5.19)$$

with the 'new' colloidal charge distributions $\tilde{q}_i(\mathbf{r}) \equiv q_i(\mathbf{r}) + \rho_{+,in}(\mathbf{r}) - \rho_{-,in}(\mathbf{r})$ for \mathbf{r} inside V_i . Within the (DLVO-) approximation that the net ionic charge density $\rho_{+,in}(\mathbf{r}) - \rho_{-,in}(\mathbf{r})$ in volume V_i is only induced by the fixed charges $q_i(\mathbf{r})$ in that volume itself one finds for \mathbf{r} in V_i

$$\begin{aligned} \tilde{q}_i(\mathbf{r}) &\approx q_i(\mathbf{r}) - 2\rho_s \phi_i(\mathbf{r}) \\ &= q_i(\mathbf{r}) - 2\lambda_B \rho_s \int_{V_i} d\mathbf{r}' q_i(\mathbf{r}') \frac{\exp(-\kappa|\mathbf{r}' - \mathbf{r}|)}{|\mathbf{r}' - \mathbf{r}|}. \end{aligned} \quad (5.20)$$

The second term in Eq. (5.16) becomes a constant that may regarded as a self-energy term and therefore can be skipped to yield

$$\beta H[q] = \int_{V_{out}} d\mathbf{r} \sum_{\alpha=\pm} \rho_{\alpha}(\mathbf{r}) \left(\frac{\rho_{\alpha}(\mathbf{r})}{\rho_s} - 2 \right) + \frac{1}{2} \int d\mathbf{r} (\rho_+(\mathbf{r}) - \rho_-(\mathbf{r}) + \tilde{q}(\mathbf{r})) \phi(\mathbf{r}) \quad (5.21)$$

with the restriction that $\rho_{\pm}(\mathbf{r}) = 0$ if \mathbf{r} is inside V_{in} . In the latter equation the effective interaction Hamiltonian between hard-core particles with charge densities $\tilde{q}_i(\mathbf{r})$ can be recognised, which is also found after the Debye-Hückel approximation to the ion densities outside the hard-cores is applied to the effective Hamiltonian of interacting inhomogeneously charged hard-core colloids. As a result, the effective interaction energy for such a system can thus be obtained from Eq. (5.15). Note that for a given particle with hard-core volumes V_i and corresponding charge densities $\tilde{q}_i(\mathbf{r})$ it is therefore necessary to first solve $q_i(\mathbf{r})$ from Eq. (5.20), as these are required in Eq. (5.15). The latter procedure can be regarded as finding the charge densities that correct for the presence the hard cores.

Up to now the derivation includes the full interaction between inhomogeneously charged colloidal particles, within the DLVO approximation that we discussed earlier. In order to isolate specific multipole interactions between colloids, Eq. (5.15) is rewritten as

$$\beta H[q] = \sum_{i < j} \int_{V_i} d\mathbf{s}_i \int_{V_j} d\mathbf{s}_j q_i(\mathbf{r}_{ci} + \mathbf{s}_i) q_j(\mathbf{r}_{cj} + \mathbf{s}_j) \frac{\exp(-\kappa|\mathbf{R}_{ij} + \mathbf{s}_j - \mathbf{s}_i|)}{|\mathbf{R}_{ij} + \mathbf{s}_j - \mathbf{s}_i|}, \quad (5.22)$$

with $\mathbf{R}_{ij} = \mathbf{r}_{cj} - \mathbf{r}_{ci}$ the colloid-colloid distance and $\mathbf{s}_i = \mathbf{r} - \mathbf{r}_{ci}$ the coordinate relative to \mathbf{r}_{ci} . Both are shown in Fig. 5.5. The Yukawa interaction can then be expanded by using spherical harmonics around these centers [107], which are \mathbf{r}_{ci} and \mathbf{r}_{cj} . For

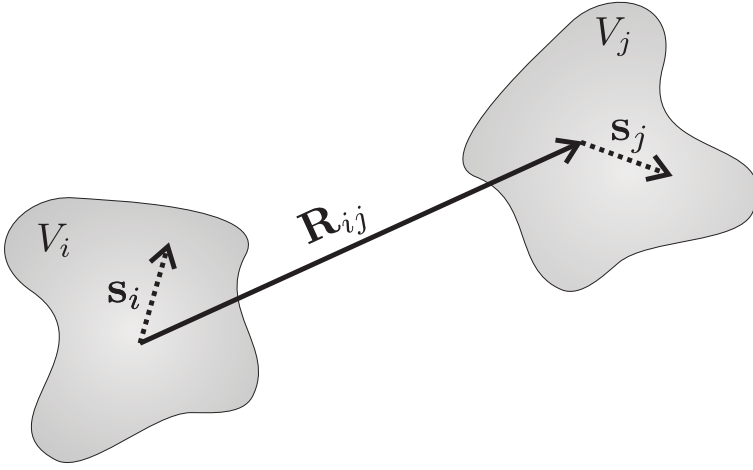


Figure 5.5: A sketch of two interaction charge distributions q_i and q_j separated by a distance R_{ij} , and the vectors \mathbf{s}_i and \mathbf{s}_j that have their origins at \mathbf{r}_{ci} and \mathbf{r}_{cj} respectively.

this we must assume that the distance from any point in V_i to its center \mathbf{r}_{ci} is less than the distance to any other center \mathbf{r}_{cj} . This however automatically holds for equisized spherical volumes if one chooses the centers \mathbf{r}_{ci} exactly in the middle of the spheres. For now, the monopole and dipole terms are of main interest. Eq. (5.22) can be expanded up to a monopole-monopole, monopole-dipole and dipole-dipole interaction term as

$$H[q] = \sum_{i < j} \mathcal{V}_{ij}^{\text{MM}}(R_{ij}) + \mathcal{V}_{ij}^{\text{MD}}(\mathbf{R}_{ij}) + \mathcal{V}_{ij}^{\text{DD}}(\mathbf{R}_{ij}), \quad (5.23)$$

respectively. It can be calculated that the interaction terms are given by

$$\beta \mathcal{V}_{ij}^{\text{MM}}(R_{ij}) = \lambda_B \frac{\exp(-\kappa R_{ij})}{R_{ij}} Z_i^Y Z_j^Y; \quad (5.24)$$

$$\beta \mathcal{V}_{ij}^{\text{MD}}(\mathbf{R}_{ij}) = \lambda_B \frac{\exp(-\kappa R_{ij})}{R_{ij}^2} \left((\mathbf{p}_i^Y \cdot \hat{\mathbf{R}}_{ij}) Z_j^Y - (\mathbf{p}_j^Y \cdot \hat{\mathbf{R}}_{ij}) Z_i^Y \right); \quad (5.25)$$

$$\begin{aligned} \beta \mathcal{V}_{ij}^{\text{DD}}(\mathbf{R}_{ij}) &= \lambda_B \frac{\exp(-\kappa R_{ij})}{R_{ij}^3} \left((1 + \kappa R_{ij}) (\mathbf{p}_i^Y \cdot \mathbf{p}_j^Y) \right. \\ &\quad \left. - (3 + 3\kappa R_{ij} + (\kappa R_{ij})^2) (\mathbf{p}_i^Y \cdot \hat{\mathbf{R}}_{ij}) (\mathbf{p}_j^Y \cdot \hat{\mathbf{R}}_{ij}) \right), \end{aligned} \quad (5.26)$$

in which the ‘Yukawa monopole’ and ‘Yukawa dipole’ are defined by

$$Z_i^Y = \int_{V_i} d\mathbf{s}_i q_i(\mathbf{r}_{ci} + \mathbf{s}_i) \frac{\sinh \kappa s_i}{\kappa s_i}; \quad (5.27)$$

$$\mathbf{p}_i^Y = 3 \int_{V_i} d\mathbf{s}_i q_i(\mathbf{r}_{ci} + \mathbf{s}_i) \mathbf{s}_i \left(\frac{\cosh \kappa s_i - \frac{1}{\kappa s_i} \sinh \kappa s_i}{(\kappa s_i)^2} \right). \quad (5.28)$$

Note that Eqs. (5.27) and (5.28) reduce to the well-known expressions for Coulomb monopole and dipole in the limit $\kappa a \downarrow 0$ [10]. Also the interactions terms (5.24)–(5.26) give the well-known result for pure Coulombic systems in this limit. The electrostatic potential around charge distribution i can be expanded as

$$\phi_i(\mathbf{r}_{ci} + \mathbf{s}_i) = Z_i^Y \lambda_B \frac{\exp(-\kappa s_i)}{s_i} + (\mathbf{p}_i^Y \cdot \hat{\mathbf{s}}_i) \lambda_B \frac{\exp(-\kappa s_i)}{s_i^2} (1 + \kappa s_i) + \mathcal{O}(\ell \geq 2) \quad (5.29)$$

in which quadrupole and higher order multipoles are not included. As an example we show that the interaction between particles with a homogeneous charge distribution is in agreement with DLVO theory. By considering a spherical colloid with a hard core radius a and a charge Z at its surface and choosing $\mathbf{r}_{ci} = 0$ for convenience, the charge distribution is given by $\tilde{q} = Z/(4\pi a^2) \delta(s_i - a)$. It can be shown that

$$q_i(\mathbf{s}_i) \begin{cases} \frac{Z}{4\pi a^2} \delta(s_i - a) + \frac{Z \lambda_B 2 \rho_s}{a(1 + \kappa a)} & \text{if } s_i \leq a, \\ 0 & \text{if } s_i > a. \end{cases} \quad (5.30)$$

solves Eq. (5.20). Note that the ‘added’ charge density inside the colloids has the same sign of charge as that on the surface. From Eq. (5.27) one obtains $Z_i^Y = Z \exp(\kappa a)/(1 + \kappa a)$ and this gives the DLVO result as Eq. (5.24) shows.

The Yukawa monopole and the Yukawa dipole can also be extracted from the solution for the electrostatic potential outside the particle, using Eq. (5.29), *without* knowing the local distribution of charges q_i explicitly. As will be shown in Chapter 6, the electrostatic potential outside inhomogeneously charged particles can be expanded as $\Phi(s_i, x_i) = \sum_{\ell=0}^{\infty} \Phi_{\ell}(s_i) P_{\ell}(x_i)$, in which $x = \hat{\mathbf{s}}_i \cdot \hat{\mathbf{n}}_i$, and $P_{\ell}(x_i)$ the ℓ 'th Legendre polynomials. Now $\ell = 0$ and $\ell = 1$ correspond to the monopole and the dipole contribution to the electrostatic potential respectively. The multipole mode functions scale as $\Phi_{\ell}(s_i) \sim s_i^{\ell}$ for $r < a$ and $\Phi_{\ell}(s_i) \sim k_i(\kappa s_i)$ for $r > a$, with k_i the i 'th modified spherical Bessel function. This will be concerned in more detail in Chapter 6 itself. By applying boundary condition (6.4) a solution to the electrostatic potential in terms of a multipole expansion is obtained. The latter solution may be compared to Eq. (5.29) to yield

$$Z_i^Y = 4\pi a^2 \sigma_0 \frac{\exp(\kappa a)}{1 + \kappa a}; \quad (5.31)$$

$$\mathbf{p}_i^Y = \hat{\mathbf{n}}_i 4\pi a^3 \sigma_1 \frac{\exp(\kappa a)}{3 + 3\kappa a + (\kappa a)^2}, \quad (5.32)$$

which holds in general for spherical particles with orientation \hat{n}_i . In the case of Janus particles with charge densities $\sigma_N e$ and $\sigma_S e$ on the upper and lower hemisphere respectively, one finds $\sigma_0 = \frac{1}{2}(\sigma_N + \sigma_S)$ and $\sigma_1 = \frac{3}{4}(\sigma_N - \sigma_S)$.

Throughout this chapter we assumed that the dielectric constant of the particles matched the dielectric constant of the solvent. The derivation we performed in order to obtain the interactions turns out to become very complicated in case of a mismatch in dielectric constant. However, Eq. (5.32) can easily be extended to particles that have a dielectric mismatch with the solvent by including a dielectric jump in the BC of Eq. (6.4), such that the Yukawa multipoles for these particles can be obtained as well. As expected, we find that the Yukawa monopole is unaffected by the value of the dielectric constant inside the particle, whilst the Yukawa dipole changes. Eq. (5.32) becomes

$$\mathbf{p}_i^Y = \hat{n}_i 4\pi a^3 \sigma_1 \frac{\exp(\kappa a)}{(2 + \epsilon_c/\epsilon)(1 + \kappa a) + (\kappa a)^2}, \quad (5.33)$$

with ϵ_c/ϵ the ratio of the relative dielectric constant inside and outside the particles. Note that the dipole becomes very small if the interior of the colloid is very polar (e.g. water), such that monopole–dipole and dipole–dipole interactions will probably be negligible. However, if the dielectric constant of the colloid is comparable or smaller than the dielectric constant of the solvent a significant dipolar interaction may arise.

5.5 Discussion

Poisson–Boltzmann theory can be applied in a well-defined parameter regime to calculate the ion-density profiles around charged Janus particles. Using a new-defined agreement parameter f_ℓ , correspondence between PB-calculations and Monte-Carlo simulations of the ion-density profiles is found in approximately the same parameter regime for the leading multipole modes as was found by Punkkinen *et al.* [80] for homogeneously charged walls. We find no indication that the regime of validity changes for the higher-order modes of the ionic charge profiles. Because of the inhomogeneous distribution of charge on the Janus particles the pair interactions do not only depend on distance but also on the orientation of the particles. DLVO theory for inhomogeneously charged particles, which describes the interactions between particles in the form of a multipole expansion, can therefore be of significant usefulness. By correcting the colloidal charge distribution for ion exclusion from the hard cores we find explicit equations that describe the interactions between general inhomogeneously charged particles within the DLVO approximation. A multipole expansions of the Yukawa potential then allows us to find explicit equations for the monopole–monopole, monopole–dipole, and dipole–dipole interactions. We did not include higher-order modes in this study, but this would be possible as well. Associated to the latter interactions are the Yukawa monopole and Yukawa dipole, and the expressions for these reduce to the expressions for the Coulomb monopole

and dipole in the ion-free Coulomb limit, $\kappa a \rightarrow 0$. The Yukawa monopole of an inhomogeneously charged particle is calculated from the bare charge corrected with a factor $\exp(\kappa a)/(1 + \kappa a)$, as known from DLVO theory, but the higher-multipole modes scale differently. We derived explicit expressions for the Yukawa monopole and dipole for Janus particles in general. We found that multipole interaction can especially be important for particles that have a relatively low dielectric constant.

Future work could for example consider finding the parameter range in which (low density) plastic crystals of Janus particles are to be expected. It could also focus on Janus particles that are only charged on the upper hemisphere (the $g = 1$ particles of the next chapter); by shifting the origin of the multipole expansion one could for example make the Yukawa dipoles vanish for the latter particle species. Therefore the interactions of these half-charged particles will probably be described accurately by shifted monopole-monopole interactions on top of unshifted hard-core interactions. The next chapter will consider charge renormalisation of Janus particles. We will obtain renormalised values for the charge-density multipoles σ_ℓ which can be used to correct for the Debye-Hückel approximation in case the charge on the particles is high.

Acknowledgement We thank Joost de Graaf and Marjolein Dijkstra for all the Monte Carlo simulations that were performed to support this chapter, and for sharing their thoughts on this matter.

Chapter 6

Charge renormalisation of Janus particles

Nonlinear ionic screening theory for *heterogeneously* charged spheres is developed in terms of a mode-decomposition of the surface charge. A far-field analysis of the resulting electrostatic potential leads to a natural generalisation of charge renormalisation from purely monopolar to dipolar, quadrupolar, etc., including ‘mode-couplings’. Our novel scheme is generally applicable to large classes of surface heterogeneities, and is explicitly applied here to Janus spheres with differently charged upper and lower hemispheres, revealing strong renormalisation effects for all multipoles.

6.1 Introduction

The past few years have seen an explosion of newly synthesised colloidal (nano-)particles that are *not* spherically symmetric, either by shape (e.g. dumbbells, snowmen, cubes) or by surface pattern (patches, stripes) [108]. A broken rotational symmetry also occurs when particles are adsorbed to air-water or oil-water interfaces [109], as in for example, colloidal monolayers [110, 111], Pickering emulsions [112], or bijels [113, 114]. Moreover, recent atomic force microscopy studies have shown that even supposedly homogeneous colloidal surfaces can actually be heterogeneous on length scales as large as 100 nm [115], while atomic corrugations and facets render any nm-sized particle strictly heterogeneous. An important consequence of surface heterogeneity is anisotropy of the mutual effective forces, which directly affects the self-assembly process of the (nano)colloids into large-scale structures, for instance into ill-understood linear chains [111, 115–117].

A fundamental problem is thus to establish relationships between shape and surface heterogeneity on the one hand and effective interactions and large-scale self-assembly structures on the other [108]. Apart from specific forces (e.g., hydrophobic, van der Waals) the effective interactions between dispersed particles often involve a strong generic electrostatic component, which is well-described, for homogeneously charged objects, by linear-screening theory *provided* renormalised charges instead

of bare charges are used [15, 18–21]. Renormalisation of heterogeneously distributed surface charge is an open problem, for which we develop a systematic theory in this chapter. We go beyond recent linear screening treatments [118–123] and formulate a new and efficient framework for computing *nonlinear* ionic screening effects of heterogeneously charged spheres dispersed in a 1:1 electrolyte. Our theory generalises Alexander’s notion of ion-condensation induced charge-renormalisation [15, 18–21] to include not only the monopole but also the dipole, quadrupole, etc., as well as their nonlinear couplings. These multipole modes can be important if one wishes to calculate the electrostatic force between particles, which was already shown for clay platelets [124]. Our scheme is versatile and can be applied to essentially any type of charge heterogeneity. We focus on applications to Janus spheres composed of two differently charged hemispheres [125, 126].

We consider an index-matched suspension of N colloidal spheres of radius a in a bulk solvent of dielectric constant ϵ and volume V at temperature T . The solvent also contains point-like monovalent cations (charge $+e$) and anions (charge $-e$) at fugacity ρ_s . Here e is the elementary charge. A relatively simple treatment of this many-body problem is the cell model [15, 18–21], in which a single colloid is considered in the center of a spherical cell of radius R and volume $(4\pi/3)R^3 \equiv V/N$. We denote the surface charge density of this central colloidal particle by $e\sigma(\theta, \varphi)$, where θ and φ are the standard polar and azimuthal angle, respectively, with respect to a laboratory frame. Within a mean-field approximation, the concentration profiles of the cations and anions can be written as Boltzmann distributions $\rho_{\pm}(\mathbf{r}) = \rho_s \exp[\mp\Phi(\mathbf{r})]$, where $k_B T\Phi(\mathbf{r})/e$ is the electrostatic potential at $\mathbf{r} = (r, \theta, \varphi)$, with k_B the Boltzmann constant and $r = |\mathbf{r}|$. Note that $\Phi(\mathbf{r}) = 0$ in the salt reservoir, and that $\rho_{\pm}(\mathbf{r}) = 0$ for $r < a$ due to hard-core exclusion. The potential must satisfy the Poisson equation $\nabla^2\Phi(\mathbf{r}) = -4\pi\lambda_B(\rho_+(\mathbf{r}) - \rho_-(\mathbf{r}))$, where we defined the Bjerrum length $\lambda_B = e^2/\epsilon k_B T$. Combining the Poisson and Boltzmann equations gives

$$\Phi''(\mathbf{r}) + \frac{2\Phi'(\mathbf{r})}{r} - \frac{\mathcal{L}^2\Phi(\mathbf{r})}{r^2} = \begin{cases} 0 & r < a; \\ \kappa^2 \sinh\Phi(\mathbf{r}) & r > a, \end{cases} \quad (6.1)$$

where a prime denotes a radial derivative, $\mathcal{L}^2 = -[(\sin\theta)^{-1}\partial_\theta\sin\theta\partial_\theta + (\sin\theta)^{-2}\partial_\varphi^2]$ the *angular momentum operator*, and $\kappa^{-1} = (8\pi\lambda_B\rho_s)^{-1/2}$ the screening length. On the colloidal surface, $r = a$, Gauss’ law imposes the boundary condition (BC)

$$\lim_{r \downarrow a} \Phi'(r, \theta, \varphi) = \lim_{r \uparrow a} \Phi'(r, \theta, \varphi) - 4\pi\lambda_B\sigma(\theta, \varphi). \quad (6.2)$$

Electro-neutrality of the cell imposes $\int d\varphi d\theta \sin\theta \Phi'(R, \theta, \varphi) = 0$ at $r = R$, which is a sufficiently stringent BC to close the system of equations in the spherically symmetric case. Now, however, an additional BC is to be specified for the angular dependence at $r = R$, depending on the environment of the cell. For now, we assume an environment that is characterised by ‘isotropic’ boundary conditions,

$$\partial_\theta\Phi(R, \theta, \varphi) = \partial_\varphi\Phi(R, \theta, \varphi) = 0. \quad (6.3)$$

We will discuss this choice, and its consequences, in section 6.4.

6.2 Theory

For a given $\sigma(\theta, \varphi)$ one can solve Eq. (6.1) with BC's for $\Phi(\mathbf{r})$, for example, numerically on a discrete (r, θ, φ) grid. The approach we take, however, avoids a cumbersome 3-dimensional grid in favor of a systematic expansion of the angular dependence in spherical harmonics. For notational convenience and illustration purposes we restrict attention here to φ -independent cases where the expansion involves only Legendre polynomials $P_\ell(x)$ with $x = \cos \theta$.

The first step in this analysis is the decomposition of the colloidal surface charge into surface multipoles $\sigma_\ell = \frac{2\ell+1}{2} \int_{-1}^1 dx \sigma(x) P_\ell(x)$, such that $\sigma(x) = \sum_{\ell=0}^{\infty} \sigma_\ell P_\ell(x)$. Similarly we decompose $\Phi(r, x) = \sum_{\ell=0}^{\infty} \Phi_\ell(r) P_\ell(x)$. With $\Phi_\ell(r) = (r/a)^\ell \Phi_\ell(a)$ the regular solution to (6.1) for $r \in [0, a]$, the BC's for $r \in \{a, R\}$,

$$\Phi'_\ell(a) = \frac{\ell}{a} \Phi_\ell(a) - 4\pi\lambda_B \sigma_\ell \quad (\ell \geq 0); \quad (6.4)$$

$$\Phi'_0(R) = 0 \text{ and } \Phi_\ell(R) = 0 \quad (\ell \geq 1), \quad (6.5)$$

conveniently decouple for the different ℓ 's. By contrast, the nonlinear sinh term in (6.1) induces 'mode-coupling' between *all* Legendre components $\Phi_\ell(r)$ – not to be confused with mode-couplings in dynamical slowing down. This coupling is obviously unpractical for a numerical treatment.

The second step of our analysis resolves this mode-coupling problem by 'ordering' the modes systematically. We introduce a dimensionless 'switching' parameter A , and consider the auxiliary distribution $\sigma^{(A)}(x) = \sum_{\ell=0}^{\infty} A^\ell \sigma_\ell P_\ell(x)$, such that $A = 0$ describes a homogeneous distribution and $A = 1$ the heterogeneous one of interest. We also define the corresponding auxiliary potential $\Phi^{(A)}(r, x) = \sum_{n=0}^L A^n \phi_n(r, x)$, where L sets the order of the truncation and where the expansion coefficients can themselves be expanded as $\phi_n(r, x) = \sum_{\ell=0}^n f_{n\ell}(r) P_\ell(x)$. The functions $f_{n\ell}(r)$ are independent of A and will be calculated numerically below for the cases of interest $n \geq \ell$ (which is assumed implicitly from now on). Since the problem is invariant under the simultaneous transformation $A \rightarrow -A$ and $x \rightarrow -x$ one checks that $f_{n\ell}(r) = 0$ for $n + \ell$ odd, that is, we only consider ℓ and n both even or both odd.

Replacing $\sigma(x)$ by $\sigma^{(A)}(x)$ and $\Phi(r, x)$ by $\Phi^{(A)}(r, x)$, inserting the corresponding expansions into the BC's, and equating all orders of A yields at $r \downarrow a$ and $r = R$

$$f'_{n\ell}(a) = \frac{\ell}{a} f_{n\ell}(a) - 4\pi\lambda_B \sigma_\ell \delta_{n\ell}; \quad (6.6)$$

$$f'_{n\ell}(R) = 0 \quad (\ell = 0) \text{ and } f_{n\ell}(R) = 0 \quad (\ell \geq 1), \quad (6.7)$$

where $\delta_{n\ell}$ is the Kronecker-delta. When the same replacement and expansion procedure is applied to the PB equation (6.1), one finds upon expanding the argument of the sinh term with respect to A a hierarchy of second-order differential equations for $f_{n\ell}(r)$, with a structure that allows for an order-by-order sequential solution. For $n = \ell = 0$ we obtain for $r \in [a, R]$ the spherically symmetric nonlinear PB equation

in the cell, $f''_{00}(r) + \frac{2f'_{00}(r)}{r} = \kappa^2 \sinh f_{00}(r)$, which we solve explicitly with the BC's given in (6.6) and (6.7) on a radial grid. We thus consider $f_{00}(r)$ as a known function from now on. For $n \geq 1$ we obtain

$$f''_{n\ell}(r) + \frac{2f'_{n\ell}(r)}{r} - \left(\frac{\ell(\ell+1)}{r^2} + \kappa^2 \cosh f_{00}(r) \right) f_{n\ell}(r) = \kappa^2 S_{n\ell}(r), \quad (6.8)$$

where $S_{n\ell}(r)$ acts as a source term of the form

$$\begin{aligned} S_{11} &= 0; \\ S_{20} &= \frac{1}{6} f_{11}^2 \sinh f_{00}; \\ S_{22} &= 2S_{20}; \\ S_{31} &= f_{11}(f_{20} + \frac{2}{5} f_{22}) \sinh f_{00} + \frac{1}{10} f_{11}^3 \cosh f_{00}; \\ S_{33} &= \frac{3}{5} f_{11} f_{22} \sinh f_{00} + \frac{1}{15} f_{11}^3 \cosh f_{00}, \end{aligned}$$

and explicit expressions for higher-order terms can be generated straightforwardly. The key observation is that $S_{n\ell}$ *only* depends on $f_{n'\ell'}$'s with $n' < n$, that is, a hierarchy of terms follows spontaneously. Thus Eq. (6.8) with the BC's (6.6) and (6.7) can be solved for $n = \ell = 1$, which in turn determines $S_{20}(r)$ and $S_{22}(r)$ such that $f_{20}(r)$ and $f_{22}(r)$ can be solved, etc. The nonlinear mode-coupling, represented explicitly by $\cosh f_{00}(r)$ and $S_{n\ell}(r)$, renders the linear equation Eq. (6.8) highly nontrivial, yet numerical solution on a radial grid $r \in [a, R]$ is straightforward. With $f_{n\ell}(r)$ determined for $L \geq n \geq \ell \geq 0$ for some cut-off L , we can set $A = 1$ to explicitly construct the potential of interest $\Phi(r, x) = \sum_{\ell=0}^L \Phi_{\ell}(r) P_{\ell}(x)$ with $\Phi_{\ell}(r) = \sum_{n=\ell}^L f_{n\ell}(r)$.

6.3 Results

The theory developed so far is directly applicable to any uniaxial charge distribution, while generalisations to azimuthal dependencies and nonspherical shapes are feasible. In this chapter we illustrate our scheme for the prototype heterogeneous charge distribution of Janus spheres characterised by surface charge-densities σ_N and σ_S on the northern ($x > 0$) and southern ($x < 0$) hemisphere, respectively [97, 125, 126]. The non-vanishing modes are thus $\sigma_0 = (\sigma_N + \sigma_S)/2$, and

$$\sigma_{\ell} = g \sigma_0 (-1)^{\frac{\ell-1}{2}} \frac{(1+2\ell)\ell!!}{(\ell^2 + \ell)(\ell-1)!!} \quad \text{for } \ell \text{ odd.} \quad (6.9)$$

Here we defined the dimensionless heterogeneity parameter

$$g = \frac{\sigma_N - \sigma_S}{\sigma_N + \sigma_S}, \quad (6.10)$$

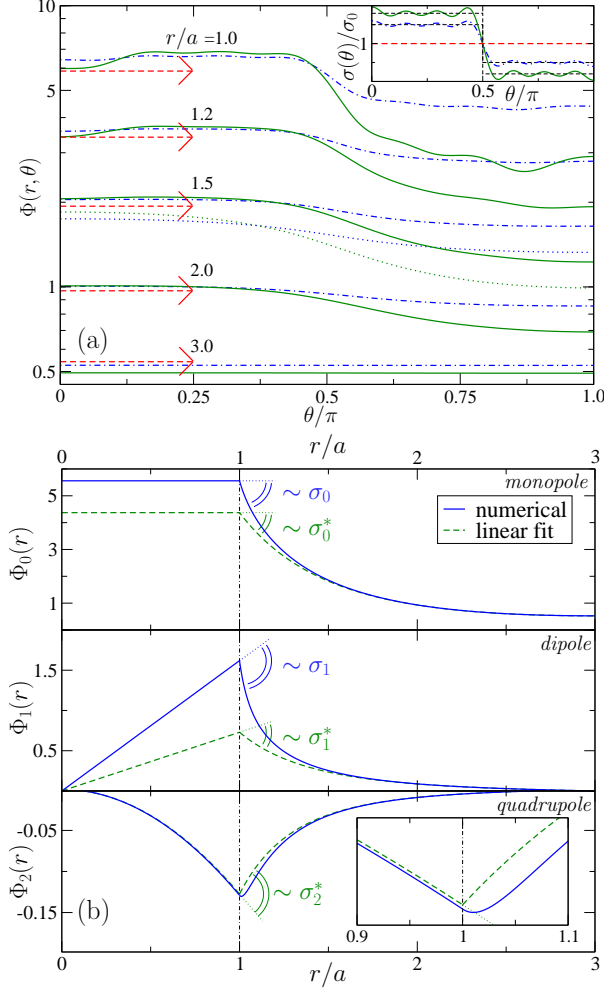


Figure 6.1: (a) Angular dependence of the potential (at several distances r) and the surface charge (inset) of a Janus sphere of radius a , for $\kappa a = 1$, $Z_0 \lambda_B / a = 22.5$, $R/a = 3$, and $L = 13$, for charge heterogeneities (see text) $g = 0$ (arrows), $g = 0.5$ (dot-dashed), and $g = 0.8$ (solid curves). The dotted curves for $r/a = 1.5$ and $g \in \{0.5, 0.8\}$ stem from a Yukawa-segment model (see text). (b) Radial dependence of the monopole ($\ell = 0$), dipole ($\ell = 1$), and quadrupole ($\ell = 2$) potentials $\Phi_\ell(r)$ (solid lines), and their far-field linear-screening approximations (dashed curves), for the parameters of (a) and $g = 0.5$. The angles defined at $r = a$ relate to the bare and renormalised modes of the surface charge (see text).

which together with the total charge $Z_0 = 4\pi a^2 \sigma_0$ fully characterises the distribution. Note that the equation in the original article [213] was unfortunately incorrectly

stated. Below we set $\kappa a = 1$, $R/a = 3$, and $L = 13$ throughout unless stated otherwise, and we identify $Z_0 \lambda_B/a$ as the only other relevant dimensionless combination. For $Z_0 \lambda_B/a = 22.5$ and $g \in \{0, 0.5, 0.8\}$ Fig. 6.1(a) shows the θ -dependence of σ (inset) and Φ for several r , revealing isotropy (as expected) for a homogeneous surface charge ($g = 0$, arrows) and strong anisotropy for the heterogeneous cases $g = 0.5$ ($\sigma_N = 3\sigma_S$, dot-dashed) and $g = 0.8$ ($\sigma_N = 9\sigma_S$, solid lines); the (small) oscillations with θ at $r = a$ are numerical artefacts due to the truncation at $L = 13$. The θ -dependence of the potential weakens, as expected, for increasing distances r . Fig. 6.1(b) shows $\Phi_\ell(r)$ for $\ell = 0, 1, 2$ and $g = 0.5$. Interestingly, the modes with $\ell = 1, 2$ have a non-vanishing electric field in the interior of the particle. The overall magnitude and spatial variation of Φ in Fig. 6.1 show the need for nonlinear screening theory. Nevertheless, in analogy to the spherically symmetric case [15, 18–21] one can describe the far-field potential ($r \simeq R$) and hence the colloidal interactions in terms of *linear* screening theory (dashed curves in Fig. 6.1(b)) with a renormalised surface charge distribution $\sigma^*(x) \equiv \sum_\ell \sigma_\ell^* P_\ell(x)$ that we will calculate below.

In the far-field $r \simeq R$ we treat the deviation of $\Phi(r, x)$ from its angular average $\Phi_0(R) \equiv \chi_0$ at $r = R$ as a small expansion parameter, such that (6.1) for $r > a$ can be linearised as $\nabla^2 \Phi(r, x) \simeq \bar{\kappa}^2 [\tanh \chi_0 + (\Phi(r, x) - \chi_0)]$ with $\bar{\kappa}^2 = \kappa^2 \cosh \chi_0$. The uniaxial solutions to this linear PB (LPB) equation read $\Phi(r, x) \simeq \chi_0 - \tanh \chi_0 + \sum_{\ell=0}^{\infty} [a_\ell i_\ell(\bar{\kappa}r) + b_\ell k_\ell(\bar{\kappa}r)] P_\ell(x)$ where i_ℓ and k_ℓ are modified spherical Bessel functions. The coefficients a_ℓ and b_ℓ are integration constants that we fix by matching the LPB-solution at $r = R$, for each ℓ , to $\Phi_\ell(R) \equiv \chi_\ell$ and $\Phi'_\ell(R) \equiv \chi'_\ell$ of the *nonlinear* problem. This leads for every ℓ to the linear two by two problem

$$\begin{aligned} \chi_\ell &= (\chi_0 - \tanh \chi_0) \delta_{\ell 0} + a_\ell i_\ell(\bar{\kappa}R) + b_\ell k_\ell(\bar{\kappa}R); \\ \chi'_\ell &= \bar{\kappa} \left(a_\ell i'_\ell(\bar{\kappa}R) + b_\ell k'_\ell(\bar{\kappa}R) \right), \end{aligned} \quad (6.11)$$

which results in explicit expressions for a_ℓ and b_ℓ given by

$$a_\ell = \frac{v_\ell \left(k_{\ell+1}(\bar{\kappa}R) - \frac{\ell}{\bar{\kappa}R} k_\ell(\bar{\kappa}R) \right) + \chi'_\ell k_\ell(\bar{\kappa}R)}{i_\ell(\bar{\kappa}R) k_{\ell+1}(\bar{\kappa}R) + i_{\ell+1}(\bar{\kappa}R) k_\ell(\bar{\kappa}R)}, \quad (6.12)$$

$$b_\ell = \frac{v_\ell \left(i_{\ell+1}(\bar{\kappa}R) + \frac{\ell}{\bar{\kappa}R} i_\ell(\bar{\kappa}R) \right) - \chi'_\ell i_\ell(\bar{\kappa}R)}{i_\ell(\bar{\kappa}R) k_{\ell+1}(\bar{\kappa}R) + i_{\ell+1}(\bar{\kappa}R) k_\ell(\bar{\kappa}R)}, \quad (6.13)$$

where $v_\ell = \chi_\ell - (\chi_0 - \tanh \chi_0) \delta_{\ell 0}$. The dashed curves in Fig. 6.1(b) are the result of such a far-field fit. With a_ℓ and b_ℓ explicitly known, one can extrapolate the LPB solution to $r = a$ to yield, with Eq. (6.4) and standard Bessel function relations, the renormalised multipoles

$$\sigma_\ell^* = -\frac{\bar{\kappa}}{4\pi\lambda_B} \left(a_\ell i_{\ell+1}(\bar{\kappa}a) - b_\ell k_{\ell+1}(\bar{\kappa}a) \right). \quad (6.14)$$

This expression is the multipole generalisation of the well-known charge renormalisation [15, 18–21].

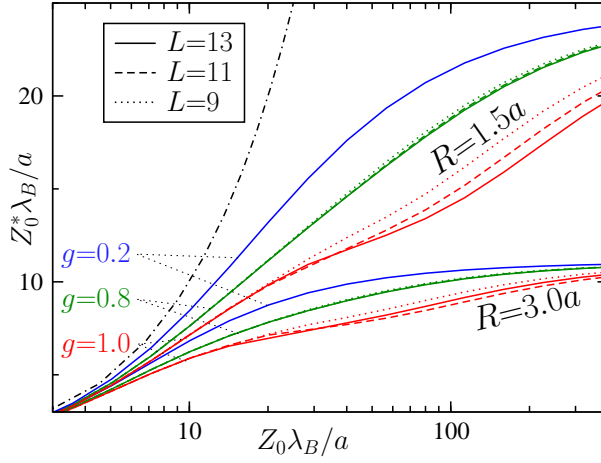


Figure 6.2: Renormalised (scaled) monopole Z_0^* for several g, L (see text) of a Janus sphere as a function of the total charge $Z_0\lambda_B/a$. The graph includes data for cell radii $R/a = 1.5$ and $R/a = 3.0$. The dot-dashed curve denotes $Z_0^* = Z_0$.

A first illustration of multipole renormalisation is shown by the angles in Fig. 6.1(b), which represent slope discontinuities at $r = a$ which are proportional to σ_ℓ (non-linear theory) and σ_ℓ^* (far-field fit). For $\ell = 0, 1$ we see $\sigma_\ell^* < \sigma_\ell$, which means that the effective charge and dipole are renormalised downward. Interestingly, however, for $\ell = 2$ the inset in the lowest panel reveals upward renormalisation since $\sigma_2^* \neq 0$ while $\sigma_2 = 0$, that is, the Janus particle has a mode-coupling induced far-field quadrupole signature. Multipole renormalisation is quantified further in figures 2–4, where (scaled) renormalised multipoles $Z_\ell^* = 4\pi a^2 \sigma_\ell^*$ are shown for the monopole $\ell = 0$ in Fig. 6.2, the dipole $\ell = 1$ in Fig. 6.3 (scaled with g), and the higher-order multipoles $\ell = 1, \dots, 6$ in Fig. 6.4. All multipoles are shown as a function of $Z_0\lambda_B/a$. Furthermore, in Figs. 6.2 and 6.3 we chose several truncation levels L and heterogeneities g , and also picked two cell radii R . The dot-dashed curves denote the linear limit $Z_\ell^* = Z_\ell$. Figs. 6.2 and 6.3 show that all curves for $L = 13$ superimpose on those of $L = 9, 11$ for all Z_0 and $g \lesssim 0.8$, indicative of excellent convergence in this parameter regime; for $g = 1$ the convergence deteriorates for $Z_0\lambda_B/a \gtrsim 15$. The R dependence in Figs. 6.2 and 6.3 shows the strongest renormalisation in the largest cell, not unlike the homogeneous-charge case [15, 18–21]. Interestingly, in the non-linear regime $Z_0\lambda_B/a \gtrsim 10$ Fig. 6.2 shows a mode-coupling induced *reduction* of Z_0^* by 10's of percents when g increases from 0 to 1. In other words, in contrast to the more usual ‘linear’ electrostatics we now have a far-field monopole potential that is not only determined by the net charge but in fact *also* by its heterogeneity. This is a key finding, relevant for understanding patchy-particle interactions. The mode coupling has an even stronger effect on renormalisation of Z_1^* , for which Fig. 6.3(a)

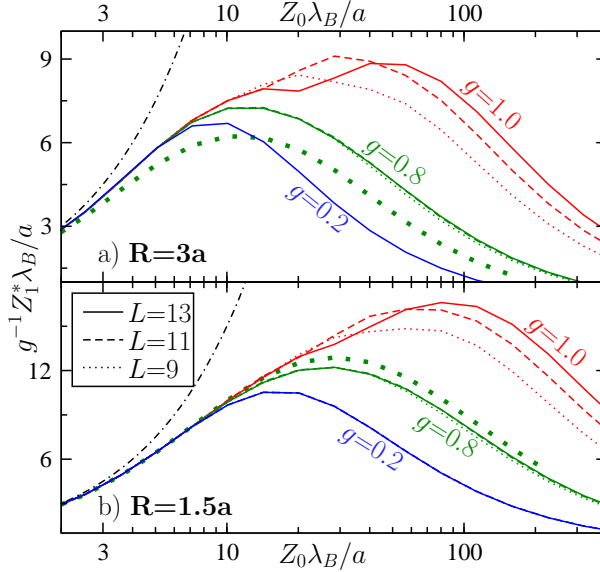


Figure 6.3: Renormalised (scaled) dipole Z_1^* for several g, L (see text) of a Janus sphere as a function of the total charge $Z_0 \lambda_B / a$. The upper and the lower graph represent cell sizes $R/a = 3.0$ and $R/a = 1.5$ respectively. The thick dotted lines denote the (scaled) difference of the renormalised northern and southern charge presumed distributed homogeneously (see text) for $g = 0.8$. The dot-dashed curves in both graphs denote $Z_1^* = Z_1$.

and (b) show a pronounced maximum in between the low- Z_0 linear screening regime and the high- Z_0 regime in which Z_1^* becomes even *vanishingly small* for all g 's considered. Fig. 6.4 shows, for $g = 0.4$, that in fact *all* Z_ℓ^* with $\ell \neq 0$ vanish in the limit of large Z_0 , while they all show an intermediate regime with finite values even for $\ell = 2, 4, 6$ for which $\sigma_\ell = 0$. The underlying physics for non-oppositely charged hemispheres with $\sigma_N > \sigma_S > 0$ (that is, with $0 < g < 1$) is that both σ_N and σ_S renormalise, if both are high enough, to the *same* saturated value, giving rise to a pure far-field monopole without multipoles.

The idea might emerge that both hemispheres renormalise their charge independent of each other, that is, some of the results could suggest that the renormalised charge density on the colloidal surface is a function which depends only locally on the bare charge density. If that were the case, it would suffice to calculate the renormalised surface charge-density for σ_N and σ_S , as if both were the charge density of a monopole. The cell radius is to be kept unchanged. The thick dotted lines in Fig. 6.3(a) and (b) denote the resulting dipole for $g = 0.8$, which is calculated with the obtained (renormalised) σ_N^* and σ_S^* by $\frac{3}{4}(\sigma_N^* - \sigma_S^*)$. The correspondence with the solid line is at best reasonable but not perfect. Also the effective monopole is

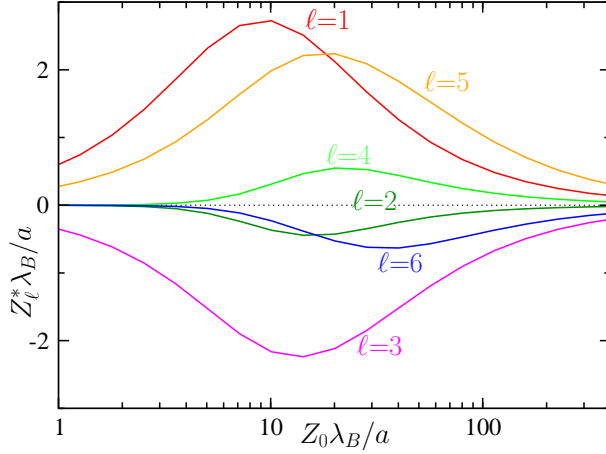


Figure 6.4: Renormalised (scaled) multipoles Z_l^* of a Janus sphere as a function of the total charge $Z_0\lambda_B/a$. The parameters here are $g = 0.4$ and $L = 13$.

not accurately predicted. This can be seen from Fig. 6.5, where we investigate the cell-size dependence of the effective monopole for $g = 0.4, 0.8$ and for $\kappa a = 1, 3$. We included data from the full theory (depicted by symbols) and the predicted values by $2\pi a^2(\sigma_N^* + \sigma_S^*)$ as a solid line. One can see that the monopole charge is underestimated for a wide range of cell radii, especially for larger cells. Nevertheless, there is qualitative agreement on the increase of the renormalised charge with higher values for κa . The difference with the full theory is expected to be the largest for very heterogeneously charged particles. Indeed, we see the largest discrepancy in Fig. 6.5(a) and (b) for $g = 0.8$, with deviations up to 20–25% between the results of the present theory for σ_0^* and those of the simple approximation $(\sigma_N^* + \sigma_S^*)/2$ discussed above. Apparently, the interactions between the hemispheres do play a role, which in fact can also be concluded from the induced even multipoles in Fig. 6.4. Further research might give more insight into the characteristics of these interactions.

6.4 Discussion

The newly emerging general picture is that nonlinear ionic screening of heterogeneously distributed surface charges strongly affects the far-field symmetry of the potential, and hence also the symmetry of the effective interactions and the self-assembling structures. The systematics of the present screening theory could be a firm basis to further study these intricate features of heterogeneously charged particles. The category of particles which are described by $g > 1$, carrying positive and negative charges on the two hemispheres, are particularly interesting. Because

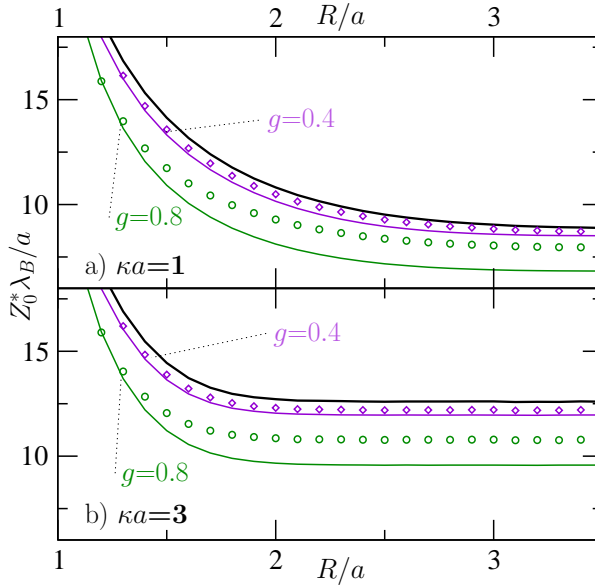


Figure 6.5: Renormalised monopole charge Z_0^* for several g of a Janus sphere as a function of the cell size R , both for $Z_0 \lambda_B / a = 22.5$, in (a) for $\kappa a = 1$ and in (b) for $\kappa a = 3$. The thick solid line corresponds to a pure bare monopole, yielding $g = 0$. The diamonds ($g = 0.4$) and circles ($g = 0.8$) show the data from the full theory, using $L = 13$. The thinner solid lines denote the average of the renormalised northern and southern charge presumed distributed homogeneously (see text) for $g = 0.4$ and $g = 0.8$.

the present method is not very efficient at high values of g , we have developed an alternative method to treat these mainly dipolar particles within a mode expansion as well. This method is similar to the method applied in Chapter 8 to calculate the electrostatic field in the vicinity of a patched plate.

It is tempting to model Janus spheres by a Yukawa-segment model [97] in which every surface element dS contributes $\sigma^*(x) \lambda_B s^{-1} \exp(-\kappa s) dS$ to the (dimensionless) potential at a distance s . Here the renormalised charge densities on both hemispheres is obtained from the renormalised monopole and dipole charge density via

$$\sigma^*(x) = \begin{cases} \sigma_0^* + \frac{2}{3} \sigma_1^* & x < 0; \\ \sigma_0^* - \frac{2}{3} \sigma_1^* & x \geq 0. \end{cases} \quad (6.15)$$

The dotted curves in Fig. 6.1(a) show that agreement with our full calculations is reasonable though not quantitative; the Yukawa model ignores the ionic hard-core exclusion in the interior of the particle. Therefore, effectively it describes the (dimensionless) potential of a charge configuration in which oppositely charged ions

were able to approach the heterogeneously charged surface from two sides, such that this potential is more suppressed compared to the full theory.

As a point of discussion, we return to the choice of the boundary conditions on the cell's surface (6.3), which we called 'isotropic' BC's. This denomination follows from the fact that, considering two randomly oriented neighboring cells, the cell-surface potentials of two cells should match on the spot where they touch, giving rise to a constant cell-surface potential. Nevertheless the choice of BC's is not unique. We can also supply the system with 'nematic' boundary conditions, corresponding to the situation that all cells are perfectly aligned such that cells only touch on opposite spots. On these spots the electrostatic potential should match, and we can also demand continuity of the electric field. The BC's then become

$$\begin{aligned}\Phi(R, \theta, \varphi) &= \Phi(R, \pi - \theta, \pi + \varphi), \\ \Phi'(R, \theta, \varphi) &= -\Phi'(R, \pi - \theta, \pi + \varphi).\end{aligned}\tag{6.16}$$

In fact one can even interpolate between 'isotropic' and 'nematic' BC's by introducing an orientation distribution function [127]. In this chapter, we assume a system in which the cell boundary is best described by isotropic BC's, given by (6.3). However, for the parameters used in this chapter, it turns out that this particular choice for the BC's did not noticeably affect the values of the renormalised charges. We do not see a significant change by turning to nematic BC's (6.16). This insensitivity to the choice of BC's is due to the fact that the nonlinear behaviour is an effect which takes place close to the colloidal surface, where these BC's have the least influence on the electrostatic potential. Furthermore, the only multipoles which are directly affected by the particular choice of BC's are the nonzero ($\ell > 0$) even multipoles, which are small for Janus particles. We therefore think that the obtained values for the renormalised multipoles can be applied in a model to describe the behaviour of a many-body system within linear theory, no matter what the orientations of the surrounding particles are. Since the monopole and multipole potentials decay for large r equally fast as $\exp(-\bar{\kappa}r)/r$ [128], where $\bar{\kappa}^{-1}$ is the decay length, the renormalised multipole charges are expected to contribute in dense as well as dilute systems.

In summary, we have developed a systematic framework for nonlinear ionic screening of heterogeneously charged spheres. The scheme allows for an explicit far-field analysis that generalises charge renormalisation from the well-studied homogeneous case (pure monopole) [15, 18–21] to the heterogeneous case (dipoles, quadrupoles, etc. and their nonlinear couplings). Application to charged Janus spheres shows (i) a 40% reduction of the effective monopole for $g = 1$ (charged and uncharged hemisphere) compared to $g = 0$ (homogeneously charged sphere), (ii) a mode-coupling induced far-field effective quadrupole component without an actual surface quadrupole, (iii) a pure far-field monopole with vanishing higher-order multipoles in the saturated high-charge limit, and (iv) no quantitative agreement with a simple Yukawa-segment model based on renormalised multipoles. Our study opens

the way to systematic microscopic calculations of effective electrostatic interactions between Janus (and other patchy) particles. In addition, our analyses also reveal non-vanishing electric fields *inside* heterogeneously charged particles, which could couple to interior dipoles and affect (anisotropic) mutual Van der Waals forces. Given that the presently introduced expansion technique can be generalised to other geometries (for example, patterned planar surfaces or ellipsoidal patchy particles), our technique and findings are directly relevant for gaining microscopic understanding of effective interactions and ultimately phase behaviour of a large class of dispersions of patchy or patterned nanoparticles, colloidal particles, or proteins [108].

Acknowledgement We thank Elma Carvajal Gallardo, Stephan Zheng, Eelco Eggen and Marjolein Dijkstra for useful discussions and a pleasant collaboration on this work.

Chapter 7

Phase diagrams of spheres with a constant zeta-potential

Abstract

We study suspensions of colloidal spheres with a constant zeta-potential within Poisson-Boltzmann theory, quantifying the discharging of the spheres with increasing colloid density and decreasing salt concentration. We use the calculated renormalised charge of the colloids to determine their pairwise effective screened-Coulomb repulsions. Bulk phase diagrams in the colloid concentration-salt concentration representation follow, for various zeta-potentials, by a mapping onto published fits of phase boundaries of point-Yukawa systems. Although the resulting phase diagrams do feature face-centered cubic (fcc) and body-centered cubic (bcc) phases, they are dominated by the (re-entrant) fluid phase due to the colloidal discharging with increasing colloid concentration and decreasing salt concentration.

7.1 Introduction

Charged colloidal particles suspended in a liquid electrolyte are interesting soft-matter systems that have generated fundamental as well as industrial attention for decades [129]. Understanding the stability and phase behaviour of these systems as a function of colloid concentration and ionic strength is an important theme in many of these studies. A key role is played by the electrostatic repulsions between the colloidal spheres, which are not only capable of stabilising suspensions against irreversible aggregation due to attractive Van der Waals forces [9], but are also the driving force for crystallisation [130], provided the surface charge on the colloids is sufficiently large and the range of the repulsions sufficiently long [9, 129, 130]. The classic theory that describes the electrostatic repulsions between charged colloidal particles in suspension goes back to the 1940's, when Derjaguin, Landau, Verwey, and Overbeek (DLVO) found, within linear screening theory, that suspended spheres repel each other by screened-coulomb (Yukawa) interactions [16, 17]. The strength of these repulsions increases with the square of the colloidal charge, and they

decay exponentially with particle-particle separation on the length scale of the Debye screening length of the solvent [131]. This pairwise Yukawa form is a cornerstone of colloid science, and can explain a large number of observations [9, 129, 130]. For instance, the experimentally observed crystallisation of charged colloidal spheres into body-centered cubic (bcc) and face-centered cubic (fcc) phases upon increasing the colloidal packing fraction at low and high salt concentrations [132–135], respectively, is in fair agreement with simulations of Yukawa systems [136–139]. Interestingly, in these simulation studies, as well as in many other studies [18, 21, 140, 141], the charge of the colloids is assumed to be independent of the colloid density and the salt concentration.

The constant-charge assumption was argued to break down, however, in some recent studies where the electrostatic repulsions were argued to be reduced with increasing colloid concentration. Biesheuvel [142], for instance, argues that experimental equilibrium sedimentation-diffusion profiles of charged silica spheres in ethanol at extremely low salt concentrations [143] are better fitted by a charge-regulation model than by a constant-charge model [144]. More recent evidence for a concentration-dependent colloidal charge stems from re-entrant melting and re-entrant freezing observations of PMMA spheres in a solvent mixture of *cis*-decaline and cyclohexyl bromide, i.e. the phase sequence upon increasing the colloid concentration is fluid-crystal-fluid-crystal [145]. In addition, direct force measurements between a single pair of colloidal PMMA spheres in hexadecane, a pair that is part of a triplet, and a pair that is part of a multiplet have very recently revealed a significant reduction of the force with increasing number of neighbouring particles [146]. Interestingly, in the three experiments of Refs.[143, 145, 146] the solvent is a nonpolar medium.

In fact, the experimental findings of Ref. [146] could well be interpreted and explained in terms of constant-potential boundary conditions on the colloidal surfaces, rather than the more usual constant-charge assumption. The present chapter addresses the consequence of constant-potential boundary conditions for the packing fraction-salt concentration phase diagram of Yukawa systems by calculating the colloidal charge and the effective screening length for various zeta-potentials as a function of salt- and colloid concentration. Perhaps surprisingly, such a study has not yet been performed. In the case of high zeta-potential this requires nonlinear screening theory, and hence the renormalised rather than the bare colloidal charge determines the effective screened-Coulomb repulsions between the colloids [14, 18, 21, 133, 147–151]. For this reason we use the renormalised charge throughout. We also compare our constant-potential calculations with those of an explicit charge-regulation model [152–157], and conclude that their results are qualitatively similar, and even quantitatively if they are considered as a function of the effective screening length.

7.2 Model and theory

We consider N colloidal spheres of radius a in a solvent of volume V , temperature T , dielectric constant ϵ and Bjerrum length $\lambda_B = e^2/\epsilon k_B T$. Here e is the elementary charge and k_B the Boltzmann constant. The colloidal density is denoted by $n = N/V$ and the packing fraction by $\eta = (4\pi/3)na^3$. The suspension is presumed to be in osmotic contact with a 1:1 electrolyte of Debye length κ^{-1} and total salt concentration $2\rho_s$. We are interested in suspensions of charged colloids of which the surface (zeta) potential ψ_0 rather than the charge Ze is fixed. We will show that this constant-potential condition mimics charge-regulation on the colloidal surfaces fairly accurately. The first goal of this chapter is to calculate Z as a function of η for fixed dimensionless combinations κa , a/λ_B , and $\phi_0 \equiv e\psi_0/k_B T$. This result will then be used to quantify the effective Yukawa interactions between pairs of colloids, and hence the phase boundaries between fluid, face-centered cubic (fcc) and body-centered cubic (bcc) crystalline phases.

In the actual suspension of constant-potential colloidal spheres, the charge distribution of each of the N colloids will be distributed heterogeneously over its surface due to the proximity of other colloids in some directions. This leads to a tremendously complex many-body problem that we simplify here by *assuming* a spherically symmetric environment for each colloid, which is nevertheless expected to describe the average electrostatic properties realistically. Below we will calculate the electrostatic potential $\psi(r)$ at a radial distance r from a charged colloidal sphere at a given zeta-potential ψ_0 , i.e. at a given value $\psi(a) = \psi_0$. The colloidal charge Ze then follows from Gauss' law

$$\psi'(a) = -\frac{Ze}{\epsilon a^2}, \quad (7.1)$$

where a prime denotes a radial derivative.

We first consider a single colloid in the center of a Wigner-Seitz cell of radius R , such that the cell volume equals the volume per particle, $(4\pi/3)R^3 = V/N$, which implies $R = a\eta^{-1/3}$. The radial coordinate of the cell is called r . We write the ionic density profiles for $r \in (a, R)$ as Boltzmann distributions $\rho_{\pm}(r) = \rho_s \exp(\mp\phi(r))$, with $\phi(r) = e\psi(r)/k_B T$ the dimensionless electrostatic potential. Together with the Poisson equation $\nabla^2\phi = -4\pi\lambda_B(\rho_+(r) - \rho_-(r))$, this gives rise to the radially symmetric PB-equation and boundary conditions (BC's)

$$\phi''(r) + \frac{2}{r}\phi'(r) = \kappa^2 \sinh \phi(r), \quad a < r < R; \quad (7.2)$$

$$\phi(a) = \phi_0; \quad (7.3)$$

$$\phi'(R) = 0, \quad (7.4)$$

where a prime denotes a derivative with respect to r . Note that BC (7.4) implies charge neutrality of the cell. Once the solution $\phi(r)$ is found for given η , κa , and ϕ_0 , e.g. numerically on a radial grid, the colloidal charge Z follows from Eq. (7.1),

which we rewrite in dimensionless form as

$$\frac{Z\lambda_B}{a} = -a\phi'(a). \quad (7.5)$$

From the numerical solutions that we will present below it turns out that Z decreases monotonically from a finite asymptotic low- η (large- R) value Z_0 to essentially 0 at $\eta \simeq 1$ (or $R \simeq a$).

Within linear-screening theory at low packing fraction, where $\sinh \phi \simeq \phi$, the potential distribution can be solved for analytically, yielding $\phi(r) = \phi_0 a \exp[-\kappa(r-a)]/r$, such that the colloidal charge takes the asymptotic low- η and low- ϕ_0 value

$$\frac{Z_0\lambda_B}{a} = (1 + \kappa a)\phi_0. \quad (7.6)$$

In the appendix we show that the discharging effect with increasing η , as found from the nonlinear screening theory discussed above, can also be approximated within linear screening theory, yielding

$$Z(\eta, \kappa a) = \frac{Z_0}{1 + \eta/\eta^*}, \quad \eta^* = \frac{(\kappa a)^2}{3(1 + \kappa a)}, \quad (7.7)$$

where η^* is a crossover packing fraction at which the colloidal charge has decayed to half its dilute-limit value Z_0 given in Eq. (7.6). For typical numbers of experimental interest, e.g. $a/\lambda_B = 100$ and $\kappa a = 0.25$, we then find $Z_0 = 125\phi_0$ and $\eta^* = 0.017$. With $\phi_0 \simeq 1-2$, which corresponds to a surface potential of 25-50mV, we should expect a few hundred charges in the dilute limit and a significant charge reduction for $\eta \gtrsim 10^{-2}$.

The constant-potential boundary condition that we employ here is supposed to mimic charge-regulation on the colloidal surface through an association-dissociation equilibrium of chargeable groups on the surface. Here we consider, as a typical example, the reaction $SA \rightleftharpoons S^+ + A^-$, where a neutral surface group SA dissociates into a positively charged surface group S^+ and a released anion A^- . The chemistry of such a reaction can be characterised by a reaction constant K such that $[S^+][A^-]/[SA] = K$, where the square brackets indicate concentrations in the vicinity of the surface where the reaction takes place. If we now realise that $Z \propto [S^+]$, we find for the usual case where $[S^+] \ll [SA]$ that $Z \propto 1/[A^-]$. For the case that the released anion is of the same species as the anion in the reservoir, such that $[A^-] = \rho_s \exp[\phi(a)]$, we thus have

$$Z = z \exp(-\phi(a)), \quad (7.8)$$

where the prefactor z , which is a measure for the surface chargeability (see in Chapter 8, where $z = Y\kappa a^2/\lambda_B$), accounts for the chemistry, the surface-site areal density, and the total area of the surface between the colloidal particle and the electrolyte solution, as considered in Chapter 8. Note that Eq. (7.8) relates the (yet

unknown) colloidal charge Z to the (yet unknown) zeta-potential $\phi(a)$, for a given z . A closed set of equations for charge-regulated colloids is obtained by combining the PB equation (7.2) with BC (7.4) at the boundary of a Wigner-Seitz cell of radius R , with BC (7.3) replaced by

$$a\phi'(a) = -\frac{\lambda_B Z}{a} \exp(-\phi(a)), \quad (7.9)$$

for some given chargeability z . The resulting solution $\phi(r)$ gives the zeta-potential $\phi(a)$ as well as the colloidal charge Z using Eq. (7.8). When comparing the constant-potential model with the ionic association-dissociation model, we will tune the chargeability z such that the low- η results for Z coincide for both models.

It is well known that nonlinear screening effects, in particular counterion condensation in the vicinity of a highly charged colloidal surface, reduce the effective colloidal charge that dictates the screened-Coulomb interactions between the colloids [14, 18, 21, 147, 148, 158]. The so-called renormalised colloidal charge, Z^* [159], can be calculated from the electrostatic potential $\phi(r)$ as obtained from the nonlinear PB equation by matching the numerically obtained solution at the edge of the cell to the analytically known solution of a suitably linearised problem. By extrapolating the solution of the linearised problem to the colloidal surface at $r = a$, one obtains the effective charge by evaluating the derivative at $r = a$ using Eq. (7.5). Following Trizac *et al.* [15], the renormalised charge Z^* can be written as

$$\frac{Z^* \lambda_B}{a} = -\frac{\tanh \phi_D}{\bar{\kappa} a} \left((\bar{\kappa}^2 a R - 1) \sinh[\bar{\kappa}(R - a)] + \bar{\kappa}(R - a) \cosh[\bar{\kappa}(R - a)] \right), \quad (7.10)$$

where the ‘Donnan’ potential is defined as $\phi_D \equiv \phi(R)$, i.e. the numerically found potential at the boundary of the cell, and where the effective inverse screening length is

$$\bar{\kappa} = \kappa \sqrt{\cosh \phi_D}. \quad (7.11)$$

Note that Z^* and $\bar{\kappa}$ can be calculated for the constant-potential as well as the association-dissociation model in a Wigner-Seitz cell.

7.3 Effective charge and screening length

For both the constant surface potential (CSP) and the association-dissociation (AD) model discussed above we calculated the bare colloidal charge Z , the effective (renormalised) charge Z^* , and the effective inverse screening length $\bar{\kappa}$ in the geometry of Wigner-Seitz cells. In Fig. 7.1 we show $Z\lambda_B/a$ (full curves) and $Z^*\lambda_B/a$ (dashed curves) as a function of packing fraction η , for two screening constants for both the CSP model (thick curves) and the AD model (thin curves), in (a) for fixed zeta-potential $\phi_0 = 1$ and in (b) for $\phi_0 = 5$. In all cases the chargeability parameter

z of the AD model is chosen such as to agree with the CSP model in the low-density limit $\eta \rightarrow 0$. The semi-quantitative agreement between the thick and the thin curves for equal κa is indicative of the reasonable description of charge-regulation by constant-potential BC's, certainly at low η . At higher η the charges predicted by the AD model exceed those of the CSP model somewhat, which should not come as a surprise since the former interpolates between the constant-charge and the constant-potential model. The close agreement between Z and Z^* for all κa at $\phi_0 = 1$ in Fig. 7.1(a) is also to be expected, since $\phi_0 = 1$ is not far into the nonlinear regime. By contrast, deep in the nonlinear regime of $\phi_0 = 5$, as shown in Fig. 7.1(b), there is a significant charge renormalisation effect such that $Z^* < Z$ by a factor of about 1.2 and 1.5 for $\kappa a = 0.1$ and $\kappa a = 0.5$, respectively. The merging of the thin and the thick curves at high- η in Fig. 7.1(b) is due to the reduction of the charge into the linear-screening regime such that $Z = Z^*$. The increase of Z^* with κ , as observed in both Fig. 7.1(a) and (b), is in line with well-known charge-renormalisation results [14, 15, 18, 21, 147, 148], and with Eq. 7.6.

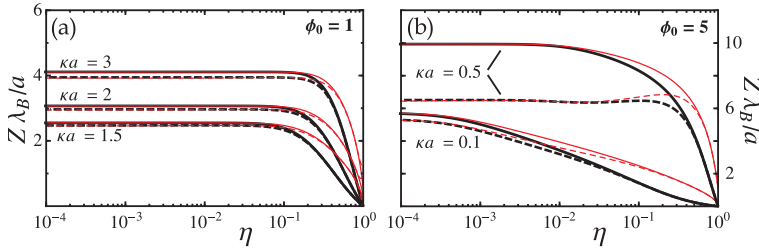


Figure 7.1: The bare colloidal charge Z (continuous thick curves) and the renormalised charge Z^* (dashed thick curves), both in units of a/λ_B (see text), as a function of the colloidal packing fraction η for several screening parameters κa , for constant surface potentials (a) $\phi_0 = 1$ and (b) $\phi_0 = 5$. The thin curves denote Z and Z^* as obtained from the association-dissociation model, with the chargeability z chosen such that the surface potential in the dilute limit $\eta \rightarrow 0$ equals ϕ_0 .

In Fig. 7.2(a) and (b) we plot, for the same zeta-potentials as in Fig. 7.1(a) and (b), the effective screening parameter $\bar{\kappa}$ as a function of η for several reservoir screening constants κ . At low enough η , where $\kappa R \gg 1$, the two screening constants are indistinguishable from each other in all cases. The reason is that the cell is then large enough for the potential to decay to essentially zero at $r = R$, such that the asymptotic decay of $\phi(r)$ is governed completely by the screening constant κ of the background (reservoir) salt concentration. At larger η , and hence smaller cells, $\phi(R)$ is no longer vanishingly small and the ion concentrations $\rho_{\pm}(R)$ at $r = R$ deviate considerably from the ionic reservoir concentration ρ_s . This larger ionic concentration at the cell boundary, which represents an enhanced ion concentration in between the colloidal particles in the true many-body system, leads to a larger effective screening constant $\bar{\kappa}$ with increasing η at a fixed κ , as is shown in Fig. 7.2(a) and (b). Given that larger charges are obtained in the AD model than in the CSP

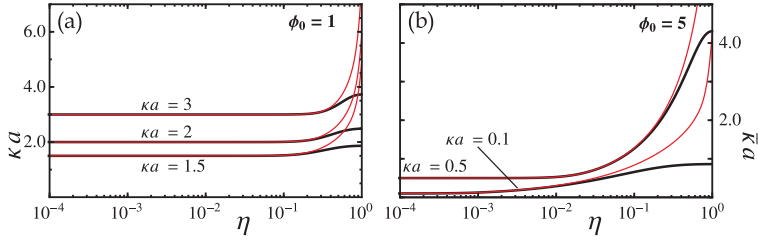


Figure 7.2: The effective inverse screening length $\bar{\kappa}a$ as a function of the packing fraction η for several reservoir screening parameters κa , for constant surface potentials (a) $\phi_0 = 1$ and (b) $\phi_0 = 5$ as represented by the thick curves. The thin curves denote $\bar{\kappa}$ as obtained from the association-dissociation model, with the chargeability z chosen such that the surface potential in the dilute limit $\eta \rightarrow 0$ equals ϕ_0 . Note that $\bar{\kappa} = \kappa$ in all cases for $\eta \rightarrow 0$.

model at high η , the number of counterions in the cell, and hence $\bar{\kappa}$, is also larger in the AD model.

7.4 Effective interactions and phase diagrams

Once the effective colloidal charge Z^* and the effective screening length $\bar{\kappa}^{-1}$ have been determined from the numerical solution of the PB equation in a Wigner-Seitz cell, either for constant-potential or association-dissociation boundary conditions, the effective interactions $u(r)$ between a pair of colloidal particles separated by a distance r follows, assuming DLVO theory, as

$$\frac{u(r)}{k_B T} = \begin{cases} \infty, & r < 2a; \\ \lambda_B \left(\frac{Z^* \exp(\bar{\kappa}a)}{1 + \bar{\kappa}a} \right)^2 \frac{\exp(-\bar{\kappa}r)}{r}, & r > 2a, \end{cases} \quad (7.12)$$

where we include a short-range hard-core repulsion for overlapping colloids and ignore Van der Waals forces (which is justified for index-matched particles). One could use Eq. (7.12) for the pair interaction to simulate (or otherwise calculate) properties of the suspension in a given state-point, e.g. whether the system is in a fluid or crystalline state. We restrict our attention here to the limiting case in which the colloidal particles are sufficiently highly charged and/or sufficiently weakly screened, that the pair-potential at contact satisfies $u(2a) \gg k_B T$, thereby effectively preventing direct particle-particle contact. In this limit the suspension can be effectively regarded as a point-Yukawa system that can be completely characterised by only *two* dimensionless parameters U and λ for the strength and the

range of the interactions, respectively. They are defined as

$$U = \left(\frac{Z^* \exp(\bar{\kappa}a)}{1 + \bar{\kappa}a} \right)^2 \frac{\lambda_B}{a} \left(\frac{3\eta}{4\pi} \right)^{1/3} \quad (7.13)$$

$$\lambda = \bar{\kappa}a \left(\frac{3\eta}{4\pi} \right)^{-1/3}, \quad (7.14)$$

such that the point-Yukawa interaction potential of interest, in units of $k_B T$, reads $U \exp(-\lambda x)/x$ with $x = r(N/V)^{1/3}$ the particle separation in units of the typical particle spacing. Note that *three* dimensionless parameters would have been needed if hard-core contact was not a low Boltzmann-weight configuration, e.g. then the contact-potential $\beta u(2a)$ (i.e. the inverse temperature), the dimensionless screening parameter κa , and the packing fraction η would be a natural choice. The mapping of the phase diagram of the point-Yukawa system onto hard-core Yukawa systems has been tested and verified explicitly by computer simulation [139].

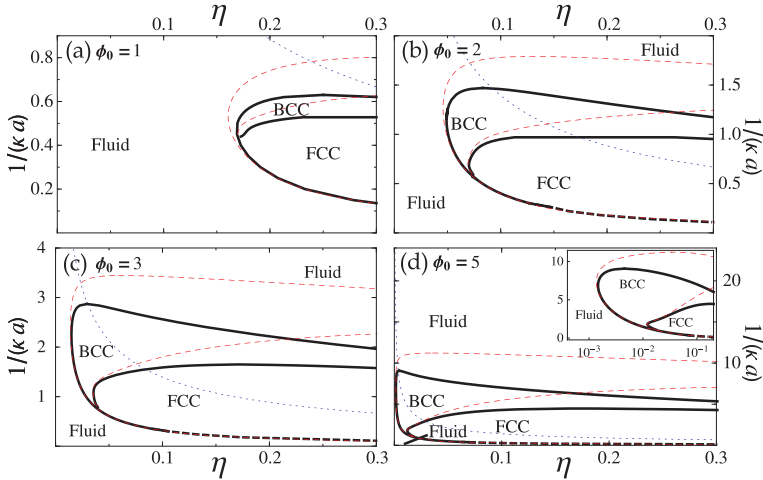


Figure 7.3: Phase diagrams in the packing fraction–screening length (η, κ^{-1}) representation for constant-potential colloids (radius $a/\lambda_B = 100$) interacting with the hard-core Yukawa potential of Eq. (7.12), for surface potentials $\phi_0 = 1, 2, 3$, and 5. The thick lines represent phase boundaries for the constant-potential model, and the thin dashed lines for the association-dissociation model with the surface potential equal to ϕ_0 in the dilute limit. The thick dashed lines indicate extrapolation of Eq. (7.15) beyond its strict regime of accuracy. The inset in the phase diagram for $\phi_0 = 5$ represents η on a logarithmic scale for clarity. The labels “Fluid”, “BCC”, and “FCC” denote the stable fluid, bcc, and fcc regions. We note that the very narrow fluid-fcc, fluid-bcc, and fcc-bcc coexistence regions are just represented by single curves. The thin dotted curves represent the estimated crossover-packing fraction η^* of Eq. (7.7), beyond which $Z(\eta) < Z(0)/2$.

The point-Yukawa system has been studied by simulation in great detail over the

years [136–139], and by now it is well known this model features a disordered fluid phase and two crystalline phases (face-centered cubic (fcc) and body-centered cubic (bcc)). Their first-order phase boundaries are well-documented, and can accurately be described by curves in the two-dimensional (λ, U) plane. Here, we employ the fits for the phase boundaries of point-Yukawa particles that were presented in Ref. [139], which were based on the results of Hamaguchi *et al.* [138] The melting-freezing line between the bcc crystal and the fluid is accurately fitted by

$$\begin{aligned} \ln U &= 4.670 - 0.04171\lambda + 0.1329\lambda^2 - 0.01043\lambda^3 \\ &\quad + 4.343 \cdot 10^{-4}\lambda^4 - 6.924 \cdot 10^{-6}\lambda^5, \end{aligned} \quad (7.15)$$

for $0 \leq \lambda \leq 12$,

and the bcc-fcc transition by

$$\begin{aligned} \ln U &= 97.65106 - 150.469699\lambda + 106.626405\lambda^2 \\ &\quad - 41.67136\lambda^3 + 9.639931\lambda^4 - 1.3150249\lambda^5 \\ &\quad + 0.09784811\lambda^6 - 0.00306396\lambda^7, \end{aligned} \quad (7.16)$$

for $1.85 \leq \lambda \leq 6.8$.

Here we exploit these empirical relations as follows. For given dimensionless colloid radius a/λ_B and screening constant κa , we calculate Z^* and $\bar{\kappa}a$ for various η for the CSP and the AD model in the Wigner-Seitz cell, as described in the previous section. These quantities can be used to compute the dimensionless Yukawa parameters U and λ from Eqs. (7.13) and (7.14), such that their phase and phase-boundaries are known from Eqs. (7.15) and (7.16).

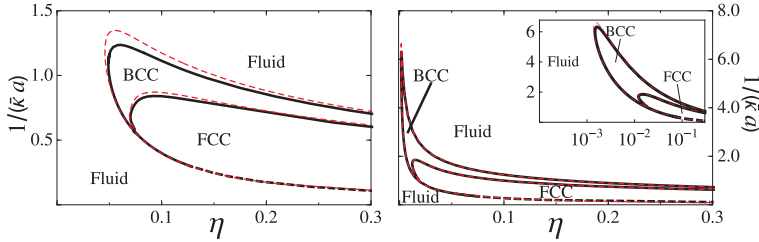


Figure 7.4: Phase diagrams in the packing fraction-*effective* screening length representation $(\eta, (\bar{\kappa}a)^{-1})$, for $a/\lambda_B = 100$, for constant-potential colloids with (a) $\phi_0 = 2$ and (b) $\phi_0 = 5$, as well as for charge-regulated colloids. Lines and symbols as in Fig. 7.3.

For $a/\lambda_B = 100$, Fig. 7.3 shows the phase diagrams that result from this point-Yukawa mapping procedure in the $(\eta, (\kappa a)^{-1})$ representation, for the CSP model (thick curves) with surface potentials (a) $\phi_0 = 1$, (b) $\phi_0 = 2$, (c) $\phi_0 = 3$, (d) $\phi_0 = 5$, and for the corresponding AD model (dashed curves). The dashed lines represent the phase boundary fits of Eqs. (7.15) and (7.16) outside their strict λ -regime of

applicability. We restrict attention to $\eta < 0.3$, as the point-Yukawa limit breaks down due to strong excluded-volume effects at higher packing fractions. An expected feature is the shift of the freezing curves to lower η for higher ϕ_0 , due to the higher (renormalised) charge and the stronger repulsions at higher ϕ_0 . Due to the higher charges in the AD model, its crystallisation regimes (dashed curves) extend to somewhat lower η 's and longer screening lengths than those of the CSP model (thick curves). However, the most striking feature of all these phase diagrams is the huge extension of the fluid regime: at high *and* at low screening length there is *no* crystalline phase at all (for $\eta < 0.3$), while at some intermediate salt concentrations the crystal phases are sandwiched in between an ordinary low-density fluid and a re-entrant fluid phase. This re-entrant fluid regime becomes more prominent with increasing zeta-potential ϕ_0 . The underlying physics of this finite-salt and finite- η regime where bcc and fcc crystals exist is the *discharging* of the colloids with increasing η and decreasing salt concentration: (i) although at high salt (small screening length) the colloidal charge is high, the screened-Coulomb interaction is then so short-ranged that the system resembles a hard-sphere system that will only crystallise at $\eta \simeq 0.5$; (ii) at low salt (long screening length) the colloidal charge is too low to have sizeable repulsions that drive crystallisation. Only at intermediate salt and intermediate colloidal packing the charge is high enough and the screening sufficiently long-ranged to drive crystallisation. The thin dotted curves in Fig. 7.3 represent the crossover packing fraction η^* of Eq. (7.7) beyond which the colloidal charge has been reduced to less than 50 percent of its dilute-limit value. Clearly, our expression for η^* indeed roughly coincides with the onset of the re-entrant fluid regime. Eq. (7.7) thus provides a quick guide to estimate where or whether re-entrant melting is to be expected at all. Interestingly, there are parameter values for κa and ϕ_0 (albeit in a narrow range) where a phase sequence fluid-bcc-fcc-bcc-fluid is predicted here upon increasing the colloidal packing fraction, i.e. not only a re-entrant fluid phase but also a re-entrant bcc phase. Moreover, for $\eta > 0.5$ one expects hard-sphere freezing into an fcc (or hcp) stacking on the basis of hard-sphere interactions, so the fcc phase is then also re-entrant.

Experimentally it is not always possible or convenient to characterise the screening in terms of the Debye length κ^{-1} of the (hypothetical) reservoir with which the suspension would be in osmotic equilibrium. Rather, one often measures the effective (actual) screening length $\bar{\kappa}$ in the suspension of interest. For this reason we replot in Fig. 7.4 the phase diagrams for $\phi_0 = 2$ and $\phi_0 = 5$ of Fig. 7.3, but now in the $(\eta, (\bar{\kappa}a)^{-1})$ representation. Interestingly, the CSP and AD model are now much closer together, and the re-entrant fluid phase appears even more pronounced in this representation.

In order to quantify in which finite salt-concentration regime bcc and fcc crystals are expected in a colloidal concentration series $0 < \eta < 0.3$, we analyse the maximum and minimum values of $\bar{\kappa}a$ at which these two crystal phases can exist, as a function of the zeta-potential ϕ_0 , for $a/\lambda_B = 100$. Fig. 7.5 shows the resulting screening-length regimes, both for bcc (solid curves) and fcc (dashed curve), where the lowest screening length for fcc crystals is set to zero because of the hard-sphere freezing

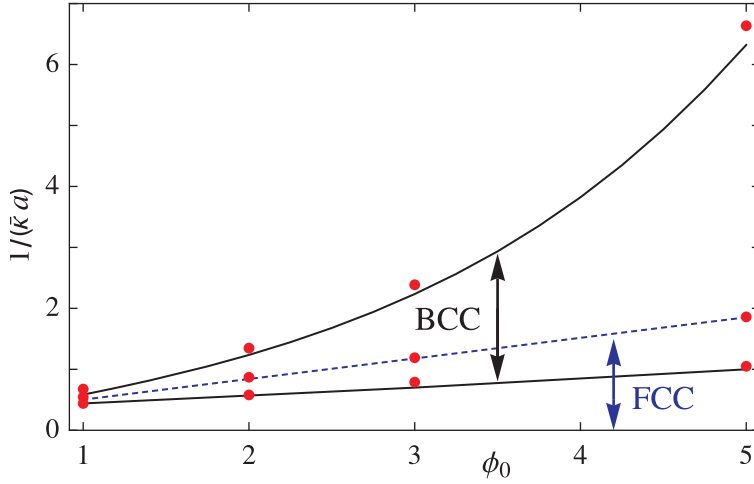


Figure 7.5: Maximum and minimum effective screening lengths where bcc and fcc can be found, as a function of the surface potential, assuming a constant surface potential for $a/\lambda_B = 100$. The bcc regime is in between the two solid lines, and the fcc regime below the dashed line. The points indicate the results from the AD model.

into fcc at $\eta = 0.5$ even for $1/\kappa a \rightarrow 0$ —of course we only restricted attention to $\eta < 0.3$ until now so strictly speaking also the fcc phase should have had a nonvanishing lower bound. Nevertheless, despite this small inconsistency, Fig. 7.5 clearly shows not only that a larger zeta-potential gives rise to a larger crystal regime, but also that for all ϕ_0 there is a limiting screening length beyond which neither fcc nor bcc crystals can exist, both for the CSP and the AD model.

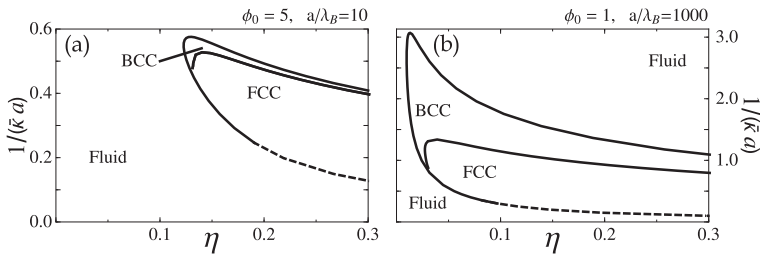


Figure 7.6: Phase diagrams in the packing fraction-effective screening length representation ($\eta, (\kappa a)^{-1}$), for constant-potential colloids with (a) $\phi_0 = 5$ for $a/\lambda_B = 10$ and (b) $\phi_0 = 1$ and for $a/\lambda_B = 1000$. Lines and symbols as in Fig. 7.3.

So far we focussed on $a/\lambda_B = 100$, which in aqueous suspensions corresponds to a colloidal radius of about 70nm. However the colloidal size regime can easily be a factor 10 larger or smaller, and for that reason we also consider the CSP model

for $a/\lambda_B = 10$ and 1000. In Fig. 7.6 we show the phase diagrams for the smaller colloids with $\phi_0 = 5$ in (a), and for larger colloids with $\phi_0 = 1$ in (b). Interestingly, they resemble those for $a/\lambda_B = 100$ shown in Fig. 7.4(a) and (b) for $\phi_0 = 2$ and 5, respectively, but the smaller colloids require a much higher potential while the larger ones only need a lower potential to obtain phase diagrams similar to those for $a/\lambda_B = 100$ —the phase diagram for $a/\lambda_B = 10$ at $\phi_0 = 1$ does not show a crystal phase at all for $\eta < 0.3$. In other words, given that $\phi_0 = 5$ is a rather high potential that may be difficult to achieve in reality while $\phi_0 = 1$ is frequently occurring, one concludes that re-entrant melting occurs in the largest salt-concentration regime (and is hence easiest observable by tuning the salt) for larger colloids.

7.5 Summary and conclusions

Within a Wigner-Seitz cell model we have calculated the bare charge Z , the renormalised charge Z^* , and the effective screening length $\bar{\kappa}^{-1}$ of colloidal spheres at a constant zeta-potential ϕ_0 . We find from numerical solutions of the nonlinear Poisson-Boltzmann equation that these constant-potential colloids discharge with increasing packing fraction and ionic screening length, in fair agreement with analytical estimates for the dilute-limit charge Z_0 in Eq. (7.6) and the typical crossover packing fraction η^* given in Eq. (7.7). We also show that the constant-potential assumption is a reasonably accurate description of charge regulation by an ionic association-dissociation equilibrium on the colloidal surface. We use our nonlinear calculations of Z^* and $\bar{\kappa}$ to determine the effective screened-Coulomb interactions between the colloids at a given state point, and we calculate the phase diagram for various zeta-potentials by a mapping onto empirical fits of simulated phase diagrams of point-Yukawa fluids. This reveals a very limited regime of bcc and fcc crystals: in order to form crystals, the charge is only high enough and the repulsions only long-ranged enough in a finite intermediate regime of packing fraction and salt concentrations; at high η or low salt the spheres discharge too much, and at high salt the repulsions are too short-ranged to stabilise crystals. In the salt-regime where crystals can exist, the discharging mechanism gives rise to re-entrant phase behaviour, with phase sequences fluid-bcc-fluid and even fluid-bcc-fcc-bcc-fluid upon increasing the colloid concentration from extremely dilute to $\eta = 0.3$.

The phase behaviour of constant-potential or charge-regulated colloids as reported here is quite different from that of constant-charge colloids, for which the pairwise repulsions do not weaken with increasing volume fraction or decreasing salt concentration. As a consequence constant-charge colloids have a much larger parameter-regime where crystals exist, and do not show the re-entrant behaviour [136–139]. The most direct comparison is to be made with the constant-charge phase diagrams of Fig.2 and Fig.4 of Ref. [139], where the charge is fixed such that the surface potential at infinite dilution corresponds to $\phi_0 \simeq 1$ and 2, respectively. Our theoretical findings can thus be used to gain insight into the colloidal charging mechanism by studying colloidal crystallisation regimes as a function of

packing fraction and salt concentration.

Acknowledgement We thank Frank Smalenburg and Marjolein Dijkstra for a pleasant collaboration, which also led to a beautiful project concerning experimental data on the phase-behaviour of colloids in the presence of AOT surfactant. The latter is expected to be published soon.

Appendix: Jellium model

Although it is numerically straightforward to solve the nonlinear PB equation (7.2) with BC's (7.3) and (7.4) in a spherical Wigner-Seitz cell of radius R , it may also be convenient to have analytic results that allow for quick estimates of the (order of) magnitude of the colloidal charge Z . A standard approach is to linearise the $\sinh \phi(r)$ term of Eq. (7.2), e.g. with $\phi(r) - \phi(R)$ as the small expansion parameter. The resulting solution is then of the form $\phi(r) = A \exp(-\bar{\kappa}r)/r + B \exp(\bar{\kappa}r)/r + C$, with $\bar{\kappa}$ defined in Eq. (7.11), $C = \phi(R) - \tanh \phi(R)$, and with integration constants A and B fixed by the two BC's. The algebra involved is, however, not very transparent.

A considerable simplification is achieved if we consider the so-called Jellium model, in which the central colloidal sphere is no longer considered to be surrounded by only cations and anions in a finite cell, but instead by cations, anions *and* other colloids with charge Z (to be determined) [14, 147, 148]. A nonlinear PB equation and BC's can then be written, for $r \geq a$,

$$\phi''(r) + \frac{2}{r} \phi'(r) = \kappa^2 \sinh \phi(r) - 4\pi\lambda_B Z n; \quad (7.17)$$

$$\phi(a) = \phi_0; \quad (7.18)$$

$$\phi'(\infty) = 0, \quad (7.19)$$

where it is assumed that the 'other' colloids are distributed homogeneously with density n . From this one derives directly that the asymptotic potential is given by

$$\sinh \phi(\infty) = \frac{4\pi\lambda_B Z n}{\kappa^2} = \frac{3\eta(Z\lambda_B/a)}{(\kappa a)^2}. \quad (7.20)$$

Now linearising $\sinh \phi(r)$ with $\phi(r) - \phi(\infty)$ as the small expansion parameter gives rise to the solution

$$\phi(r) = \phi(\infty) + (\phi_0 - \phi(\infty)) \frac{\exp(-\tilde{\kappa}(r-a))}{r/a}, \quad (7.21)$$

where the effective screening length $\tilde{\kappa}^{-1}$ is defined by

$$\tilde{\kappa} = \kappa \sqrt{\cosh \phi(\infty)}. \quad (7.22)$$

We note that the average ion concentrations in the system, within the present linearisation scheme, is given by $c_{\pm} = \rho_s \exp(\mp \phi(\infty))$, such that the corresponding

screening length $\tilde{\kappa}^{-1}$ is given by $\tilde{\kappa}^2 = 4\pi\lambda_B(c_+ + c_-)$. In other words, the effective screening length $\tilde{\kappa}$ and the asymptotic potential $\phi(\infty)$ of this jellium model play exactly the same role as $\bar{\kappa}$ and $\phi(R)$ that we introduced before in the Wigner-Seitz cell. In particular, $\bar{\kappa}^{-1}$ and $\tilde{\kappa}^{-1}$ can be seen as the *actual* screening length in the suspension (in contrast to the screening length κ^{-1} of the ion reservoir).

From Eq. (7.21) the colloidal charge Z follows, using Eq. (7.5), as the solution of the transcendental equation

$$\frac{Z\lambda_B}{a} = (\phi_0 - \phi(\infty))(1 + \tilde{\kappa}a), \quad (7.23)$$

where one should realise that both $\phi(\infty)$ and $\tilde{\kappa}$ depend on $Z\lambda_B/a$ through Eqs. (7.20) and (7.22). It is possible to solve Eq. (7.23) explicitly in the dilute limit. For $\eta = 0$ one finds $\phi(\infty) = 0$ from Eq. (7.20), and hence $Z = Z_0$ given by Eq. (7.6). For finite but low-enough η for which $\phi(\infty) \ll 1$ one can ignore $\mathcal{O}(\eta^2)$ contributions, such that $\sinh \phi(\infty) \simeq \phi(\infty)$ and $\cosh \phi(\infty) \simeq 1$, to find Eq. (7.7) from the self-consistency condition Eq. (7.23).

Chapter 8

Charge regulation and ionic screening of patchy surfaces

Abstract

The properties of surfaces with charge-regulated patches are studied using non-linear Poisson-Boltzmann theory. Using a mode expansion to solve the non-linear problem efficiently, we reveal the charging behaviour of Debye-length sized patches. We find that patches charge to higher charge densities if their size is relatively small and if the patches are well separated. The numerical results are used to construct a basic analytical model which predicts the average surface charge density on surfaces with patchy chargeable groups.

8.1 Introduction

Most surfaces that are immersed in an aqueous solution obtain a net charge due to ion adsorption or dissociative processes at the surface. The resulting electrostatic force between such surfaces is essential for understanding the stability, osmotic pressure and flocculation behaviour of colloidal suspensions. In the standard (linear) screening picture, like-charged surfaces repel each other at distances of the order of the Debye screening length [16, 17, 130], due to overlapping clouds of screening ions in the vicinity of the two surfaces. This electrostatic repulsion, combined with short-range attractive Van der Waals forces if there is a dielectric contrast between the colloidal particles and the solvent, is a basic result of Derjaguin-Landau-Verwey-Overbeek (DLVO) theory which dates back to the 1940's [16, 17, 130]. More recent studies, based on nonlinear Poisson-Boltzmann theory, also find strictly repulsive electrostatic forces between pairs of like-charges surfaces [160–165]. Nevertheless, there are also experimental reports of attraction between like-charge colloids at ranges much longer than those of Van der Waals forces. Ion-ion correlations, which are ignored in the mean-field type Poisson-Boltzmann theory, might be an explanation for these observed attractions in the case of multi-valent ions [81–84, 91, 166, 167]. However, evidence for electrostatic attractions has also been

reported for suspensions with only monovalent ions [168–171], causing heated debates in the literature on the break-down of the classic DLVO theory due to many-body effects, the vicinity of glass walls, hydrodynamic forces, etc. Interestingly, it has also been suggested that *charge inhomogeneities* can be responsible for these attractions [172–176], where the heterogeneity of the surface charge may be due to an incidentally present or purposely designed underlying chemical structure, or by clustering of adsorbed surfactants.

Apart from the ill-understood electrostatic attractions in some systems, another good reason for considering heterogeneously charged surfaces in more detail stems from the fascinating recent advances in the chemical synthesis of a large class of novel patchy nanoparticles, featuring not only corners, edges, and facets due to their finite size, but also spots or stripes [108]. Understanding the large-scale self-assembly properties of these newly available nanoparticles is an important ongoing scientific quest that requires effective particle-particle interactions as an input. For this reason a better understanding is needed of the relations between the chemical heterogeneity of patchy particles, the resulting surface charge density, and the nature and geometry of the ionic screening cloud that ultimately dictates the effective electrostatic interactions. In this chapter we explore some of these relations within nonlinear Poisson-Boltzmann (PB) theory in the relatively simple geometry of chargeable stripes on a planar surface in contact with a bulk electrolyte.

In PB theory a key role is being played by the boundary conditions (BC's), in particular those on the surface between the suspending electrolyte and the suspended colloidal nanoparticles. The most common BC is to predescribe the surface charge density of the colloidal particle, thereby imposing a fixed discontinuity of the displacement field at both sides of the surface while the surface potential itself increases upon the approach of another like-charged surface. This type of constant-charge BC was shown to be realistic for e.g. strongly acidic homogeneous surfaces that ionise completely in a polar solvent such as water [177]. An alternative is to predescribe the electrostatic potential on the surface, such that the particles can adjust their charge density if another surface approaches. This constant-potential BC has turned out to be realistic for surfaces not too far from a point of zero charge [178]. It is not clear, however, which of these BC's is realistic for surfaces with a heterogeneous chemical composition. For instance, it is not trivial how the charge of a highly charged patch on an otherwise weakly charged or neutral surface is distributed, and how the induced electrostatic potential propagates to affect the charging of nearby surface groups of other patches. The problem requires us to treat the interplay between the electrostatic potential and the surface charge density at the more microscopic level of a chemical equilibrium of attaching and detaching ions as modeled by charge-regulation [157, 178–185]. Such an approach has been applied to fit force measurements between two homogeneously charged plates [157, 178, 182], or to compute forces between periodically modulated charged plates within linearised PB theory [186]. Here, however, we combine charge-regulation BC's with nonlinear PB theory for a single spatially heterogeneous surface.

Using a newly developed numerical scheme we will reveal how surfaces with finite-sized discrete patches [123, 186, 187] tend to charge up and get screened, where the full non-linear PB theory allows us to deal with highly charged patches next to oppositely charged or neutral areas with strongly varying ion concentrations perpendicular and parallel to the surface. Although the calculated charge distributions cannot directly be compared to experiments, the results form a direct stepping stone towards understanding the complex interactions between heterogeneously charged particles. We will investigate to what extent (small) patches with a different chemical composition can influence the overall charge of these surfaces.

8.2 Theory

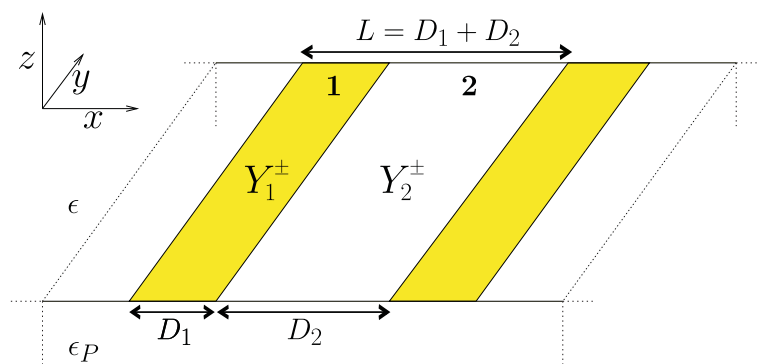


Figure 8.1: Pictorial representation of the model. The striped patches are shaded to distinguish these from the rest of the plate and will be referred to as region '1'. The area in between the patches will be referred to as region '2'.

We consider a solid medium in the half space $z < 0$, characterised by a dielectric constant ϵ_p . The surface of this medium at $z = 0$ is considered to be chemically heterogeneous, e.g. with a stripe pattern such as depicted in Fig. 8.1. The half space $z > 0$ is a bulk solvent with dielectric constant ϵ and volume V at temperature T . This solvent is assumed to be in thermal and diffusive equilibrium with a reservoir at $z \rightarrow \infty$ that contains point-like monovalent cations and anions, both at a concentration ρ_s . Since treating the ions in a mean-field fashion is in most of the cases an accurate approach in the case of monovalent ions in water or the more polar (higher ϵ) oils [80, 188], we describe the distributions of ions for $z > 0$ by the Boltzmann distributions $\rho_{\pm}(\mathbf{r}) = \rho_s \exp(\mp \Phi(\mathbf{r}))$. Here $k_B T \Phi(\mathbf{r})/e$ is the electrostatic potential at $\mathbf{r} = (x, y, z)$, with e the elementary charge and $k_B T$ the Boltzmann constant. We assume that $\Phi(x, y, z \rightarrow \infty) = 0$ in the reservoir, and that the densities of both ion species are zero for $z < 0$ due to hard-core repulsions. The Poisson equation relates the charge density to the Laplacian of the potential, $\nabla^2 \Phi(\mathbf{r}) = -4\pi \lambda_B (\rho_+(\mathbf{r}) - \rho_-(\mathbf{r}))$,

where we introduce the Bjerrum length $\lambda_B = e^2/\epsilon k_B T$. What follows is the Poisson-Boltzmann (PB) equation,

$$\nabla^2 \Phi(\mathbf{r}) = \begin{cases} \kappa^2 \sinh \Phi(\mathbf{r}) & z \geq 0; \\ 0 & z < 0, \end{cases} \quad (8.1)$$

where the Debye screening length is given by $\kappa^{-1} = (8\pi\lambda_B\rho_s)^{-1/2}$. At the fluid-solid interface, the presence of a surface charge density $e\sigma(x, y)$ and a stepwise change in dielectric medium gives rise to a boundary condition

$$\begin{aligned} \nabla\Phi(x, y, 0^+) \cdot \hat{z} &= -4\pi\lambda_B\sigma(x, y) \\ &+ \frac{\epsilon_P}{\epsilon} \nabla\Phi(x, y, 0^-) \cdot \hat{z}. \end{aligned} \quad (8.2)$$

Other boundary conditions ensure that the potential is continuous at $z = 0$, vanishes at infinity, and require that the electric field in the medium vanishes far away from the interface:

$$\Phi(x, y, 0^+) = \Phi(x, y, 0^-); \quad (8.3)$$

$$\lim_{z \rightarrow \infty} \Phi(x, y, z) = 0; \quad (8.4)$$

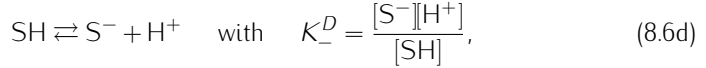
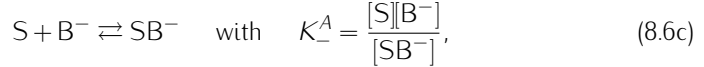
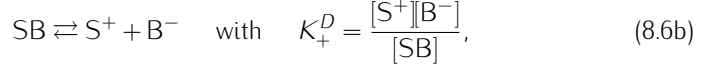
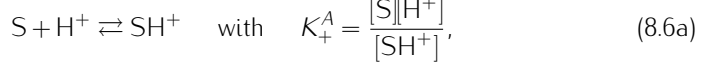
$$\lim_{z \rightarrow -\infty} \Phi'(x, y, z) = 0. \quad (8.5)$$

Here, and below, a prime denotes a partial derivative w.r.t. the z -coordinate. We remark that we are bound to the description of systems containing only monovalent ions as PB theory does not take the strong correlations into account that occur in the ionic charge distributions of multivalent ions. [81–84] Apart from giving only mean field results, standard PB theory does not account for the finite size of the ions in the system either. The hard-core repulsion of the ions may become important at high salt concentrations, and could in this case be added via a steric correction to the PB equation [189]. Corrections due to the finite size of the ions are also expected for cases where the typical size of the surface inhomogeneities becomes comparable to the size of the (hydrated) ions. Despite these shortcomings, there is still a large parameter regime in which our results are applicable, e.g. aqueous systems with monovalent ions in contact with surfaces containing nm-sized patches.

8.2.1 Charge regulation

The majority of models which apply PB theory assume either a fixed charge density or a fixed potential at surfaces. In reality the charging is often regulated; neither the charge density nor the surface potential is fixed, since both depend on the local density of ions in the surrounding liquid. There is a subtle interplay as the local surface charge density depends on the local surface potential and vice versa.

We consider 4 major charge generation mechanisms, involving cationic/anionic adsorption/desorption,



where S denotes a surface group, H^+ represent a cation, and B^- an anion, with concentrations $[S]$, $[H^+]$, and $[B^-]$ in the vicinity of the surface. Eqs. (8.6a) and (8.6c) describe associative charging in which an ion from the liquid is adsorbed at the surface. Eqs. (8.6b) and (8.6d) describe dissociative charging, where ions are released from the surface into the liquid. These chemical reactions are characterised by reaction constants $K_{\pm}^{A/D}$. We assume the charging to occur at discrete sites at the surface, and define a surface site density $m_{\pm}^A(x, y)$ and $m_{\pm}^D(x, y)$ for associatively and dissociatively chargeable sites respectively. Since each surface site is either charged or neutral, we have

$$[S] + [SH^+] = m_+^A(x, y), \quad (8.7a)$$

$$[S^+] + [SB] = m_+^D(x, y), \quad (8.7b)$$

$$[S] + [SB^-] = m_-^A(x, y), \quad (8.7c)$$

$$[S^-] + [SH] = m_-^D(x, y). \quad (8.7d)$$

Using the Boltzmann relations $[H^+] = \rho_s \exp[-\Phi(x, y, 0)]$ and $[B^-] = \rho_s \exp[+\Phi(x, y, 0)]$ for the ion densities at the surface $z = 0$, we can express the associative and dissociative surface charge densities $\sigma_{\pm}^A = [SH^+]$, $[SB^-]$ and $\sigma_{\pm}^D = [S^{\pm}]$, respectively, as

$$\sigma_{\pm}^A(x, y) = \frac{m_{\pm}^A(x, y)}{1 + \frac{K_{\pm}^A}{\rho_s} \exp(\pm\Phi(x, y, 0))}; \quad (8.8a)$$

$$\sigma_{\pm}^D(x, y) = \frac{m_{\pm}^D(x, y)}{1 + \frac{\rho_s}{K_{\pm}^D} \exp(\pm\Phi(x, y, 0))}, \quad (8.8b)$$

for both types of charging. Here, $\Phi(x, y, 0)$ is the surface potential, which for heterogeneous surfaces is a function of the lateral coordinates x and y . Note that *all* surface chemistry is encoded in $m_{\pm}^{A/D}(x, y)$ and equilibrium constants $K_{\pm}^{A/D}$, which

we consider as input parameters in this work.

For simplicity we only consider stripe-like surface inhomogeneities in this work, such that the charge and the surface potential only depend on x and not on y , see Fig. 8.1. Translational invariance in the y -direction follows directly by assuming $m_{\pm}^{A/D}(x, y) = m_{\pm}^{A/D}(x)$. Note that the potential $\Phi(x, y, z) = \Phi(x, z)$ does depend on a lateral coordinate and a normal one.

The common case that only a small fraction of the sites charges ($\sigma \ll m$) necessarily corresponds to the case that the unity in the denominators of Eqs. (8.8a) and (8.8b) is negligible compared to the other term. In other words, for all cases that the surface is only charged to a fraction of its maximum it is safe to omit the unity from Eqs. (8.8a) and (8.8b). For most associative reactions this approximation is fine, as was already argued by Grahame in 1947 [190]. For dissociating surfaces one should be more cautious, especially at low ionic strengths ρ_s [191]. In the remainder of this study we employ this assumption throughout, as it reduces the number of independent parameters vastly. This is immediately seen by introducing the dimensionless total surface charge density

$$y(x) = 4\pi\lambda_B\kappa^{-1} \left(\sigma_+^A(x) + \sigma_+^D(x) - \sigma_-^A(x) - \sigma_-^D(x) \right), \quad (8.9)$$

which reduces Eq. (8.8a) and (8.8b) within the small-charge-fraction limit to

$$y(x) = Y^+(x)\exp(-\Phi(x, 0)) - Y^-(x)\exp(+\Phi(x, 0)), \quad (8.10)$$

where

$$Y^{\pm}(x) = \kappa \left(\frac{m_{\pm}^A(x)}{2K_{\pm}^A} + \frac{m_{\pm}^D(x)K_{\pm}^D}{2\rho_s^2} \right). \quad (8.11)$$

Note that Eq. (8.11) defines a dimensionless quantity which is not necessarily of the order of unity. Depending on the material properties and ion concentrations, both $Y^+(x)$ and $Y^-(x)$ can easily vary over many decades. From now on we refer to $Y^+(x)$ and $Y^-(x)$ as the positive and negative *chargeability*, respectively. Eqs. (8.2), (8.9) and (8.10) give rise to the boundary condition for our model,

$$\begin{aligned} \Phi'(x, 0^+) &= \frac{\epsilon_P}{\epsilon} \Phi'(x, 0^-) + \kappa Y^-(x) \exp(+\Phi(x, 0)) \\ &- \kappa Y^+(x) \exp(-\Phi(x, 0)). \end{aligned} \quad (8.12)$$

The latter equation together with Eqs. (8.1) and (8.3)-(8.5) forms a closed set of equations to solve the electrostatic potential above and within the solid medium.

8.2.2 The homogeneous limit

To the best of our knowledge, there are no analytic solutions to the nonlinear Poisson-Boltzmann (PB) equation for inhomogeneously charged surfaces. However,

it can be solved analytically in the case of a single homogeneously charged plate, see for example Ref. [129]. Considering a homogeneous surface charge density $\sigma(x, y) = \sigma_H$, the potential can be written as

$$\Phi_H(z) = \begin{cases} 2 \ln \frac{1 + \gamma \exp[-\kappa z]}{1 - \gamma \exp[-\kappa z]} & z \geq 0; \\ \Phi_H(0) & z < 0, \end{cases} \quad (8.13)$$

where $\gamma = (\sqrt{4 + y_H^2} - 2)/y_H$, and $y_H = 4\pi\lambda_B\kappa^{-1}\sigma_H$ is the dimensionless surface charge density as defined in Eq. (8.9), now for a homogeneously charged plate. Note that the solid medium is free of electric fields in this case, and because of this, Eq. (8.13) is independent of the dielectric constant of the plate, $\epsilon\rho$. By using Eq. (8.10) for the mechanism to account for associative and dissociative charging we find an expression for the surface potential of homogeneously chargeable plates. In general, for a (positive) homogeneous chargeability $Y^+(x) = Y_H$ (and $Y^-(x) \equiv 0$) we obtain from Eqs. (8.10) and (8.13) that the surface potential is given by

$$\Phi_H(0) = 2 \ln \begin{cases} \frac{2}{\sqrt{3}} \cos \left(\frac{1}{3} \arctan \left(\sqrt{\frac{4}{27Y_H^2} - 1} \right) \right) & \text{if } 0 \leq Y_H < \frac{2}{3\sqrt{3}}; \\ \frac{\frac{2}{3}^{1/3}}{\left(9Y_H + \sqrt{3}\sqrt{27Y_H^2 - 4}\right)^{1/3} + \frac{\left(9Y_H + \sqrt{3}\sqrt{27Y_H^2 - 4}\right)^{1/3}}{18^{1/3}}} & \text{if } Y_H \geq \frac{2}{3\sqrt{3}}. \end{cases} \quad (8.14)$$

The regime $Y_H < 1$ is associated with the regime where linear Poisson–Boltzmann theory holds, as we can easily check that surface potentials do not exceed unity here. By taking the inverse of Eq. (8.13) we obtain a relation which is well-known from Gouy–Chapman theory,

$$y_H = 2 \sinh \frac{\Phi_H(0)}{2}, \quad (8.15)$$

and this can be used in combination with Eq. (8.14) to find the explicit relation $y_H(Y_H)$ between charge and chargeability of a homogeneous plate. The limiting cases are

$$y_H \approx \begin{cases} Y_H & \text{if } Y_H \ll 1; \\ Y_H^{1/3} & \text{if } Y_H \gg 1. \end{cases} \quad (8.16)$$

Physically this means that the charging of a weakly chargeable surface is relatively efficient, whilst a highly chargeable surface only gains charge with the cube root of the density of chargeable sites. Both regimes of Eq. (8.16) can easily be distinguished in a double-logarithmic plot; the solid line in Fig. 8.7 consists of two straight lines with slopes 1 and 1/3, respectively, with a cross-over between both regimes at $Y_H \approx 1$.

8.2.3 Mode expansion

We develop a numerical scheme to solve the PB equation in the case of a striped patchiness on the surface, described by $\sigma(x, y) = \sigma(x)$, such that the charge distribution on the surface only changes in the \hat{x} direction. We assume inhomogeneities to be periodic with period L , such that $\sigma(x + L) = \sigma(x)$, and we can thus write

$$\sigma(x) = \sum_{k=-M}^M \sigma_k \eta_k(x), \quad (8.17)$$

where $\eta_k(x) \equiv \frac{1}{\sqrt{\kappa L}} \exp(\frac{i2\pi kx}{L})$ with $k \in \mathbb{Z}$ are conveniently normalised (Fourier-) modes and σ_k are the corresponding amplitudes in the expansion, given by $\sigma_k = \kappa \int_0^L \sigma(x) \eta_k(-x) dx$. Note that this charge density is not known beforehand, as it depends on the surface potential through Eq. (8.10). The number M signifies a high-wavenumber cut-off, that we will empirically choose to be large enough to describe the essential large-wavelength physics. We will develop a method to calculate the electrostatic potential $\Phi(x, z)$ at and above the plate, $z \geq 0$. Since this is a function which will be subject to the L -periodic symmetry as a function of x , such that $\Phi(x, z) = \Phi(x + L, z)$ for all x, z , it can be written as

$$\Phi(x, z) = \sum_{k \in \mathbb{Z}} \phi_k(z) \eta_k(x), \quad (8.18)$$

where $\phi_k(z)$ is the mode amplitude of the Fourier component $\eta_k(x)$. One easily checks that functions of the form $\phi_k(z) \eta_k(x) = c_k \exp(\frac{|k|Lz}{2\pi}) \eta_k(x)$, with c_k a constant, solve the PB equation for $z < 0$, and satisfy boundary condition (8.5). This solution can be put into Eq. (8.2), to yield boundary conditions in terms of the mode amplitudes given by

$$\epsilon \phi_k'(0^+) = -4\pi\epsilon\lambda_B \sigma_k + \frac{2\pi|k|}{L} \epsilon_P \phi_k(0); \quad (8.19)$$

$$\lim_{z \rightarrow \infty} \phi_k(z) = 0. \quad (8.20)$$

The task is now to find PB-like differential equations for every mode $\phi_k(z) \eta_k(x)$ in the regime $z > 0$ by inserting the mode expansion (8.18) into the PB equation (8.1). The left hand side can be treated easily, yielding

$$\nabla^2 \Phi(\mathbf{r}) = \sum_{k \in \mathbb{Z}} \left(\phi_k''(z) - \left(\frac{2\pi k}{L} \right)^2 \phi_k(z) \right) \eta_k(x), \quad (8.21)$$

where a prime denotes a derivative with respect to z . The $\sinh \Phi(\mathbf{r})$ on the right side of the PB equation is a nonlinear function, which gives rise to the couplings between mode amplitudes $\phi_k(z)$ for all $k \in \mathbb{Z}$. This complicates the calculation of

the solution of these modes; in general it will not be possible to find solutions for every mode separately.

Only in the case that one describes a weakly charged system, such that the potential is small, and thus $\sinh \Phi(\mathbf{r}) \approx \Phi(\mathbf{r})$, the PB equation becomes linear, $\nabla^2 \Phi(\mathbf{r}) \approx \kappa^2 \Phi(\mathbf{r})$. In this case the modes decouple, and using Eq. (8.21) the solution for each mode is found to be

$$\phi_k(z) = a_k \exp(-\kappa_k z) + b_k \exp(\kappa_k z), \quad (z \geq 0) \quad (8.22)$$

where a_k and b_k are integration constants and $\kappa_k = \sqrt{\kappa^2 + \left(\frac{2\pi k}{L}\right)^2}$ is the mode-dependent screening parameter. Note that in the present case of a single plate the coefficient b_k vanishes because of Eq. (8.20), and we find by applying Eq. (8.19) the amplitudes

$$a_k = \frac{4\pi\epsilon\lambda_B\sigma_k L}{\epsilon\kappa_k L + 2\pi|k|\epsilon_P}. \quad (8.23)$$

Fig. 8.2a shows the relation between the screening parameters κ_k and the (dimensionless) periodicity of the system κL . Besides the independence of κ_0 on κL , it shows that $\kappa_k \gg \kappa_0$ for small κL . This means that wave-like inhomogeneities in the electrostatic surface potential always vanish within a few wavelengths normal to the surface. Therefore, inhomogeneities with short wavelengths are screened over shorter distances than a Debye length. From Fig. 8.2a and from the definition of κ_k it can be concluded that all inhomogeneities in the potential must have essentially disappeared at distances of the order of L from the surface as $\kappa_k \gg 1/L$ for all $|k| \neq 0$.

Fig. 8.2b shows some of the corresponding mode coefficients a_k , for $k = 1, 3$, and 7 , all for $\epsilon_P = 0$ (non-penetrating fields) and $\epsilon_P = \epsilon$ (index-matched solvent and plate). In the figure we divided by a_0 to show the inhomogeneous amplitudes relative to the homogeneous background. All coefficients can be calculated by using the σ_k following from a surface with charged ($y=1$) and uncharged ($y=0$) stripes of equal width. This is a fixed charge density and therefore we do not account for association/dissociation reactions at the surface here. The coefficients a_k , and therefore the inhomogeneities in the potential, are relatively small but may become large for systems with a larger periodicity ($\kappa L \gg 1$). This is analogous to the fact that at small periodicities (with respect to κ^{-1}) the potential is not able to laterally adapt to the oscillations in the surface charge and becomes more homogeneous, whilst at very high κL it is able to take the form of a step function.

The choice of the ratio of the dielectric constants between the plate and the liquid is of importance. We see from Fig. 8.2b that if we choose an index-matched plate and solvent, corresponding to the situation that the fields are able to penetrate into the solid medium, the coefficients a_k become significantly lower (in absolute value) than if this ratio is chosen close to zero, where we do not find any fields in

the medium. In the $\epsilon_P = 0$ case, inhomogeneities in the charge distribution will have a larger effect on the inhomogeneity of the associated electrostatic potential, as the polarisability of the solid medium is not able to compensate any inhomogeneities in the electrostatic potential from within the plate. Since every ion close to a body with a lower dielectric constant will be repelled by its own image charge, typically a small depleted zone of ions appears close to the surface. This image-charge effect is, however, only significant if $(\kappa\lambda_B \ll 1)$ [192], and can thus be ignored in most aqueous electrolytes. Moreover, although we do not include this correction in our model, the effect of image charges of the ionic double layer is naturally included by the chosen boundary condition at the surface $z = 0$.

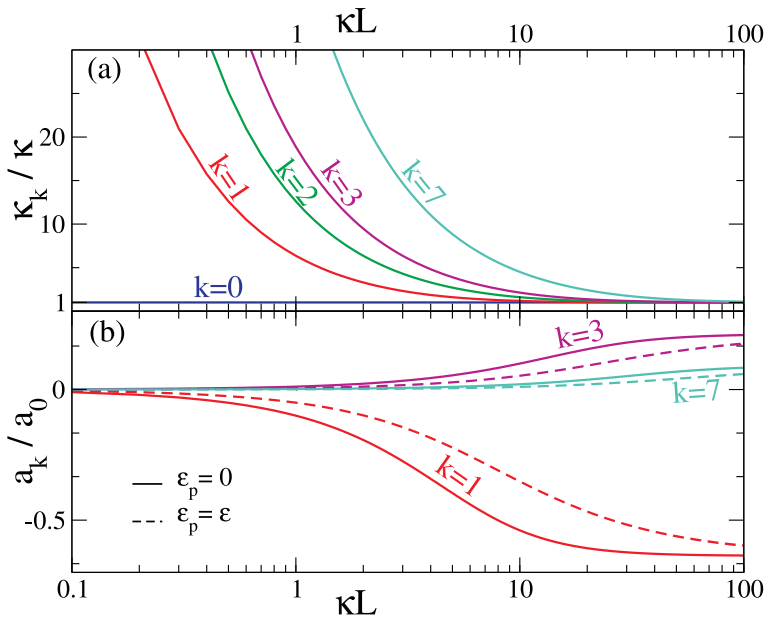


Figure 8.2: The mode-dependent screening parameter κ_k (a) and mode amplitudes a_k (b) for several k as a function of the periodicity parameter in the system, in (b) for charged ($y = 1$) and uncharged ($y = 0$) stripes of equal width. The solid lines in (b) correspond to the case $\epsilon_P = 0$, whilst the dashed lines show data for $\epsilon_P = \epsilon$.

8.3 Results

8.3.1 Charging of stripes

In the general nonlinear case the mode amplitudes will not be exponential functions of the distance like in Eq. (8.22). Since no analytical form is known we develop

a method to solve for these functions numerically, its details are described in the Appendix. Using the theory in combination with the numerical method we can in principle calculate the charging of any periodic configuration of chargeable parallel stripes on a planar surface. Here, we focus on a plate coated with stripes with periodicity $L = D_1 + D_2$, where D_1 and D_2 are the widths of the striped regions with dimensionless chargeabilities Y_1^\pm and Y_2^\pm respectively, such that

$$Y^\pm(x) = \begin{cases} Y_1^\pm & \text{if } x \in \text{region 1;} \\ Y_2^\pm & \text{if } x \in \text{region 2.} \end{cases} \quad (8.24)$$

Regions '1' and '2' are also shown in Fig. 8.1. We focus mostly on $Y_1^+ \equiv Y$, $Y_1^- = Y_2^\pm = 0$, and $\epsilon_P/\epsilon \ll 1$, which corresponds to uncharged areas (regions '2') separating stripes with positive chargeability Y on a low-epsilon plate in contact with a high-epsilon liquid such as water. For this particular calculation it suffices to choose $M = 64$ modes, a z -grid of $N = 2000$ points extending to $z = 5\kappa^{-1}$.

For a periodicity of 10 Debye lengths, $\kappa L = 10$, a charged stripe of width $D_1 = 3.1\kappa^{-1}$ (such that $D_2 = 6.9\kappa^{-1}$), and several chargeabilities $Y \in \{0.1, 1, 10, 100\}$, Fig. 8.3(a) shows the x -dependence of the chargeability, which is a step function. This is the starting point of our calculation, and we calculate the electrostatic potential $\Phi(x, z)$ via the iterative scheme that was described above. Fig. 8.3(b) shows the resulting surface potential $\Phi(x, z = 0)$ for the four values of Y of Fig. 8.3(a). For each Y , the thin horizontal dotted lines show the surface potential in the case that the stripe would have infinite width ($D_1 \gg \kappa^{-1}$) by using the analytical solution to the planar-PB Eqs. (8.14)-(8.15), i.e. the surface potential of a homogeneously charged plate. In the present system the homogeneous surface potential limits the actual surface potential from above. Since the stripes are relatively broad ($D_1 > \kappa^{-1}$), the calculated surface potential approaches this limit, which we will call the homogeneous limit from now on, at the center of the stripe. Typical length scales over which the potential varies laterally are clearly of the order κ^{-1} , as expected. Fig. 8.3(c) shows the dimensionless surface charge $y(x)$, which is related to the surface potential via Eq. (8.10). We see that the charge density at the center of the stripe is well described by that of a homogeneously charged plate. By contrast, a relatively high charge builds up close to the edges of the stripe. For $Y \gg 1$, in the nonlinear screening regime, the charge density at these edges largely exceeds the values we find at the center. The reason is the nearby neutral surface, which results in a surface potential which is lower at the edge of the stripe than at its center. The charging of the surface groups, which is normally limited by the induced rise of the electrostatic potential according to Eq. (8.10), can therefore be stronger close to the edges. As a result, the average charge density of a stripe can be much higher than what one would expect for homogeneously charged plates with the same chemical properties. The reason that we only observe this effect (deeply) in the *nonlinear* regime is because the surface potentials must be significant ($\Phi(x) \geq 1$), such that the Boltzmann factors which govern the surface charge distribution, see Eq. (8.10),

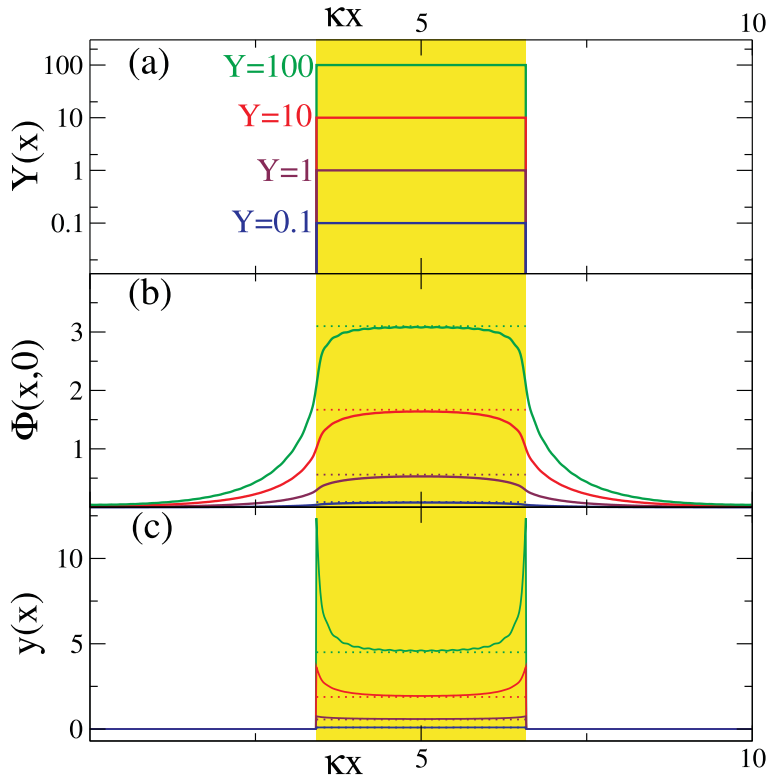


Figure 8.3: Positional (lateral) dependence of (a) the chargeability, (b) the surface potential and (c) the dimensionless surface charge density of a striped patchy surface with periodicity $L = 10\kappa^{-1}$ and patch stripe width $D_1 = 3.1\kappa^{-1}$, for several stripe chargeabilities. The shaded area shows the position of the stripe on the plate, and the horizontal dotted lines in (b) and (c) show values we would obtain for infinitely wide stripes.

deviate strongly from unity.

We checked that the results we obtain do not depend on the finite grid size and the number of included modes characterised by N and M , respectively; even the curves obtained with $M = 16$ and $N = 1000$ are indistinguishable from all those in Fig. 8.3. It should be noticed that in the case we choose M too small, instead of giving inaccurate results, the iterative scheme does often not converge anymore, such that no solution is found at all.

The two panels in Fig. 8.4 each show the charge density $y(x)$ for $Y = 10$ as was calculated in Fig. 8.3(c) for $\kappa D_1 = 3.1$ and $\kappa L = 10$ by a dashed line, while the full curve denotes $y(x)$ in the case of a modified parameter set. It illustrates cases

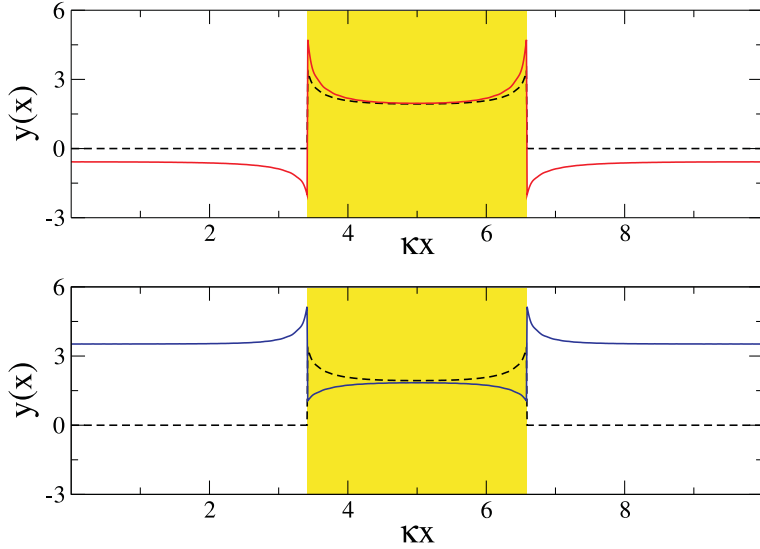


Figure 8.4: Positional (lateral) dependence of the dimensionless surface charge density of a striped patchy surface with periodicity $L = 10\kappa^{-1}$ and stripe width $D_1 = 3.1\kappa^{-1}$. We indicated the position of the stripe by the shaded areas. Both (a) and (b) show a dashed line which shows data corresponding to $Y = 10$ as in Fig. 8.3(c), whilst the solid lines show the effect of setting the chargeability of the surrounding plate to (a) $Y_2^- = 1$ in combination with $Y_2^+ = 0$ and (b) $Y_2^+ = 50$ (in combination with $Y_2^- = 0$.)

where the surrounding surface is chargeable as well. Fig. 8.4(a) shows a situation where the surrounding stripe is able to charge slightly negatively (with chargeability $Y_2^- = 1$). The presence of strong peaks of (opposite) excess charge at the edges of the stripes demonstrates that this presence of a chargeable surface with opposite sign of charge enhances the charging of the adjoining area. If the surrounding stripe is chosen to be more positively chargeable ($Y_2^+ = 50$) than the original one, as in Fig. 8.4(b), the stripe and the surrounding surface change roles. At the interface between the two regions the potential now is higher than at the center of the stripe, having a value somewhere in between the homogeneous limits of both stripes. This causes the charge density to peak just outside the original stripe whilst inside it shows sharp minima at the edges.

The distribution of charge at the chargeable stripe depends on the width and the spatial periodicity of the stripes. This is depicted in Fig. 8.5, where the charge density $y(x)$ for $Y = 10$ is plotted like in Fig. 8.3(c), now for various D_1 and L . Figs. 8.5(a) and (b) show the effect of changing the width of the stripes but deal differently with the size of region in between the stripes. In Fig. 8.5(a) the stripe periodicity is kept fixed at $L = 10\kappa^{-1}$, such that the stripe-fraction of the surface

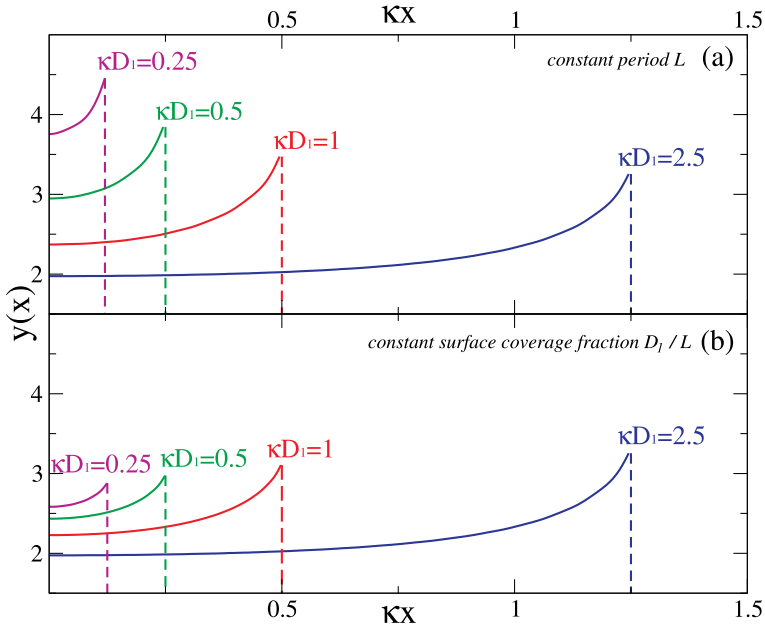


Figure 8.5: Surface charge-density profiles $y(x)$ of a striped patchy surface with $Y = 10$ for various stripe widths D_1 and spatial periodicities L , here as a function of the distance to the center of the charged stripe. In view of the symmetry we only plot half a period. The data in (a) is calculated using the fixed value of $\kappa L = 10$, whilst in (b) we use $L = 2D_1$. The vertical dashed lines indicate the edges of the stripes, beyond which $y(x) = 0$.

increases with increasing stripe width D_1 . In Fig. 8.5(b) the stripe periodicity is set to $L = 2D_1$, for several D_1 , such that the surface coverage fraction of the stripes remains fixed at 50%. The numerical results in Fig. 8.5(a) clearly show that smaller stripes at a fixed stripe periodicity L gain a higher charge density. From Eq. (8.10) it follows that the maximum charge density will occur for infinitesimally thin stripes, since the surface potential at the stripe will vanish in that case. In this limit, the corresponding charge density is $y(x) = Y$, for all x at the stripe. The results for a constant surface coverage in Fig. 8.5(b) fraction also show that thin stripes gain the highest average charge density, although the maximal charge density at the edges decreases a little. The increase is less pronounced than in Fig. 8.5(a) since now the width of the charge-neutral region in between the stripes scales with the width of the stripes. Therefore, thin stripes in Fig. 8.5(b) are relatively close to their neighboring stripes, and will hinder each other in gaining charge. One can show that the maximum charge density will again be found for infinitesimally thin stripes, for which the system reduces to an essentially homogeneously chargeable plate with chargeability $Y_H = YD_1/L$.

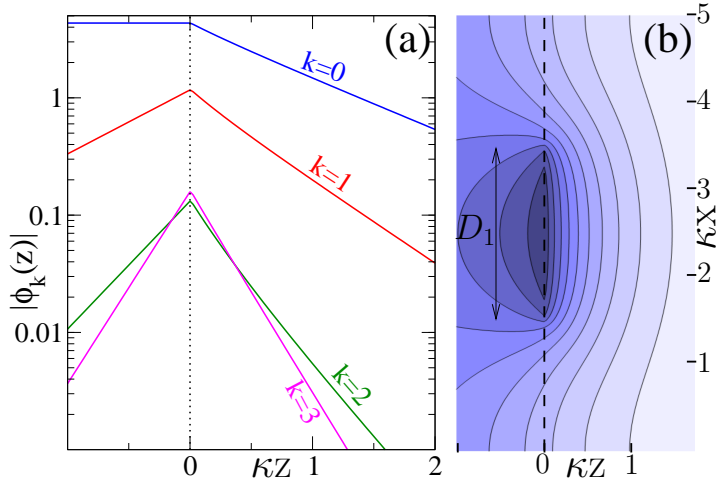


Figure 8.6: Results of the numerical calculation for the electrostatic potential of a striped patchy surface with periodicity $L = 5\kappa^{-1}$, stripe width $D_1 = 2\kappa^{-1}$ and chargeability $Y = 100$, showing the absolute value of the first 4 mode amplitudes of the electrostatic potential in (a), and a contour plot of the electrostatic potential at both sides of the interface using the calculated mode amplitudes (b). A contour line borders the darkest area at $\Phi(x, z) > 2.75$ and the lightest area at $\Phi(x, z) < 0.5$, with steps of 0.25 in between. The vertical dashed line in both figures denotes the location of the interface between the solid medium (left) and the solvent (right). For these calculations we choose an index-matching plate and liquid, $\epsilon = \epsilon_P$, such that the electric field is able to penetrate into the solid medium.

Fig. 8.6 shows the electrostatic potential around the plate for $\kappa L = 5$, $\kappa D_1 = 2$, $Y_2^\pm = Y_1^- \equiv 0$, $Y_1^+ = 100$ and $\epsilon_P = \epsilon$. This choice of the dielectric constants is such that electric fields do not vanish inside the solid medium. In Fig. 8.6(a) the logarithmic plot shows nearly exponential decay of the mode amplitudes $\phi_k(z)$ for $k = 0, \dots, 3$. Deviations from a straight line are due to nonlinear couplings between the modes, and slopes far away from the surface are the mode-dependent screening parameters κ_k . It can be seen that, for this choice of ϵ_P , the nonzero modes also give rise to an electric field inside the solid medium, and for high k the screening on both sides of the interface is equally efficient, as there are almost no ions involved. Fig. 8.6(b) shows a contour plot of the potential $\Phi(x, z)$ around the charged interface. It shows a local increase of the potential close to the stripe, which is caused by a local high charge density. The inhomogeneity in the potential persists for a few screening lengths into the liquid, as the stripe width is larger than the screening length, and thus ionic screening is the dominant type of screening there. In the solid medium ionic screening is not possible, and the inhomogeneity persists over a range of the order of the width of the stripe as was found below Eq. (8.18).

We now return to the case of chargeable stripes on an otherwise neutral plate, and define the average charge density on a stripe

$$\bar{y} = \frac{1}{D_1} \int_{x=0}^L y(x) dx. \quad (8.25)$$

Fig. 8.7 shows \bar{y} as a function of chargeability Y for multiple choices of the stripe geometry parameters D_1 and D_2 . All curves show, as expected, that the charge increases with the chargeability. It illustrates, however, that the charging of the stripes

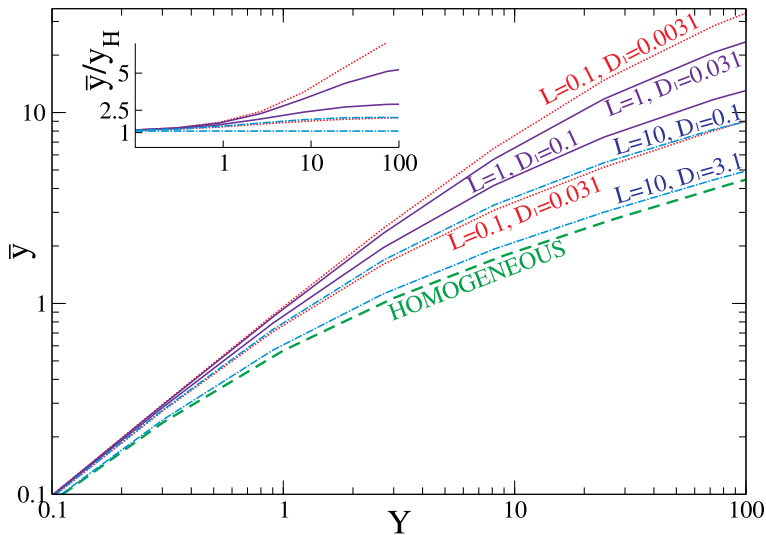


Figure 8.7: Average charge density on a chargeable stripe surrounded by charge-neutral surface for various stripe widths D_1 and periodicity L , denoted in units of κ^{-1} , plotted as a function of the stripe chargeability Y . The medium has a dielectric constant $\epsilon_P \ll \epsilon$. The thick dashed line corresponds to the infinite stripe-width limit for which we use the analytical result for homogeneously chargeable plates. Using the same data, the inset shows the charge density relative to this homogeneous limit.

strongly depends on their width and the distance in between two successive stripes. Charge densities are increased either by narrower stripes or by larger stripe–stripe distances, the strongest charging occurs for narrow stripes with relatively much space in between. This is intuitively clear since for stripes that are rather separated the charging of the edges is not hindered by the charge of neighboring stripes. Moreover, narrow stripes have relatively more edge surface. For broad stripes this gain at the edges is small compared to the charge at the center, and we see from the line for $\kappa D_1 = 3.1$ and $\kappa L = 10$ that the charge density indeed approaches the homogeneous limit ($D_1 = L$), given in Eqs. (8.14)–(8.15) and limiting behaviour (8.16). By contrast,

the narrower stripe of width $D_1 = 0.1\kappa^{-1}$ and the same periodicity $L = 10\kappa^{-1}$ has, for $Y \gg 1$, a charge density that is a factor ~ 2 higher than the homogeneous limit, while the relative increase of \bar{y} compared to y_H can be a factor 5 for extremely narrow patches with $D_1 = 0.0031\kappa^{-1}$ and $L = 0.1\kappa^{-1}$, as can be seen in the inset of Fig. 8.7. Furthermore, we note that $\bar{y} = Y$ in the low-charge limit $Y \ll 1$. This is not surprising either, as in this limit any charge, regardless its position on the surface, is essentially 'alone' in a vanishingly small potential; the vicinity of a neutral area '2' or an essentially neutral stripe '1' is indistinguishable in that case.

8.3.2 Analytical approximation

As a way to better understand and quantify the charging mechanism of the patches, we now propose a method to estimate the stripe charge densities by an analytic procedure and check if the right physics emerges. The key element in the method is the fact that the charging of different surface groups is correlated. This correlation is mediated by the electrostatic potential and logically the (longest) correlation length is of the order of the screening length, as long as we use the assumption that $\epsilon_P \ll \epsilon$. This correlation implies that a small area of charge-neutral plate around every stripe is involved in the charging as well. For the geometry of current interest this means we can think of an extra strip of width s on each side of the charged patch of width D_1 , as illustrated in Fig. 8.8. Now we presume that the stripe including the extra area charges up like a homogeneously charged plate, such that we can apply the analytic expressions (8.14)-(8.15) from planar PB theory with an effective (decreased) chargeability $\tilde{Y} = Y \frac{D_1}{D_1 + 2s}$ for the enlarged stripe.

The strip width s depends on the local screening length, and therefore we set $s = \min(\alpha\bar{\kappa}^{-1}, D_2/2)$, with α a fit parameter and $\bar{\kappa}^{-1}$ the effective screening length defined below. The minimum condition is used to prevent overlaps, as the size of the additional strip area cannot exceed the size of the uncharged region in between the charged stripes. The effective screening parameter $\bar{\kappa}$ is determined by the average electrostatic potential around the edge. The relation stems from PB-linearisation procedures and is given for example in ref. [18, 21, 193]. Since the local surface potential at the strip must be somewhere in between zero and the value for a homogeneously charged plate with chargeability Y , we estimate the effective screening length to be their average, such that $\bar{\kappa}^{-1} = \kappa^{-1} / \sqrt{\cosh(0 + \Phi_H(0))/2}$. The procedure is now to use this effective screening length in the calculation of the estimated strip width s to obtain the effective chargeability \tilde{Y} . In the homogeneous limit this gives a charge density \tilde{y} for the stripes plus the side strips via Eqs. (8.15) and (8.13). The average charge density \bar{y} on the original stripe follows by assigning the charge density to a smaller surface, $\bar{y} = \tilde{y} \frac{D_1 + 2s}{D_1}$.

For the fit parameter $\alpha = 3/8$, Fig. 8.9 shows the resulting \bar{y} as a function of

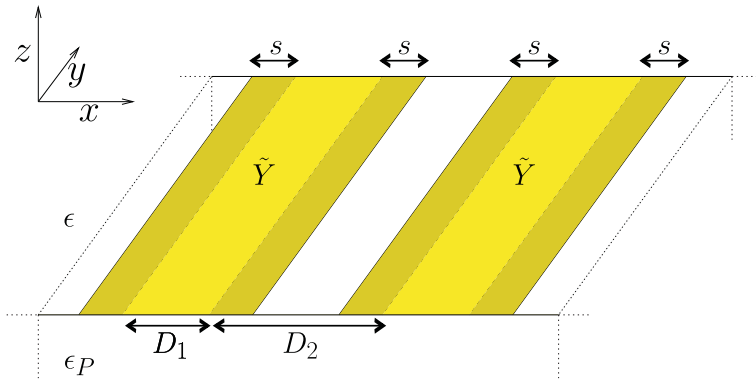


Figure 8.8: Pictorial representation of the method used to estimate the charging of narrow stripes. The darker areas adjoining the shaded stripes resemble strips of charge neutral surface assumed to be involved in the charging as well.

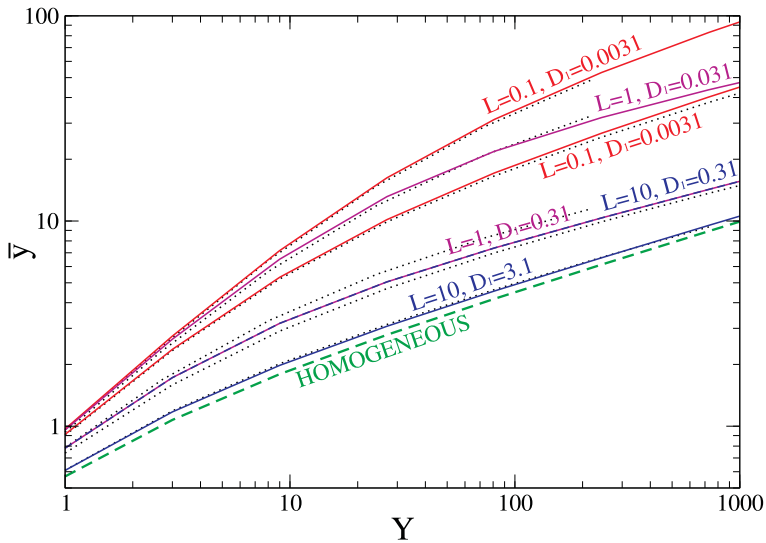


Figure 8.9: Average charge density on a chargeable stripe surrounded by charge-neutral surface, for various stripe widths D_1 and separations D_2 , plotted as a function of the stripe chargeability Y_1^+ . The medium has a dielectric constant $\epsilon_P \ll \epsilon$. The solid lines show results from the approximative method as described in the text, and the dotted lines show results from the numerical calculations. The thick dashed line shows the result for a homogeneous surface.

Y for several κL and κD_1 , together with the numerically determined ‘exact’ results based on Eq. (8.25). The agreement between the two is good, within a maximal error of 25%, and we find the right trend with Y which suggests that this approximation holds for even higher stripe chargeabilities as well. It is expected that the fits will remain good or even become better for larger stripe distances or stripe widths than investigated here, since for broader stripes the relative amount of edge surface decreases. Moreover, the choice of parameters $\kappa L = 10$ in combination with $\kappa D_1 \leq 3.6$ describes a system in which the stripes are separated by multiple screening lengths, which is close to the $\kappa D_2 \rightarrow \infty$ limit where the patches do not mutually interact anymore.

8.4 Discussion

Although the importance of charge inhomogeneities on the interactions between surfaces was already mentioned in many other studies, the relation between chemical inhomogeneity on the surface and the resulting inhomogeneity in surface charge was, to our knowledge, never studied in detail. We developed a numerical method, based on expansion into Fourier modes, to find the electrostatic potential and charge distributions close to an interface with an inhomogeneous distribution of chargeable chemical surface groups. We focussed on the case where the chemical groups are clustered in stripe-like regions, with different chargeabilities, either of the same or different sign. For the case of striped chargeable patches on an otherwise neutral surface we showed a significant increase of charging of surface groups as the width of the stripes decreases below the Debye length. For very small patches this increase of the surface charge density can easily be an order of magnitude, although patches that have little spacing show significantly less increase of charging because neighboring patches hinder each other’s charging. From the numerical results we arrive at the observation that the edges of the patches are able to charge optimally and will contribute significantly to the total charge of small patches. Our calculated numerical results for the average charge density on a patch are in fine agreement with a very basic analytical model (and one fit parameter) which employs an effective patch size in combination with results for homogeneous plates. Our results are stepping stone towards the study of interactions between heterogeneously charged surfaces, where charged patches themselves may induce charge inhomogeneities onto nearby surfaces, thereby generating nontrivial forces and torques. If the surfaces are in the vicinity of each other the induced charges cause a larger attraction between the patch and the nearby surface than constant charge models would predict. Work along these lines shows that in this way induced charges can contribute to a ‘global’ attraction at distances typically of the order of a few screening lengths, as we will see in the next chapter.

Appendix: Nonlinear PB

In this appendix we will focus on the numerical method which can be applied to efficiently solve the nonlinear PB equation (8.1) using the mode expansion (8.18) which was described in the text. We use $\sinh \Phi = (\exp[\Phi] - \exp[-\Phi]) / 2$ to write the mode expansion of the electrostatic potential as

$$\sinh \Phi(\mathbf{r}) = \frac{1}{2} \prod_{j=-M}^M E_j^+(x, z) - \frac{1}{2} \prod_{j=-M}^M E_j^-(x, z), \quad (8.26)$$

where M is the high-wavenumber cut-off and $E_j^\pm(x, z) = \exp[\pm \phi_j(z) \eta_j(x)]$ contains the nonlinear dependence of the PB equation on $\phi_j(z)$. Using the Taylor expansion of the exponential function, and applying that $\eta_j(x)^n = (\kappa L)^{(1-n)/2} \eta_{n,j}(x)$, we write $E_j^\pm(x, z)$ as a mode sum, where high-frequency modes $\eta_{n,j}$ for which $|n \cdot j| > M$ have been neglected. Note that because of this truncation we only need to expand $E_j^\pm(x, z)$ up to order M/j (and for $j = 0$ we choose to stop at order M). As an illustrative example, $E_1^\pm(x, z)$ can be expanded to a mode sum as

$$\begin{aligned} E_1^\pm(x, z) &= 1 \pm \phi_1(z) \eta_1(x) \\ &+ \frac{\phi_1(z)^2 \eta_2(x)}{2\sqrt{\kappa L}} \pm \frac{\phi_1(z)^3 \eta_3(x)}{6\kappa L} + \dots \end{aligned} \quad (8.27)$$

Using the mode-expansion representation of $E_j^\pm(x, z)$, it is now a straightforward task to calculate both the products of all $E_j^+(x, z)$ and all $E_j^-(x, z)$, as appearing in Eq. (8.26), and rewrite these products as *new* mode sums with mode amplitudes $V_k(z)$,

$$\begin{aligned} \sinh \Phi(\mathbf{r}) &= \frac{1}{2} \sum_{k=-M}^M (V_k^+(z) - V_k^-(z)) \eta_k(x) \\ &+ \mathcal{O}(\eta_{M+1}(x)). \end{aligned} \quad (8.28)$$

Note that $V_k^\pm(z) = V_k^\pm(\phi_0(z), \phi_1(z), \dots, \phi_M(z))$, such that combining Eqs. (8.28) and (8.21) yields

$$\begin{aligned} &\phi''_k(z) - \left(\frac{2\pi k}{L} \right)^2 \phi_k(z) \\ &= \frac{\kappa^2}{2} V_k^+(\{\phi_j(z)\}) - \frac{\kappa^2}{2} V_k^-(\{\phi_j(z)\}), \end{aligned} \quad (8.29)$$

for each k , $|k| \leq M$. We solve Eq. (8.29) for all k iteratively as follows. For a given mode-amplitude $\phi_k(z)$ we project out the dependence on all other modes $\phi_j(z)$, $j \neq k$,

by expanding $V_k^\pm(z) = \sum_{i=0}^M U_{k,i}^\pm(z) \phi_k^i(z)$ and write Eq. (8.29) as

$$\begin{aligned} \phi_k''(z) - \left(\frac{2\pi k}{L}\right)^2 \phi_k(z) &= \frac{\kappa^2}{2} \sum_{i=0}^M U_{k,i}^+(z) (\phi_k(z))^i \\ &\quad - \frac{\kappa^2}{2} \sum_{i=0}^M U_{k,i}^-(z) (\phi_k(z))^i, \quad z > 0. \end{aligned} \quad (8.30)$$

As an example we calculate the explicit expressions for the monopole ($k = 0$),

$$U_{0,i}^\pm = \frac{(\pm\eta_0)^i}{i!} \cdot \left(\sqrt{\kappa L} - \frac{\phi_{-1}\phi_1}{\sqrt{\kappa L}} + \frac{\phi_{-1}^2\phi_1^2}{4(\kappa L)^{3/2}} + \dots \right), \quad (8.31)$$

where we omitted higher modes $|k| > 1$ and left out the z dependence for brief notation. If we insert this expressions into Eq. (8.30) again, we find

$$\phi_0''\eta_0 = \kappa^2 \left(1 - \frac{\phi_{-1}\phi_1}{\kappa L} + \frac{\phi_{-1}^2\phi_1^2}{4(\kappa L)^2} + \dots \right) \sinh[\phi_0\eta_0], \quad (8.32)$$

which reduces to the planar PB-equation in the case that $\phi_{\pm 1}$ vanish. Eq. (8.30) together with the BC's (8.19) and (8.20) can be used to find the numerical solution to every mode, given the approximations to the solutions for other modes. In order to obtain the solution of the full problem, we therefore apply an iterative scheme in which we go through multiple cycles of solving each PB mode equation consecutively, until we find the converged solution. This is done by solving for every $\phi_k(z)$ the mode equations (8.30) on a 1-dimensional grid. As a starting point we use a vanishing solution for all modes. It is possible to reduce the computational effort significantly by considering systems for which $\Phi(x, z) = \Phi(-x, z)$, such that all $\phi_k(z)$ take values in the real space \mathbb{R} and $\phi_k(z) = \phi_{-k}(z)$. The number of iterations required for convergence depends on the degree of nonlinearity in the system and is typically in the order of 10 per mode.

Chapter 9

Effective attraction between similar patchy surfaces

Abstract

Poisson-Boltzmann theory in combination with charge regulation is applied to calculate the interaction between chargeable patchy surfaces. Within a parallel-plate geometry we model patches to charge positively whilst the surrounding surface charges negatively (or vice versa). Interactions between the patch and the opposing surface turns out to depend nontrivially on the distance between the plates; the local (negative) charge density on the opposing surface is strongly dependent on the distance to a patch. We observe that an effective repulsive force between the surfaces at large separations can easily become attractive at smaller separations due to this charge-regulation mechanism. We therefore distinguish three characteristic regimes for the electrostatic interaction between patchy surfaces: attraction at any distance, repulsion at any distance, and a repulsion|attraction cross-over. The energy barrier between attraction and repulsion in the interaction potential can be tuned by varying the patch size, even while keeping the patch coverage fraction constant. We argue that randomly distributed patchiness in combination with charge regulation gives rise to a strong tendency for sub-Debye length attractions between similar colloidal particles.

9.1 Introduction

Colloidal particles tend to charge in contact with an electrolyte due to an exchange of ions with the solvent. Because of their charge, such particles experience an electrostatic interaction with the ions, and also with other colloidal particles. A well-known result that follows from DLVO-theory [16, 17] is that this interaction can only be of significant strength up to distances comparable to the Debye screening length, which is the typical thickness of the layer of counterions in the vicinity to the charged surface. As one might expect, the interaction between equal homogeneously charged particles is typically repulsive, if Van der Waals attractions at very small distances are ignored. However, for a large class of colloidal particles the charge

is distributed *inhomogeneously* over the surface. Despite that in such cases the net charge can be estimated by means of e.g. electrophoresis or streaming potential measurements [129], the nature and strength of the two-particle interactions may differ enormously from what one would expect for homogeneously charged particles with the same net charge. For example Janus particles [125, 126] with one positively and one negatively charged hemisphere can be uncharged on average, while experiencing strong dipolar forces due to the inhomogeneous nature of the charge distribution. In such cases repulsiveness is not guaranteed anymore and strong attractions may be found. Charge inhomogeneities may be due to a naturally occurring inhomogeneous distribution of chargeable groups over the surface such as for example in clays or bitumen [194, 195], or certain latex or silica particles [173, 196]. The inhomogeneities can also be the result of the adsorbance of oppositely charged polyions on the surface [174, 197, 198]. Nowadays it is even possible to design the structure of the inhomogeneities on the particles [108]. In many cases, however, charge inhomogeneities are not a severe point of attention in models that describe the electrostatic interactions between colloids as often the net charge dominates the electrostatic interaction between the particles, such that a ‘monopole’-treatment suffices. This is especially the case at colloid-colloid distances much larger than the typical size of the inhomogeneities. Most experimental measurements of the force between colloidal particles can therefore be described with variations of the classical DLVO-theory [16, 17, 130], in which one either assumes a constant and homogeneous surface charge (CC) [199] or a constant surface potential (CP) on the colloidal surface as the distance between the particles is varied [200–202]. More detailed approaches exist that account for the fact that charge is regulated; it follows from chemical equilibria between the surface and the solvent [73]. The constant regulation (CR) model [178, 182] includes regulation by interpolating between the CC and the CP model using an additional fit parameter which signifies the constantness of the surface charge as a function of the surface potential. This model can be used to fit experimental data where CC and CP models fails [157, 203]. Recently, Popa *et al.* used the CR model to fit force curves between latex particles with adsorbed polyelectrolytes [175, 204]. However, AFM microscopic images of these particles showed that the adsorbed polyelectrolyte had not formed a smooth layer on the surface. Instead it was adsorbed in the form of small patches of opposite charge. As was shown by Popa *et al.*, this patchiness induced an additional attraction between the particles at distances that are of the order of the size of the patches. Although the CR model did well in describing the interparticle force at large and intermediate distances, at close distances it failed to reproduce the observed additional attraction. Theoretical studies show that attractive forces may indeed arise between inhomogeneously charged surfaces [174, 186, 205–207], even if the net charge of the surfaces has the same sign [208–210]. If the inhomogeneities are free to migrate over the surface, the effective electrostatic interaction has an even greater tendency to become attractive as positive patches prefer to align opposite to negative patches on the opposing surface. This is a straightforward result of statistical averaging [174].

In this chapter an approach based on charge regulation and Poisson–Boltzmann theory will be put forward. We investigate if and how pairs of chargeable patchy surfaces are able to induce an effective electrostatic attraction at distances of the order of the electrostatic correlation distance and smaller. The latter distance is the well-known Debye screening length, defined by $\kappa^{-1} = (8\pi\lambda_B\rho_s)^{-1/2}$, with $\lambda_B \equiv e^2/\epsilon k_B T$ the Bjerrum length which depends on the dielectric constant ϵ , and the bulk concentration of ions $2\rho_s$ far away from the charged surfaces. Here k_B is the Boltzmann constant, T is the temperature of the solvent, and e the elementary charge. Although the model that is presented here considers the interaction between flat plates, it has interesting applications to the study of interactions of charged patchy colloidal particles, as it can describe aspects of the underlying physics of the interactions at small distances. At larger distances the finite size and curvature of the particles become relevant [121, 127, 211–213]. In Fig. 9.1(a) a typical configuration of two patchy particles at small distances is sketched. We map the problem of calculating the force ‘in the rectangular area’ to that of two plates separated by a distance h , as is shown in Fig. 9.1(b). The width of the total interaction area is denoted by L , although for a surface with multiple interacting patches, the parameter L characterises the typical center-to-center distance between the patches, while a parameter θ must be introduced to specify the surface coverage fraction of patches, such that in our model geometry the width of the patches follows as $D = \theta L$. One expects a patch mainly to interact with non-patchy parts of the surface of other particles for low θ . For this reason, and for simplicity and clarity, we consider here a homogeneously chargeable top plate. Note however that the induced charge on the top plate will *not* be homogeneous as the charge density is regulated locally. Intrinsic patchiness on *both* plates could be interesting in the case that lateral forces between both surfaces are studied, and will also be discussed later in the text briefly.

9.2 Theory

The charge regulation on the bulk surface and the patches can be described by means of an equilibrium constant K^\pm that relates the surface charge density due to a release of cations (+) and anions (-) into the solvent to the local ion- and surface group densities by

$$K^\pm = \frac{\rho_\pm \sigma^\pm}{m_\pm - \sigma^\pm}, \quad (9.1)$$

with m_\pm the density of chargeable groups on the surface, σ^\pm the positive/negative surface charge density, and $\rho_\pm = \rho_s \exp(\pm\Phi)$ the density of counter-ions close to the surface that follows from the Boltzmann distribution of ions. For convenience we defined $\Phi = \Psi/\Psi_{\text{TH}}$ as the dimensionless potential which is related to the electrostatic potential Ψ through the thermal voltage $\Psi_{\text{TH}} = k_B T/e = 25.6$ mV at room temperature. In case of an excess of chargeable surface sites w.r.t. the charge density ($\sigma_\pm \ll m_\pm$), the relation between the charge density $\pm e\sigma^\pm$ and the surface potential

becomes

$$4\pi\lambda_B\sigma^\pm/\kappa \equiv y^\pm = Y^\pm \exp(\mp\Phi), \quad (9.2)$$

with $y^\pm = 4\pi\sigma\lambda_B$ the dimensionless positive or negative charge density and λ_B the Bjerrum length. The parameters Y^\pm we will call positive/negative chargeability, as they were introduced in Ref. [213] or Chapter 8. The chargeabilities Y^\pm are local surface parameters which are defined by

$$Y^\pm = \kappa \frac{m^\pm K^\pm}{\rho_s^2}, \quad (9.3)$$

where m_\pm is the density of chargeable groups and ρ_s the bulk density of counterions. In the model that we will consider, the bottom plate contains a patch, a stripe of width D , which is able to charge only positively with constant chargeability Y^+ . The bulk surface of the bottom plate, as well as the entire top plate, is negatively chargeable with chargeability Y^- as indicated in Fig. 9.1. At the bottom plate, the positive and negative chargeability can be written as step functions $Y^\pm(x)$ that only take nonzero values at the patch and bulk surface, respectively.

To find the electrostatic potential throughout this system we use the nonlinear Poisson-Boltzmann (PB) equation,

$$\nabla^2\Phi(\mathbf{r}) = \begin{cases} \kappa^2 \sinh \Phi(\mathbf{r}) & 0 \leq z \leq h; \\ 0 & \text{otherwise,} \end{cases} \quad (9.4)$$

with z the normal direction between the plates. We start by formulating continuity of the potential at the planar surfaces and global neutrality,

$$\lim_{z \uparrow 0} \Phi(x, y, 0^-) = \lim_{z \downarrow 0} \Phi(x, y, 0^+); \quad (9.5)$$

$$\lim_{z \uparrow 0} \Phi(x, y, h^-) = \lim_{z \downarrow 0} \Phi(x, y, h^+); \quad (9.6)$$

$$\lim_{z \rightarrow \pm\infty} \Phi'(x, y, z) = 0, \quad (9.7)$$

where a prime denotes the derivative w.r.t. z . For colloidal plates with dielectric constant ϵ_P , the boundary condition on the electric field on the bottom plate, at $z = 0$, becomes

$$\begin{aligned} \lim_{z \downarrow 0} \Phi'(x, z) &= \lim_{z \uparrow 0} \frac{\epsilon_P}{\epsilon} \Phi'(x, z) + \kappa Y^-(x) \exp(+\Phi(x, 0)) \\ &\quad - \kappa Y^+(x) \exp(-\Phi(x, 0)). \end{aligned} \quad (9.8)$$

On the top plate, at $z = h$, we have

$$\begin{aligned} \Phi'(x, h^-) &= -\frac{\epsilon_P}{\epsilon} \Phi'(x, h^+) \\ &\quad - \kappa Y^- \exp(+\Phi(x, h)). \end{aligned} \quad (9.9)$$

Note that in Eqs. (9.4)–(9.9) we assumed the plates to be infinitely thick.

9.3 Method

By applying a numerical scheme to solve the full nonlinear Poisson-Boltzmann (PB) equation by means of a Fourier expansion, that was developed in Ref. [213] or Chapter 8, it can now be calculated how a patch on a surface interacts with an intrinsic homogeneous opposing surface. We choose $N = 1000$ grid points in the normal (z -) direction interval $z \in (0, h)$, and a Fourier expansion in the lateral x direction up to mode 64, which were tested to be sufficient to avoid numerical artifacts. For explicit calculations, we choose $Y^- = Y^+ = 31.6$, $L = 1\kappa^{-1}$, and $\theta = 0.2$, such that $D = 0.2\kappa^{-1}$, and various distances h . For simplicity and clarity, the dielectric constants of the solvent and the plates are chosen such that $\epsilon_p/\epsilon = 1$, to eliminate additional electrostatic forces due to image charges.

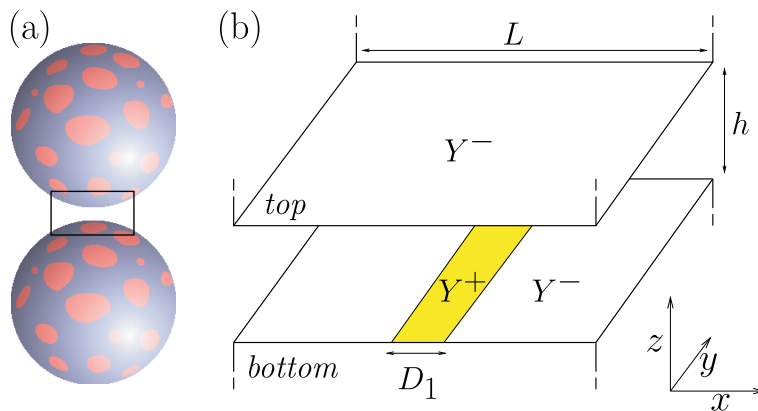


Figure 9.1: Pictorial representation of (a) two patchy particles at close distances (b) the two-plate system consisting of a top plate with homogeneous chargeability and a bottom plate with patch, that is shaded here for better visibility.

9.4 Results

Fig. 9.2 shows the result of the numerical calculation of the surface potentials $\Phi(x, 0)$ and $\Phi(x, h)$ in (a) and charge density $y(x)$ in (b) at the two plates at various separations. The charge and potential profiles that are found for large separations ($\kappa h = 0.8$) agree with calculations for single (patched) plates [213], showing a typical excess of charge at the edges of the patches. For smaller distances, the charge-density profile on the top and the bottom plate change as a consequence of the converging potential profiles of both plates. Note that in particular the potential profile of the top plate is sensitive to the distance h , as its value right above the middle of the patch, $\Phi(L/2, h)$, changes from -2.4 to -1.5 if h is reduced from

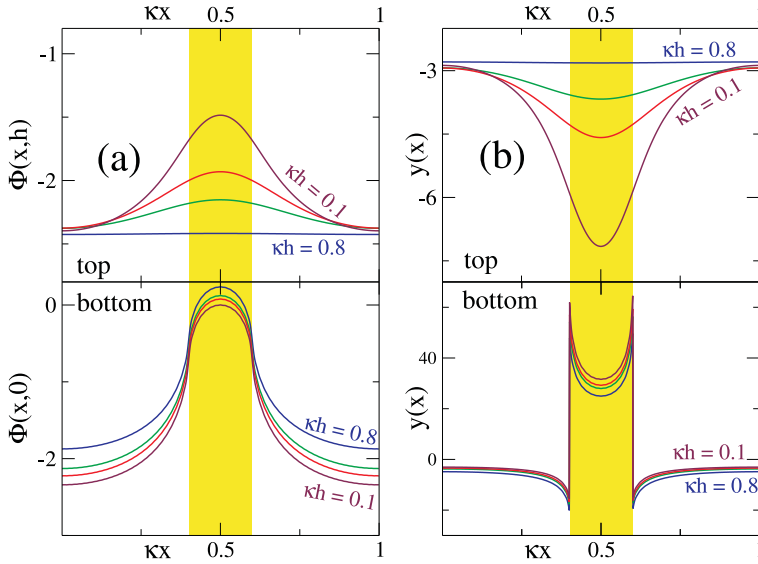


Figure 9.2: Positional dependence of the surface potential (a) and dimensionless surface charge (b) on the top and bottom plate using $\kappa L = 1$, $D = 0.2L$, and $Y^- = Y^+ = 31.6$. The different lines show various separation distances, $\kappa h \in \{0.8, 0.3, 0.2, 0.1\}$. The shaded areas show the position of the stripe on the bottom plate.

$\kappa h = 0.8$ to $\kappa h = 0.1$. This has an important effect on the related charge density, as can be seen in Fig. 9.2b, which more than doubles (from -3 to -7) while the stripe on the bottom plate remains strongly positively charged at $y \sim 30 - 50$. The induced charge on the top plate generates a strong additional attraction between the stripe and the opposing plate, which is able to overcome the repulsion between the similar negative charge densities away from the patch if the distance becomes small, as we will see now.

The stress tensor in the electrolyte can be used to calculate the disjoining pressure between the inhomogeneously charged plates at a given separation h . Its cartesian components are given by

$$T_{ij}(x, z; h) = \frac{\epsilon}{4\pi} \left(E_i(x, z)E_j(x, z) - \frac{1}{2}E^2(x, z)\delta_{ij} \right) - 2\rho_s k_B T (\cosh \Phi(x, z) - 1) \delta_{ij}, \quad (9.10)$$

where the first term represents the electrostatic (Maxwell) stress in terms of the electric field $\mathbf{E} = -\Psi_{\text{TH}} \nabla \Phi$, and the second term represents the osmotic pressure contribution. By symmetry, the total force per unit area (the ‘disjoining’ pressure) between the plates can only have a nonzero component in the z -direction, and

therefore follows from laterally averaging the zz -component of the stress tensor as

$$p(h) = -\frac{1}{L} \int_{x=0}^L T_{zz}(x, z_F; h) dx, \quad (9.11)$$

where $z = z_F$ specifies the plane of integration which can be chosen anywhere in between the plates, $0 < z_F < h$, without determining the obtained values for the force. For the selected set of parameters of Fig. 9.2 we find attraction ($p < 0$) for $h < 0.5\kappa^{-1}$, and repulsion ($p > 0$) at larger separations.

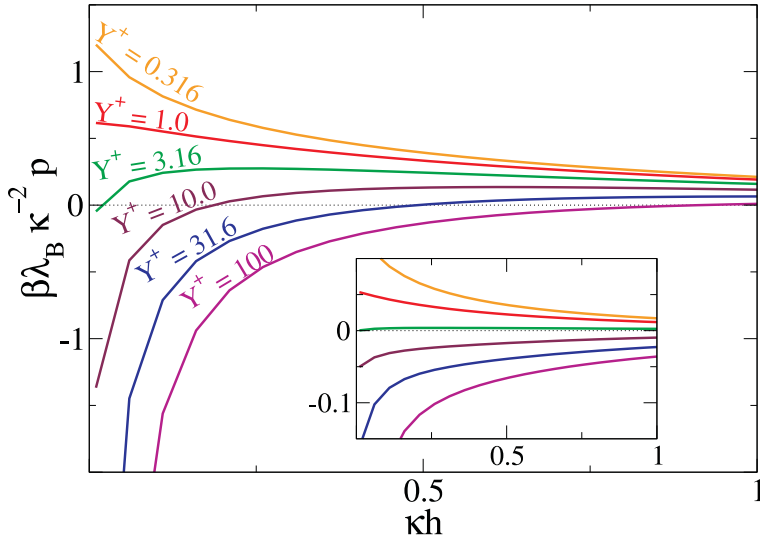


Figure 9.3: Pressure-distance curves between a homogeneously chargeable and a patched plate as in Fig. 9.1 for various Y^+ showing repulsion ($p > 0$) for small Y^+ , attraction for large Y^+ , and crossover behaviour at intermediate Y^+ . The parameters here are $\kappa L = 1$, $\theta = 0.2$ and $Y^- = 31.6$. The inset shows the same calculations for a weaker plate chargeability $Y^- = 1$.

For $Y^- = 31.6$ and several patch chargeabilities Y^+ we calculate the resulting disjoining pressure and the effective potential by performing the integral of Eq. (9.11) numerically. The result is plotted as a function of the plate separation h in Fig. 9.3. From the force-distance curves three regimes can be identified. In the first ‘weak stripe charge’ regime (R) one finds a repulsive force at all distances, as we see in Fig. 9.3 for $Y^+ \leq 1.0$. In this regime the positive charge on the patch and the induced negative charge on the top plate are too small to overcome the repulsion of the like-charged background charges on the surfaces. For larger patch chargeabilities we find a second regime (R+A) where long-range repulsions cross-over to short-range attractions, with a crossover distance that increases monotonically with Y^+ . For the

present geometrical parameters short-range attractions are found for $Y^+ \geq 3.16$. A third regime (A) appears for sufficiently large Y^+ , where the interaction is attractive at all distances. This regime does not occur for the parameters chosen in the main graph of Fig. 9.3, where the plate-plate attraction disappears at large separations for all Y^+ , but it can be observed in the inset of Fig. 9.3, which contains data for a weaker chargeable ‘bulk’ $Y^- = 1$, while keeping the same range in Y^+ . From this inset it also becomes clear that it is difficult to observe the interesting intermediate regime for low values of the ‘bulk’ chargeability Y^- , as one can only observe a very small band in the range of the patch chargeability Y^+ for which a crossover from long-range repulsion to shorter-ranged attraction takes place. We will demonstrate below that this holds in general, implying that this cross-over regime is only ‘visible’ in the nonlinear regime of the PB equation.

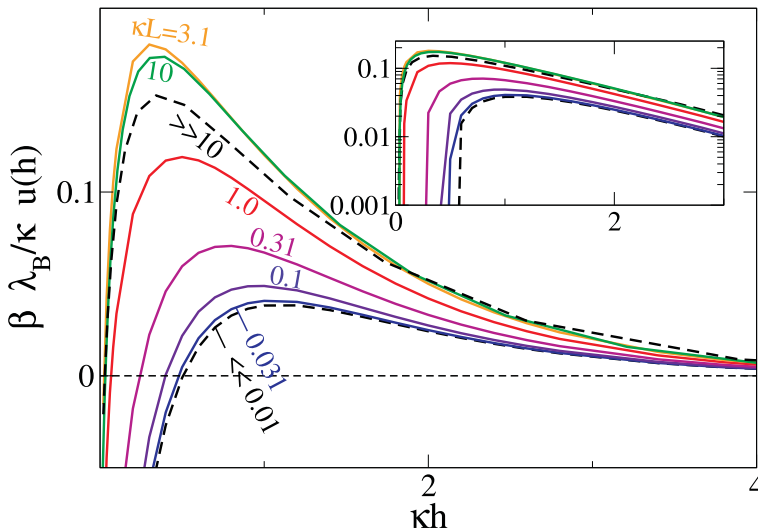


Figure 9.4: Effective interaction potential per unit surface between a homogeneously chargeable and patched plate as a function of the separation in units of screening lengths, κh , for several lengths κL . The parameters here are $\theta = 0.2$ and $Y^+ = Y^- = 31.6$. The inset shows the same data in a logarithmic plot to show exponential decrease.

From integrating the pressure–distance curves as in Fig. 9.3 one obtains the effective interaction potential per unit surface area,

$$u(h) = \int_h^\infty dh p(h). \quad (9.12)$$

Regarding the parameter range of Fig. 9.3 the corresponding interaction potential can be expected to be significant (of order $k_B T$) for the case that the total interaction area is of the order L^2 and $\lambda_B < \kappa^{-1}$; for spherical surfaces the size of the

interacting area can be estimated by the Derjaguin approximation [214]. Fig. 9.4 shows $u(h)$ for a patch coverage fraction $\theta = 0.2$, and for various κL while keeping $Y^+ = Y^- = 31.6$ fixed. The strong dependence on κL shows non-additivity of the forces resulting from the patches [215]. Fig. 9.4(b) shows exponentially decaying repulsions at larger distances, with decay length κ^{-1} . This is the same behaviour as one finds for homogeneously charged plates at large distances [129]. In this regime the repulsion can be described by linear PB theory, using effective charge densities matched to describe the far field potential of both single plates [18, 20, 213]. The energy barrier separates attraction at small distances and repulsion at larger distances. Both the inset and the main figure include the interaction potential in the extreme cases $\kappa L \gg 1$ and $\kappa L \ll 1$, denoted by dashed lines. Note that the height of the energy barrier is a nonmonotonic function of κL ; infinite κL does not limit the energy barrier from above, as the line for $\kappa L = 3.1$ clearly gives a higher barrier than for $\kappa L = 10$. As one can see from the curves for $\kappa L = 10$, the potential barrier decreased again, and is approaching the infinite- κL limit. Fig. 9.4 therefore shows that, for this set of parameters, patches with a size of the order of a screening length give the largest energy barrier between the repulsive and the attractive part of the pair potential. This may be useful to tune stability of a suspension

For each κL and patch coverage θ , there exist different regimes of Y^+ and Y^- for which repulsion (R), repulsion and attraction (R+A), and attractions (A) is found between the plates of Fig. 9.1. Fig. 9.5 maps these regimes for several κL and $\theta = 0.2$ and $\theta = 0.1$. The lower and the upper line bundles in Fig. 9.5 correspond to the R to R+A and the R+A to A crossover, respectively. The intermediate R+A regime at intermediate values for Y^+ , characterised by a long-range repulsion combined with a short-range attraction, opens up for higher background chargeabilities Y^- . This is in agreement with the observations made in Fig. 9.4. Varying the dimensionless patch distance κL does not significantly change the size of the interval, as Fig. 9.5 shows. However, all regimes shift down to lower Y^+ for decreasing κL , which therefore confirms that smaller patches (while keeping the coverage θ constant) give rise to more attractive forces.

As we stressed before, the critical patch coverage fraction θ_{crit} , which is the patch coverage fraction at which the disjoining pressure vanishes, depends on the distance between the plates h . Fig. 9.6 shows θ_{crit} as a function of the length scale κL , in (a) and (b) for large and small distances respectively, and for various sets of chargeabilities Y^+ and Y^- . At large distances $h \gg L$, the nature of the force (attractive/repulsive) is an immediate consequence of the average (renormalised) charge density on the inhomogeneous plate, since the inhomogeneities in the potential only propagate over a distance which is smaller than the separation between the plates. The difference in the vertical order of the lines in Fig. 9.6 (a) and (b) is the best observation of the fact that the behaviour of the system at small and large separations depends totally different on Y^+ and Y^- . We note that at large distances, the critical coverage θ_{crit} depends on the *relative* strength of the chargeability of the patch with respect to the chargeability of the surrounding plate, i.e. in (a) the lines

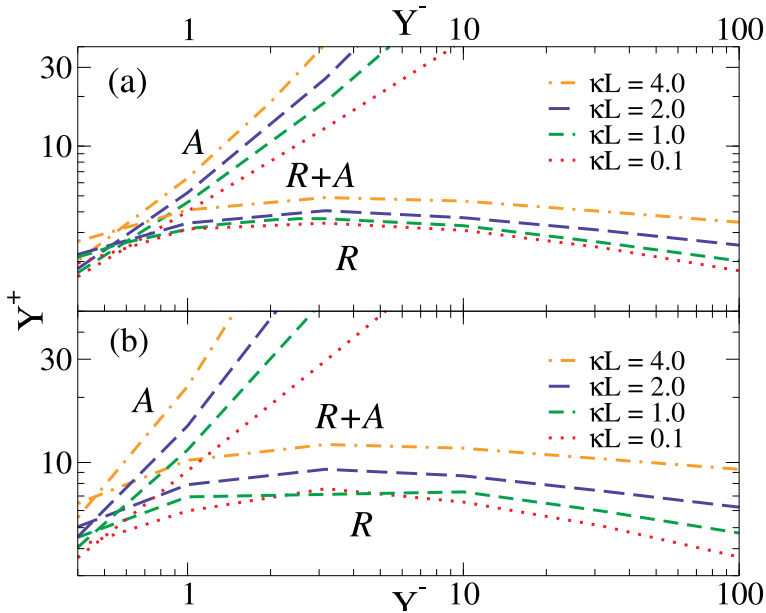


Figure 9.5: Crossover values for the patch chargeability Y^+ as a function of the surrounding plate chargeability Y^- for several length scales κL , outlining regions of pure attraction (A), long range repulsion combined with short range attraction (R+A), and pure repulsion (R). (a) and (b) hold data for patch coverage $\theta = 0.2$ and $\theta = 0.1$ respectively.

are ordered by the value of Y^+/Y^- . However, at small distances, θ_{crit} is mainly determined by the chargeability of the patch alone, i.e. Y^+ (and not Y^-) is the parameter of significant importance for the behaviour here.

9.5 Random patchiness

So far, we have investigated the interaction between a patch-containing plate and a homogeneously chargeable plate. However, for most colloidal suspensions all particles are alike; both surfaces contain patches. We argued that the attraction mechanism that we described here will also apply for the interaction between a patch-containing plate with another patch-containing plate, certainly in the case that θ is small. In the following we will calculate the interaction between surfaces which both contain exactly one patch, although in general the interactions between two surfaces with many (randomly distributed) patches must be considered such that some patches will face a patch on the opposing surface, whilst others will face no patch but only the oppositely chargeable surface. We will calculate the disjoining

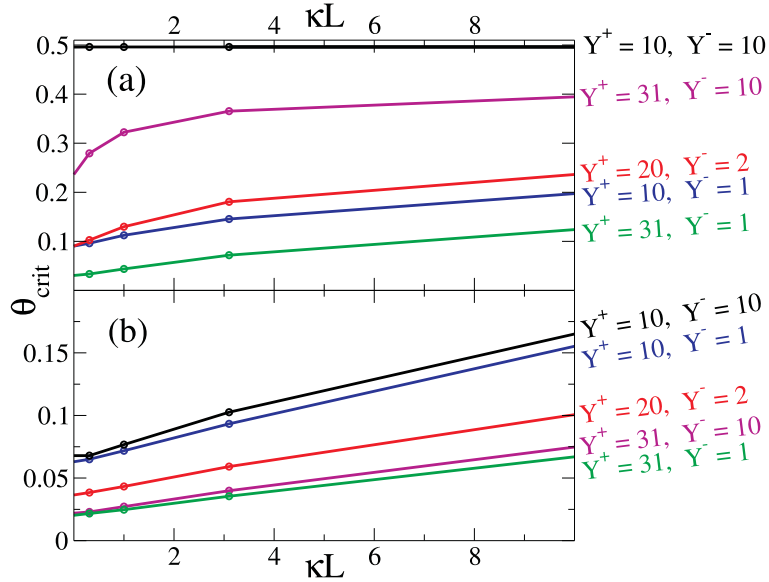


Figure 9.6: Critical patch coverage fraction θ_{crit} at which the disjoining pressure between the plates changes sign, as a function of the length κL for several patch and plate chargeabilities Y^+ and Y^- , in (a) for large distances ($\kappa h = 5$), whilst in (b) for $\kappa h = 0$.

pressure for the case that two patches are exactly aligned, as well as for the case that the two patches are shifted by a distance $L/2$, as is shown in the insets of Fig. 9.7. As a crude estimate for the disjoining pressure between two patched plates we then assume that the effective disjoining pressure is given by the unweighed average of the pressures resulting from either case. A more proper method would be to consider all displacements between 0 and $L/2$ and average over these. Such a procedure was carried out in Ref. [186], where the authors considered patches that were formed out of condensed polymer, being able to displace over the surface such that a Boltzmann average over the configurations of the patches on the surface was needed. Here however, we assume the patches to be pinpointed to the surface. For the sake of simplicity we only consider the aligned and the shifted case and average over these to illustrate that a randomly distributed but static patchiness is able to generate a sub-Debye length attraction between surfaces for $\kappa L = 5$. Fig. 9.7 shows p for plate chargeability $Y^- = 31.2$ and various patch chargeability Y^+ . The (red) dashed lines in Fig. 9.7, which correspond to the aligned geometry, show that the effective force between the surfaces in this case is always repulsive. This is because the patches are not able to induce an attraction with the opposing surface, as the patches on both plates exactly face each other. On the other hand, the (blue) dotted lines in Fig. 9.7 correspond to the shifted geometry and show a repulsion to attraction cross-over for sufficiently high patch chargeabilities. Our observations

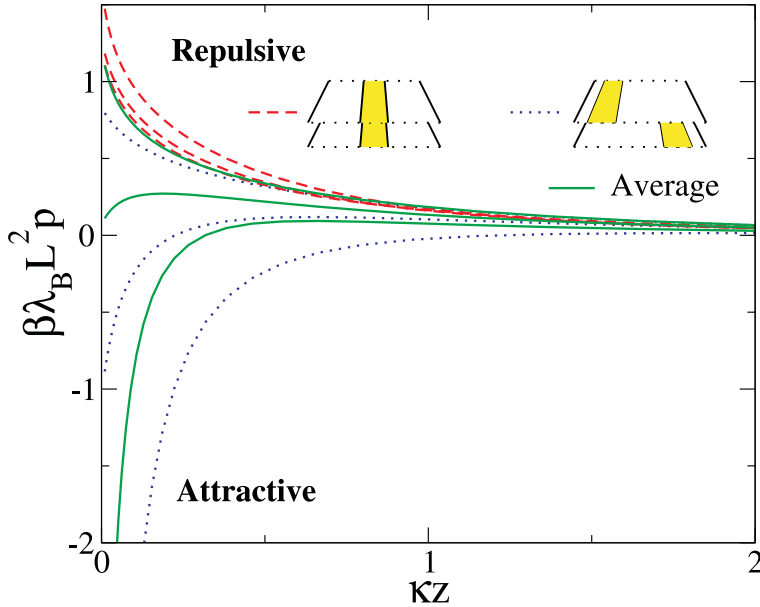


Figure 9.7: Pressure–distance curves for two patched plates for the two different alignments shown in the insets. The parameters here are $\kappa L = 5$, $\theta = 0.2$ and $Y^- = 31.6$. We plot data for several patch chargeabilities; $Y^+ \in \{0.1, 1.0, 10.\}$.

are in agreement with earlier observations for a single patch interacting with a homogeneously chargeable plate. The latter is expected as there is almost no direct interaction between patches in the case of the maximally nonaligned patches. By taking the average of the pressures that arise in both relative alignments that one gets a rough idea of the disjoining pressure between two large randomly patched surfaces. We again observe that the attractive pressure can become dominant over the repulsive pressure at sufficiently small distances such that the effective pressure becomes attractive. It can be checked that this attraction vanishes for really small patches, $\kappa L \rightarrow 0$.

9.6 Discussion

We studied a negatively chargeable surface with positively chargeable patches facing a homogeneous surface and calculated the resulting charge on both surfaces at varying distances. Observed was that the presence of the patches induces significant inhomogeneous charging on the non-patchy surface at small distances. The reason is that the surface area opposite to the patch gains additional positive charge in the vicinity of the negatively charged patch. The resulting force between pairs

of such plates can therefore become attractive at short separations, whilst at large separations we find an effective repulsion, that decays exponentially with distance as expected. If we assume that this interaction mechanism also describes the case of spherical patchy particles, the associated potential barrier between repulsion and attraction determines the stability of the system against coalescence. We showed that the height of the barrier can be tuned by varying the size of the inhomogeneities while keeping the patch coverage ratio constant. For the parameters used, maximal stability occurs for patches with sizes of the order of a few screening lengths. These calculations also form a stepping stone towards more elaborate/realistic ones, in which patch-patch interactions and hence lateral forces and torques emerge. This extension is, however, left for future work.

Conclusions and Outlook

Throughout this thesis we studied charged surfaces in electrolytes by means of Poisson-Boltzmann theory, which describes ion-density profiles around these surfaces and predicts the formation of a 'double layer' of countercharge that screens surface charge. As a result, the strength of electrostatic interactions reduces exponentially over a typical distance that is determined by the polarisability of the solvent and the bulk ion concentration. This distance is known as the Debye screening length. In water this length is typically between a nanometer and a micron. In other solvents, this distance can even be larger than a micron. The screening length sets the electrostatic capacity of surfaces in electrolyte; it turns out to be inversely proportional to it. Therefore, conducting surfaces that are immersed in electrolyte can be applied as capacitors with a capacitance that can be tuned by changing the ion concentration. In Chapter 3 we showed that this property can be applied to reversibly gain energy out of mixing streams of different salinity.

The remainder of the thesis concerned colloidal particles, which are typically charged due to ion dissociation/association processes at the colloid-fluid interface, or by ion absorption into a porous structure as we discussed in Chapter 4. Since colloidal particles live on a length scale that is often of the same order of magnitude as the Debye screening length, their electrostatic charge often determines phase behaviour of the whole suspension. For example, crystallisation at very low packing fractions can occur if the colloids have high charges. In this thesis we extended the classical theories that describe the interaction between colloidal particles towards situations that became relevant only recently; a large class of new colloidal particles, so-called 'patchy' particles with an inhomogeneous surface distribution of chargeable groups, demands orientational-dependent pair interactions. This applies to short-range forces, like hydrophobic attractions, but also to longer-ranged electrostatic forces. In especially, we considered the electrostatic interaction between suspensions of spherical 'Janus' particles with differently charged hemispheres. We found in Chapter 5 that a mode expansion of the electrostatic potential and the ion-density profiles can be useful in order to describe the interaction between inhomogeneously charged particles in general. The latter also gave a handle for a

mode-by-mode comparison of PB with Monte Carlo data for the charge-density profiles in the ionic double layer around Janus particles. The regime where PB theory holds was observed to be in agreement with what was known for monopoles. Therefore, it is possible to express the electrostatic interaction between Janus particles in the form of a DLVO-like monopole-monopole term, however now extended by a monopole-dipole and a dipole-dipole term. The higher-mode interactions we did not derive explicitly in this thesis. The mode expansion of the problem was also used to calculate deviations from the Debye-Hückel approximation close to strongly charged Janus particles. These deviations occur in the nonlinear regime of the Poisson-Boltzmann equation where the surface potential is high. In Chapter 6 we derived the renormalised multipoles of the charge densities for strongly charged Janus particles. These can be used to correct the Debye-Hückel approximation in order to give more accurate results regarding the particle-particle interactions. We observed couplings between the monopole, dipole, and higher-order modes.

Apart from inhomogeneities, the surface chemistry that induces the charge on the particles can also be crucial for observed interactions between particles. Although it is tempting to assume that equal particles have equal charges, this turns out not to be the case in general. Charge dynamically results from a chemical equilibrium between the colloidal surface and the ions in the liquid; it is regulated. As a result, the charge on a colloid changes unceasingly because of (indirect) interactions with other particles. In Chapter 7 we considered the effect of charge regulation on the phase behaviour of colloidal suspensions, and compared this with the approximation that the electrostatic potential (instead of the charge) at the surface is fixed at any configuration and packing fraction. For both charge-regulated and constant-potential surfaces we found a much larger parameter-regime where crystalline structures exist.

Charge regulation turns out to be important as well for particles that have (many) small patches with a different chemical structure than the bulk surface. These patches are for example able to charge positively whilst the bulk surface of the particles charge negatively. In Chapter 8 we took a closer look at these patchy surfaces. We calculated that the interaction between small patches and the bulk surface induces a strong charge density on the patches. In Chapter 9 we showed that chemical inhomogeneities on one colloid can induce charge inhomogeneities as well on another colloid. This may lead to a net attraction at small distances whilst the colloids could repel each other at larger distances.

As the work on charge-regulating patchy surfaces was performed within planar geometry, future work could involve finding descriptions of the multipolar interactions between charge-regulating colloids. It could for example be investigated how the charge multipoles of Janus particles are affected by charge regulation or how charge regulation can induce Yukawa dipoles on pairs of otherwise homogeneously charged colloids. Also particles with different geometries than spherical have not been considered in this thesis; the Yukawa-multipole framework derived in Chapter 5

would however also allow for a multipole description of the electrostatic interactions between particles with different geometric properties than spherical, for example colloidal ellipsoids or even cubes.

References

- [1] R. Brown. *Phil. Mag.* **4**, 181 (1828).
- [2] A. Einstein. *Ann. Phys.* **17**, 549 (1905).
- [3] W. Sutherland. *Phil. Mag.* **9**, 781 (1905).
- [4] D. F. Evans and H. Wennerström. *The Colloidal Domain*. Wiley-VCH, New York (1994).
- [5] L. Onsager. *Chem. Rev.* **13**, 73 (1933).
- [6] C. Kittel. *Thermal Physics (2nd ed.)*. W. H. Freeman and Company, San Francisco and London (1980).
- [7] D. Brogioli. *Phys. Rev. Lett.* **103**, 058501 (2009).
- [8] J. D. van der Waals. *Over de Continuïteit van den Gas- en Vloeistofoestand*, *Ph.D. Thesis*. Leiden University (1873).
- [9] J. Israelachvili. *Intermolecular and surface forces*, volume 2nd edition. Academic Press, Amsterdam (1991).
- [10] D. J. Griffiths. *Introduction to electrodynamics, third edition*. Prentice Hall, London (1999).
- [11] R. Evans. *Adv. Phys.* **28**, 143 (1979).
- [12] P. Attard. *J. Phys. Chem.* **99**, 14174 (1995).
- [13] J. Groenewold and W. K. Kegel. *J. Phys. Chem B* **105**, 11702 (2001).
- [14] E. Trizac, L. Bocquet and M. Aubouy. *Phys. Rev. Lett.* **89**, 248301 (2002).
- [15] E. Trizac, L. Bocquet, M. Aubouy and H. H. von Grünberg. *Langmuir* **19**, 4027 (2003).
- [16] B. Derjaguin and L. Landau. *Acta Physicochim. URSS* **14**, 633 (1941).
- [17] E. J. W. Verwey and J. T. G. Overbeek. *Theory of the Stability of Lyophobic Colloids*. Elsevier, New York (1948).
- [18] S. Alexander, P. M. Chaikin, P. Grant, G. J. Morales, P. Pincus and D. Hone. *J. Chem. Phys.* **80**, 5776 (1984).
- [19] A. Diehl, M. C. Barbosa and Y. Levin. *Europhys. Lett.* **53**, 86 (2001).
- [20] E. Trizac, L. Bocquet and M. Aubouy. *Phys. Rev. Lett.* **89**, 248301 (2002).
- [21] B. Zoetekouw and R. van Roij. *Phys. Rev. Lett.* **97**, 258302 (2006).
- [22] R. E. Pattle. *Nature* **174**, 660 (1954).
- [23] G. L. Wick and W. R. Schmitt. *Mar. Technol. Soc. J.* **11**, 16 (1977).
- [24] O. Levenspiel and N. de Nevers. *Science* **183**, 157 (1974).
- [25] S. Loeb. *J. Membr. Sci.* **1**, 49 (1976).
- [26] S. Loeb, F. Van Hessen and D. Shahaf. *J. Membr. Sci.* **1**, 249 (1976).
- [27] T. Thorsen and T. Holt. *J. Membr. Sci.* **335**, 103 (2009).
- [28] J. W. Post, J. Veerman, H. V. M. Hamelers, G. J. W. Euverink, S. J. Metz, K. Nijmeijer and C. J. N. Buisman. *J. Membr. Sci.* **288**, 218 (2007).
- [29] J. N. Weinstein and F. B. Leitz. *Science* **191**, 557 (1976).
- [30] J. Veerman, M. Saakes, S. J. Metz and G. J. Harmsen. *J. Membr. Sci.* **327**, 136 (2009).
- [31] J. W. Post, H. V. M. Hamelers and C. J. N. Buisman. *Environ. Sci. Technol.* **42**, 5785 (2008).

- [32] P. Dlugolecki, K. Nymeijer, S. J. Metz and M. Wessling. *J. Membr. Sci.* **319**, 214 (2008).
- [33] See for example: <http://www.statkraft.com/energy-sources/osmotic-power/>.
- [34] See for example:
<http://www.newscientist.com/article/dn19191-green-machine-a-salty-solution-for-power-generation.html>.
- [35] P. Simon and Y. Gogotsi. *Nat. Mater.* **7**, 845 (2008).
- [36] D. Brogioli, R. Zhao and P. M. Biesheuvel. *Energy Environ. Sci.* (2011). Accepted.
- [37] B. B. Sales, M. Saakes, J. W. Post, C. J. N. Buisman, P. M. Biesheuvel and H. V. M. Hamelers. *Environ. Sci. Technol.* **44**, 5661 (2010).
- [38] P. M. Biesheuvel. *J. Colloid Interface Sci.* **332**, 258 (2009).
- [39] S. J. Blundell and K. M. Blundell. *Concepts in Thermal Physics*. Oxford University Press, Oxford (2006).
- [40] P. M. Biesheuvel. Private Communication.
- [41] J. J. Bikerman. *Philos. Mag.* **33**, 384 (1942).
- [42] M. Z. Bazant, M. S. Kilic, S. B. D. and A. Ajdari. *Adv. Colloid Interface Sci.* pages 48–88 (2009).
- [43] I. Borukhov, D. Andelman and H. Orland. *Phys. Rev. Lett.* **79**, 435 (1997).
- [44] V. Kralj-Iglic and A. Iglic. *J. Phys. II France* **6**, 477 (1996).
- [45] V. N. Paunov and B. P. Binks. *Langmuir* **15**, 2015 (1999).
- [46] V. N. Paunov, R. I. Dimova, P. A. Kralchevsky, G. Broze and A. Mehreteab. *J. Colloid Interface Sci.* **182**, 239 (1966).
- [47] R. van Roij. *Physica A* **389**, 4317 (2010).
- [48] D. Chapman. *Philos. Mag.* **25**, 475 (1913).
- [49] R. Ettelaie and R. Buscall. *Adv. Colloid Interface Sci.* **61**, 131 (1995).
- [50] P. M. Biesheuvel. *J. Colloid Interface Sci.* **238**, 362 (2001).
- [51] B. W. Ninham and V. A. Parsegian. *J. Theor. Biol.* **31**, 405 (1971).
- [52] A. Torres, R. van Roij and G. Tellez. *J. Colloid Interface Sci.* **301**, 176 (2006).
- [53] J. Chmiola, G. Yushin, Y. Gogotsi, C. Portet, P. Simon and P. L. Taberna. *Science* **313**, 1760 (2006).
- [54] R. Zhao, P. M. Biesheuvel, H. Miedema, H. Bruning and A. van der Wal. *J. Phys. Chem. Lett.* **1**, 205 (2010).
- [55] P. M. Biesheuvel and M. Z. Bazant. *Phys. Rev. E* **81**, 031502 (2010).
- [56] M. Z. Bazant, K. Thornton and A. Ajdari. *Phys. Rev. E* **70**, 021506 (2004).
- [57] U. Marini Bettolo Marconi and P. Tarazona. *J. Chem. Phys.* **110**, 8032 (1999).
- [58] U. Marini Bettolo Marconi and P. Tarazona. *J. Phys. Condens. Matter* **12**, A413 (2000).
- [59] A. J. Archer and R. Evans. *J. Chem. Phys.* **121**, 4246 (2004).
- [60] T. Hiemstra, J. C. M. De Wit and W. H. Van Riemsdijk. *J. Colloid Interface Sci.* **133**, 105 (1989).
- [61] M. Kosmulski. *Colloids Surf., A* **222**, 113 (2003).
- [62] G. V. Franks. *J. Colloid Interface Sci.* **249**, 44 (2002).
- [63] M. Kosmulski. *J. Colloid Interface Sci.* **208**, 543 (1998).

- [64] M. E. Labib and R. Williams. *Colloid Polymer Sci.* **264**, 533 (1986).
- [65] M. E. Labib and R. Williams. *J. Colloid Interface Sci.* **115**, 330 (1987).
- [66] W. Stöber, A. Fink and E. Bohn. *J. Colloid Interface Sci.* **26**, 62 (1968).
- [67] A. Labrosse and A. Burneau. *J. Non-Cryst. Sol.* **221**, 107 (1997).
- [68] G. H. Bogush, M. A. Tracy and C. F. Zukoski Jr. *J. Non-Cryst. Sol.* **104**, 95 (1988).
- [69] A. Burneau and B. Humbert. *Colloids Surf., A* **75**, 111 (1993).
- [70] A. Walcarius, C. Despas and J. Bessière. *Microporous Mesoporous Mater.* **23**, 309 (1998).
- [71] R. Kramer Campen, A. K. Pymer, S. Nihonyanagi and E. Borguet. *J. Phys. Chem. C.* **114**, 18465 (2010).
- [72] A. de Keizer, E. M. van der Ent and L. K. Koopal. *Colloids Surf., A* **142**, 303 (1998).
- [73] N. Boon and R. van Roij. *J. Chem. Phys.* **134** (2011).
- [74] J. Zhuravlev. *J. Colloid Interface Sci.* **3**, 316 (1987).
- [75] J. Zwanikken and R. van Roij. *Phys. Rev. Lett.* **99**, 178301 (2007).
- [76] C. Despas, A. Walcarius and J. Bessiere. *Langmuir* **15**, 3186 (1999).
- [77] D. E. Yates and T. W. Healy. *J. Colloid Interface Sci.* **55**, 9 (1976).
- [78] D. E. Yates, S. Levine and T. W. Healy. *J. Chem. Soc., Faraday Trans. 1* **F 70**, 1807 (1974).
- [79] L. Jelinek, P. Dong, C. Rojas-Pazos, H. Taibi and E. S. Kovats. *Langmuir* **8**, 2152 (1992).
- [80] O. Punkkinen, A. Naji, R. Podgornik, I. Vattulainen and P.-L. Hansen. *Europhys. Lett.* **82**, 48001 (2008).
- [81] J. Wu, D. Bratko and J. M. Prausnitz. *PNAS* **95**, 15169 (1998).
- [82] P. Linse and V. Lobaskin. *Phys. Rev. Lett.* **83**, 4208 (1999).
- [83] R. R. Netz. *European Physical Journal E* **5**, 557 (2001).
- [84] T. T. Nguyen, A. Y. Grosberg and B. I. Shklovskii. *Phys. Rev. Lett.* **85**, 1568 (2000).
- [85] I. Rouzina and V. A. Bloomfield. *J. Phys. Chem.* **100**, 9977 (1996).
- [86] M. M. Hatlo and R. Van Roij (2011). Submitted.
- [87] P. Linse. *J. Chem. Phys.* **94**, 3817 (1991).
- [88] P. Linse. *J. Chem. Phys.* **110**, 3493 (1999).
- [89] G. Téllez and E. Trizac. *Phys. Rev. E* **70**, 011404 (2003).
- [90] G. Téllez and E. Trizac. *Phys. Rev. E* **68**, 061401 (2003).
- [91] S. Pianegonda, M. C. Barbosa and Y. Levin. *Europhys. Lett.* **71**, 831 (2005).
- [92] D. Ben-Yaakov, D. Andelman, D. Harries and R. Podgornik. *J. Phys. Condens. Matter* **21**, 424106 (2009).
- [93] M. M. Hatlo and L. Lue. *Soft Matter* **5**, 125 (2009).
- [94] A. P. dos Santos, A. Diehl and Y. Levin. *J. Chem. Phys.* **132**, 104105 (2010).
- [95] M. M. Hatlo and L. Lue. *Europhys. Lett.* **89**, 25002 (2010).
- [96] A. Y. Grosberg, T. T. Nguyen and B. I. Shklovskii. *Rev. Mod. Phys.* **74**, 329 (2002).
- [97] L. Hong, A. Cacciuto, E. Luijten and S. Granick. *Langmuir* **24**, 621 (2008).

- [98] S. Tyagi, A. Arnold and C. Holm. *J. Chem. Phys.* **127**, 154723 (2007).
- [99] S. Tyagi, M. Sützen, M. Sega, M. Barbosa, S. Kantorovich and C. Holm. *J. Chem. Phys.* **132**, 154112 (2010).
- [100] Z.-Y. Wang and Y.-Q. Ma. *J. Chem. Phys.* **133**, 064704 (2010).
- [101] M. Kanduč, A. Naji, J. Forsman and R. Podgorinik. arxiv **1101.1362v1**, 1 (2011).
- [102] R. H. Hardin, N. J. A. Sloane and W. D. Smith. Maximal minimum distance dataset of 100 points distributed on a 3D sphere.
- [103] D. Frenkel and B. Smit. *Understanding Molecular Simulation: From Algorithms to Applications*. Academic Press (2002).
- [104] E. Wigner and F. Seitz. *Phys. Rev.* **43**, 804 (1933).
- [105] R. A. Marcus. *J. Chem. Phys.* **23**, 1057 (1955).
- [106] T. Ohtsuki, S. Mitaku and K. Okano. *Jpn. J. Appl. Phys.* **17**, 627 (1978).
- [107] R. Nozawa. *J. Math. Phys.* **7**, 1841 (1966).
- [108] S. C. Glotzer and M. J. Solomon. *Nat. Mater.* **6**, 557 (2007).
- [109] B. P. Binks. *Curr. Opin. Colloid Interface Sci.* **7**, 21 (2002).
- [110] P. Pieranski. *Phys. Rev. Lett.* **45**, 569 (1980).
- [111] D. Frydel, S. Dietrich and M. Oettel. *Phys. Rev. Lett.* **99**, 118302 (2007).
- [112] S. U. Pickering. *J. Chem. Soc.* **91**, 2001 (1907).
- [113] K. Stratford, R. Adhikari, I. Pagonabarraga, J. C. Desplat and M. E. Cates. *Science* **309**, 2198 (2005).
- [114] M. E. Cates and P. S. Clegg. *Soft Matter* **4**, 2132 (2008).
- [115] W. Chen, S. Tan, T.-K. Ng, W. T. Ford and P. Tong. *Phys. Rev. Lett.* **95**, 218301 (2005).
- [116] K.-S. Cho, D. V. Talapin, W. Gaschler and C. B. Murray. *J. Am. Chem. Soc.* **127**, 7140 (2005).
- [117] J. H. Liao, K. J. Chen, L. N. Xu, C. W. Ge, J. Wang, L. Huang and N. Gu. *Appl. Phys. A* **76**, 541 (2003).
- [118] A. Dominguez, D. Frydel and M. Oettel. *Phys. Rev. E.* **77**, 020401 (2008).
- [119] N. Hoffman, C. N. Likos and J. P. Hansen. *Mol. Phys.* **102**, 857 (2004).
- [120] Z. J. Lian and H. R. Ma. *J. Chem. Phys.* **127**, 104507 (2007).
- [121] R. Ramirez and R. Kjellander. *J. Chem. Phys.* **125**, 144110 (2006).
- [122] S. J. Miklavic, D. Y. C. Chan, L. R. White and T. W. Healy. *J. Phys. Chem.* **98**, 9022 (1994).
- [123] A. M. Khachatourian and A. O. Wistrom. *J. Phys. Chem. B.* **102**, 2483 (1998).
- [124] R. J. F. Leote de Carvalho, E. Trizac and J. P. Hansen. *Phys. Rev. E.* **61**, 1634 (2000).
- [125] A. Walther and A. H. E. Muller. *Soft Matter* **4**, 663 (2008).
- [126] L. Hong, A. Cacciuto, E. Luijten and S. Granick. *Nano Lett.* **6**, 2510 (2006).
- [127] E. Eggen and R. van Roij. *Phys. Rev. E.* **80**, 041402 (2009).
- [128] R. Ramirez and R. Kjellander. *J. Chem. Phys.* **119**, 11380 (2003).
- [129] R. J. Hunter. *Foundations of colloid science*. Oxford University Press, Oxford; New York (2001).
- [130] J. L. Barrat and J. P. Hansen. Basic concepts for simple and complex fluids.

- Cambridge University Press (2003).
- [131] J. C. Crocker and D. G. Grier. *Phys. Rev. Lett.* **73**, 352 (1994).
- [132] E. B. Sirota, H. D. Ou-Yang, S. K. Sinha, P. M. Chaikin, J. D. Axe and Y. Fujii. *Phys. Rev. Lett.* **62**, 1524 (1989).
- [133] Y. Monovoukas and A. P. Gast. *J. Colloid Interface Sci.* **128**, 533 (1989).
- [134] T. Okubo. *Chem. Soc. Faraday Trans.* **86**, 2871 (1990).
- [135] T. Okubo. *J. Chem. Phys.* **95**, 3690 (1991).
- [136] M. O. Robbins, K. Kremer and G. S. Grest. *J. Chem. Phys.* **88**, 3286 (1988).
- [137] E. J. Meijer and D. Frenkel. *J. Chem. Phys.* **94**, 2269 (1991).
- [138] S. Hamaguchi, R. T. Farouki and D. H. E. Dubin. *Phys. Rev. E* **56**, 4671 (1997).
- [139] A.-P. Hynninen and M. Dijkstra. *Phys. Rev. E.* **68**, 021407 (2003).
- [140] M. E. Leunissen, C. G. Christova, A.-P. Hynninen, C. P. Royall, A. I. Campbell, A. Imhof, M. Dijkstra, R. van Roij and A. van Blaaderen. *Nature (London)* **437**, 235 (2005).
- [141] J. Dobnikar, Y. Chen, R. Rzehak and H. H. von Grünberg. *J. Chem. Phys.* **119**, 4971 (2003).
- [142] P. M. Biesheuvel. *J. Phys.: Condens. Mat.* **16**, L499 (2004).
- [143] M. Rasa, B. Ern e, B. Zoetekouw, R. van Roij and A. P. Philipse. *J. Phys.: Condens. Mat.* **17**, 2293 (2005).
- [144] R. van Roij. *J. Phys.: Condens. Mat.* **15**, S3569 (2003).
- [145] C. P. Royall, M. E. Leunissen, A.-P. Hynninen, D. M. and A. van Blaaderen. *J. Chem. Phys.* **124**, 244706 (2006).
- [146] J. W. Merrill, S. K. Sainis and E. R. Dufresne. *Phys. Rev. Lett.* **103**, 138301 (2009).
- [147] E. Trizac and Y. Levin. *Phys. Rev. E* **69**, 031403 (2004).
- [148] T. E. Colla, Y. Levin and E. Trizac. *J. Chem. Phys.* **131**, 074115 (2009).
- [149] P. Wette, I. Klassen, D. Holland-Moritz, D. M. Herlach, H. J. Sch u pe, N. Lorenz, H. Reiber, T. Palberg and S. V. Roth. *J. Chem. Phys.* **132**, 131102 (2010).
- [150] A. Toyotama, T. Sawada, J. Yamanaka and K. Kitamura. *Langmuir* **19**, 3236 (2003).
- [151] L. F. Rojas-Ochoa, R. Casta eda Priego, V. Lobaskin, A. Stradner, F. Scheffold and P. Schurtenberger. *Phys. Rev. Lett.* **100**, 178304 (2008).
- [152] B. W. Ninham and V. A. Parsegian. *J. Theor. Biol.* **31**, 405 (1971).
- [153] D. Y. C. Chan and D. J. Mitchel. *J. Colloid Interface Sci.* **227**, 152 (2000).
- [154] S. H. Behrens and J. Borkovec. *J. Chem. Phys.* **111**, 382 (1999).
- [155] T. Gisler, S. F. Schulz, M. Borkovec, H. Sticher, P. Schurtenberger, B. D'Aguzzo and R. Klein. *J. Chem. Phys.* **101**, 9924 (1994).
- [156] H. H. von Gr nberg. *J. Colloid Interface Sci.* **219**, 339 (1999).
- [157] I. Popa, P. Sinha, M. Finessi, P. Maroni, G. Papastavrou and M. Borkovec. *Phys. Rev. Lett.* **104**, 228301 (2010).
- [158] T. Palberg, W. M nch, F. Bitzer, R. Piazza and T. Bellini. *Phys. Rev. Lett.* **74**, 4555 (1995).
- [159] J.-P. Hansen and H. L wen. *Annu. Rev. Phys. Chem.* **51**, 209 (200).

- [160] J. C. Neu. *Phys. Rev. Lett.* **82**, 1072 (1999).
- [161] H. H. von Grünberg, R. van Roij and G. Klein. *Europhysics Letters* **55**, 580 (2001).
- [162] R. Klein and H. H. von Grunberg. *Pure and Applied Chemistry* **73**, 1705 (2001).
- [163] M. N. Tamashiro and H. Schiessel. *Journal of Chemical Physics* **119**, 1855 (2003).
- [164] G. Tellez and E. Trizac. *Journal of Chemical Physics* **118**, 3362 (2003).
- [165] E. Trizac. *Phys. Rev. E* **62**, R1465 (2000).
- [166] Y. Levin. *Rep. Prog. Phys.* **65**, 1577 (2002).
- [167] J. W. Zwanikken and M. O. de la Cruz. *Phys. Rev. E* **82**, 050401 (2010).
- [168] N. Ise, T. Okubo, M. Sugimura, K. Ito and H. J. Nolte. *Journal of Chemical Physics* **78**, 536 (1983).
- [169] G. M. Kepler and S. Fraden. *Phys. Rev. Lett.* **73**, 356 (1994).
- [170] M. D. Carbajal-Tinoco, F. Castro-Román and J. L. Arauz-Lara. *Phys. Rev. E* **53**, 3745 (1996).
- [171] A. E. Larsen and D. G. Grier. *Nature* **385**, 230 (1997).
- [172] R. Vreeker, A. J. Kuin, D. C. Den Boer, L. L. Hoekstra and W. G. M. Agterof. *Journal of Colloid and Interface Science* **154**, 138 (1992).
- [173] W. Chen, S. S. Tan, Z. S. Huang, T. K. Ng, W. T. Ford and P. Tong. *Phys. Rev. E* **74**, 021406 (2006).
- [174] S. Perkin, N. Kampf and J. Klein. *Phys. Rev. Lett.* **96**, 038301 (2006).
- [175] I. Popa, G. Papastavrou and M. Borkovec. *Phys. Chem. Chem. Phys.* **12**, 4863 (2010).
- [176] J. Z. Wu, D. Bratko, H. W. Blanch and J. M. Prausnitz. *Phys. Rev. E* **62**, 5273 (2000).
- [177] S. H. Behrens and M. Borkovec. *Phys. Rev. E* **60**, 7040 (1999).
- [178] S. H. Behrens and M. Borkovec. *J. Phys. Chem. B* **103**, 2918 (1999).
- [179] D. Chan, T. W. Healy and L. R. White. *J. Chem. Soc., Faraday Trans. 1 F* **72**, 2844 (1976).
- [180] D. Y. C. Chan, R. M. Pashley and L. R. White. *Journal of Colloid and Interface Science* **77**, 283 (1980).
- [181] D. Y. C. Chan and D. J. Mitchell. *Journal of Colloid and Interface Science* **95**, 193 (1983).
- [182] R. Percet-Camara, G. Papastavrou, S. H. Behrens and M. Borkovec. *J. Phys. Chem. B* **108**, 19467 (2004).
- [183] M. Lund and B. Jönsson. *Biochemistry* **44**, 5722 (2005).
- [184] F. B. da Silva, M. Lund, B. Jönsson and T. Åkesson. *J. Phys. Chem. B* **110**, 4459 (2006).
- [185] M. Lund, T. Åkesson and B. Jönsson. *Langmuir* **21**, 8385 (2005).
- [186] S. J. Miklavic, D. Y. C. Chan, L. R. White and T. W. Healy. *J. Phys. Chem.* **98**, 9022 (1994).
- [187] P. Richmond. *J. Chem. Soc., Faraday Trans. 2* **8**, 1066 (1974).
- [188] C. Valeriani, P. J. Camp, J. W. Zwanikken, R. van Roij and M. Dijkstra. *Soft Matter* **6**, 2793 (2010).

- [189] D. Antypov, M. C. Barbosa and C. Holm. *Phys. Rev. E* **71**, 061106 (2005).
- [190] D. C. Grahame. *Chem. Rev.* **41**, 441 (1947).
- [191] T. W. Healy and L. R. White. *Adv. Colloid Interface Sci.* **9**, 303 (1978).
- [192] M. M. Hatlo and L. Lue. *Soft Matter* **4**, 1582 (2008).
- [193] B. Zoetekouw and R. van Roij. *Phys. Rev. E* **73**, 021403 (2006).
- [194] J. Drelich and Y. U. Wang. *Adv. Colloid Interface Sci.* **165**, 91 (2011).
- [195] J. Drelich, J. Long and A. Yeung. *Can. J. Eng.* **85**, 625 (2007).
- [196] W. Chen, S. Tan, Y. Zhou, T.-K. Ng, W. T. Ford and P. Tong. *Phys. Rev. E* **79**, 041403 (2009).
- [197] E. E. Meyer, Q. Lin, T. Hassenkam, E. Oroudjev and J. N. Israelachvili. *PNAS* **102**, 6839 (2005).
- [198] S. Sennato, D. Truzzolillo, F. Bordi, F. Sciortino and C. Cametti. *Colloids Surf., A* **343**, 34 (2009).
- [199] N. Kampf, D. Ben-Yaakov, D. Andelman, S. A. Safran and J. Klein. *Phys. Rev. Lett.* **103**, 118304 (2009).
- [200] V. A. Parsegian and D. Gingell. *Biophysical Journal* **12**, 1192 (1972).
- [201] A. Torres and R. Van Roij. *Langmuir* **24**, 1110 (2008).
- [202] F. Smalenburg, N. Boon, M. Kater, M. Dijkstra and R. van Roij. *J. Chem. Phys* **134**, 074505 (2011).
- [203] J. Gregory and A. J. Wishart. *Colloids Surf.* **1**, 313 (1980).
- [204] I. Popa, G. Gillies, G. Papastavrou and M. Borkovec. *J. Phys. Chem B* **114**, 3170 (2010).
- [205] S. J. Miklavcic. *Journal of Chemical Physics* **103**, 4794 (1995).
- [206] R. Brewster, P. A. Pincus and S. A. Safran. *Phys. Rev. Lett.* **101** (2008).
- [207] D. Velegol and P. K. Thwar. *Langmuir* **17**, 7687 (2001).
- [208] N. Kozlova and M. M. Santore. *Langmuir* **22**, 1135 (2005).
- [209] M. M. Santore and N. Kozlova. *Langmuir* **23**, 4782 (2007).
- [210] R. Duffadar, S. Kalasin, J. M. Davis and M. M. Santore. *Journal of Colloid and Interface Science* **337**, 396 (2009).
- [211] N. Hoffmann, C. Likos and J. P. Hansen. *Mol. Phys.* **102**, 857 (2004).
- [212] Z. J. Lian and H. R. Ma. *Journal of Chemical Physics* **127**, 104507 (2007).
- [213] N. Boon, E. C. Gallardo, S. Zheng, E. Eggen, M. Dijkstra and R. van Roij. *J. Phys.: Condens. Matt.* **22**, 104104 (2010).
- [214] B. V. Derjaguin, V. M. Muller and Y. P. Toporov. *Journal of Colloid and Interface Science* **53**, 314 (1975).
- [215] E. Kokkoli and F. Zukoski. *Langmuir* **17**, 369 (2001).

Samenvatting voor iedereen

De 19e eeuw mag gezien worden als het startpunt van de thermodynamica. Sadi Carnot was in 1825 de eerste die thermische energiestromen, warmte, kwantitatief relateerde aan mechanische arbeid en hierdoor voorspellingen kon doen van de maximale efficiëntie van stoommachines en hoe deze efficiëntie bereikt kon worden. Dit zou uiteindelijk leiden tot de 1e en de 2e hoofdwet van de thermodynamica die het behoud van energie en de richting van warmte beschrijven. De juistheid van deze wetten wordt vandaag de dag niet bediscussieerd. Toch formuleerde James Clerk Maxwell in 1867 een beroemd gedachte-experiment dat destijds twijfel over een van deze basisregels van de thermodynamica zaaide. Het door hem geformuleerde probleem zou later aantonen dat een statistische benadering van de thermodynamica noodzakelijk is.

Maxwell stelde zich twee compartimenten voor met daarin gasmoleculen, verbonden met een kleine afsluitbare opening die bediend wordt door een goed oplettende en vooral behendige poortwachter. Deze is dankzij Lord Kelvin later bekend geworden als 'Maxwell's demon'. De poortwachter heeft de mogelijkheid de afsluiting te openen wanneer deze maar wil en we gaan ervan uit dat het openen en het sluiten een verwaarloosbare hoeveelheid energie kost. Zo kan de poortwachter er voor kiezen om snelle moleculen alleen door te laten als deze uit het linker reservoir komen, en om langzame moleculen alleen door te laten als deze uit het rechter reservoir afkomstig zijn. Hierdoor zal de gemiddelde snelheid van de moleculen in het linker reservoir steeds maar dalen, terwijl deze in het rechter reservoir blijft toenemen. Aangezien de gemiddelde snelheid van de moleculen direct gerelateerd is aan de temperatuur resulteert dit in de situatie dat het linker reservoir afkoelt, terwijl het rechter reservoir steeds warmer wordt. Het zou niet ingewikkeld zijn om dit temperatuurverschil vervolgens te gebruiken om bijvoorbeeld mechanische arbeid te verrichten. Dit alles is in strikte tegenspraak met de 2e hoofdwet van de thermodynamica, die Carnot impliciet al beschreef maar in 1854 exacter verwoord werd door Clausius: *Es gibt keine periodisch arbeitende funktionierende Maschine, die nichts anderes tut, als Wärme in mechanische Arbeit zu verwandeln.*

Het probleem blijkt bij de duivelse poortwachter te liggen. Zelfs een maximaal efficiënt werkende poortwachter houdt bij al dat geregeld aan de poort niet oneindig lang het hoofd koel, en staat daardoor warmte af aan zijn omgeving. Bij het tot-

standkomen van elk besluit om de poort wel of niet open te zetten blijkt het voor de poortwachter namelijk fysisch noodzakelijk te zijn om een minimale hoeveelheid energie te verbruiken teneinde zichzelf alert te houden. Om zijn of haar energievoorraad vervolgens op pijl te houden rest de poortwachter geen andere keus dan af en toe wat nieuwe energie in te slaan, bijvoorbeeld door te eten. Dit laatste aspect zorgt ervoor dat de 2e hoofdwet behouden blijft.

De beperking die de 2e hoofdwet legt op Maxwell's demon is universeel. De hoeveelheid wanorde, of entropie, moet namelijk globaal altijd blijven toenemen. De enige manier om toch ergens orde te scheppen is door het creëren van extra wanorde ergens anders, bijvoorbeeld door het omzetten van chemische energie in warmte. De 'wisselkoers' tussen energie en orde is wat we kennen als temperatuur. Zo kunnen we bijvoorbeeld uitrekenen dat er bij een taak zoals het alfabetisch rangschikken van een significante verzameling boeken of artikelen minimaal een energie van ongeveer 10^{-18} Joule verstoekt moet worden in onze hersenen. Dit is uiteraard een erg kleine hoeveelheid energie, die bovendien veel kleiner is dan wat er in werkelijkheid verbruikt zal worden, maar deze is niet gelijk aan nul.

De hoeveelheid energie die als ruilmiddel kan worden ingezet voor het plaatselijk aanbrengen van orde blijkt over het algemeen dus erg klein te zijn voor relatief kleine verzamelingen die we in alledaagse leven tegenkomen, maar kan aanzienlijk worden bij gebeurtenissen waar ontzettend veel objecten of deeltjes bij betrokken zijn. Dit zijn met name processen die zich afspelen op een moleculaire schaal. Het is bovendien ook mogelijk de energie weer terug te winnen op het moment dat de wanorde weer hersteld wordt.

De bovenstaande analyse is ook toe te passen op de waterkringloop op aarde. Overal waar zeewater verdampt, om later regenwater te vormen dat rivieren van water voorziet, zal het zout achterblijven in de zee. Om zoet water te maken heeft men dus het zoute water van het zoete water moeten scheiden, wat orde schept en dus netto een beetje energie kost. Bij riviermondingen, waar de wanorde weer vergroot wordt, is er noodzakelijkerwijs energie te winnen. Aangezien er zich ontzettend veel zoutionen meer bevinden in een liter zeewater dan in een liter rivierwater kan deze hoeveelheid energie aardig oplopen. Voor een liter rivierwater die wordt gemengd met zeewater is dat al gauw meer dan 1000 Joule. De hoeveelheid energie die te winnen is uit de rivier is daarmee gelijk aan dat van een waterval met meer dan 100 meter hoogteverschil. Het winnen van deze energie gaat echter niet vanzelf. Normaal gesproken gaat het dan ook verloren in de riviermonding.

In dit proefschrift hebben we een recentelijk ontwikkelde methode onderzocht om deze energie te winnen. Belangrijk hiervoor is dat opgelost zout bestaat uit positieve ionen en negatieve ionen. Door een paar (+ & -) poreuze koolstofelektroden op te laden terwijl deze ondergedompeld zijn in zeewater worden deze zoutionen gevangen in het elektrisch veld van de elektroden, waarna ze even later weer worden

vrijgelaten in zoet water door de elektroden daarin te ontladen. Met dit cyclische proces houdt men telkens wat energie over. Deze methode is nog maar enkele jaren oud en wordt deze momenteel experimenteel onderzocht bij 'Wetsus' in Leeuwarden.

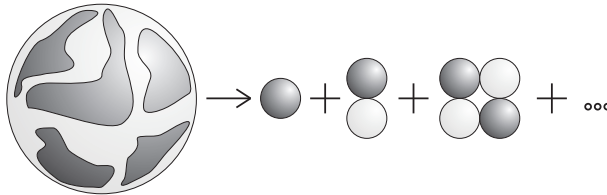
Belangrijk in onze analyse is een relatie tussen de spanning over de elektroden en de hoeveelheid lading die er naartoe getransporteerd is. Zouden er geen ionen aanwezig zijn dan zou dit een eenvoudige relatie zijn; we kunnen in dit geval volstaan met Poisson's beschrijving van het elektrisch veld rondom geladen objecten. De aanwezigheid van ionen maakt het een en ander wat complexer, zo wordt de spanning ook afhankelijk van de zoutconcentratie. Het mechanisme achter de beschreven vorm van 'blue energy' is dan ook dat tijdens het laden de spanning over de elektroden laag blijft als gevolg van het neutraliserende effect van de tegenovergesteld geladen ionen in het zeewater. Het ontladen gaat gepaard met extra vermogen aangezien in zoet water het neutraliserende effect veel minder is. Geïnspireerd door dit principe, beschrijven we in hoofdstuk 3 een cyclisch proces waarbij theoretisch gezien alle energie uit het mengen geëxtraheerd kan worden.

De concentratie van ionen in de nabijheid van de elektroden kan tot op zekere hoogte worden beschreven door de statistische wetten van Boltzmann in combinatie met Poisson's beschrijving van de elektrostatiche interactie tussen geladen objecten, deze gecombineerde theorie staat bekend als de Poisson-Boltzmann vergelijking en kan gezien worden als de rode draad in dit proefschrift. Wat we verwachten, namelijk dat positieve ionen zich niet graag in de omgeving bevinden van de positieve elektrode, en negatieve ionen juist wel, wordt met de Poisson-Boltzmann vergelijking kwantitatief gemaakt.

Het grootste deel van het proefschrift beschrijft echter de elektrostatiche eigenschappen van microscopisch kleine deeltjes in vloeistoffen. Deze deeltjes worden colloïden genoemd. Hun karakteristieke grootte, tussen enkele nanometers en een micrometer in, maakt dat ze een stuk groter zijn dan de moleculen waaruit de vloeistof is opgebouwd, maar klein genoeg om niet (snel) te bezinken in de vloeistof. Deze deeltjes hebben vaak een significante elektrostatiche lading omdat ze ionen uitwisselen met de omringende vloeistof. De klassieke theorie die onder andere de elektrostatiche krachten beschrijft tussen colloïden is in de jaren '40 van de 20e eeuw geformuleerd door zowel de Russische wetenschappers Derjaguin en Landau als de Nederlanders Verwey en Overbeek. Het betreft de interactie tussen homogeen geladen colloïdale bollen in een vloeistof waarin ionen aanwezig zijn. DLVO-theorie houdt er rekening mee dat ionen met tegengestelde lading zich als een atmosfeer rondom de colloïden verzamelen. Colloïden die elkaar naderen, voelen daardoor een verminderde afstoting. De atmosfeer met tegengestelde lading reduceert de netto lading van een colloïde namelijk aanzienlijk.

In dit proefschrift hebben we deze beschrijving van de elektrostatica enigszins uit proberen te breiden naar de colloïden die vandaag de dag belangstelling gekre-

gen hebben, namelijk die met een inhomogene verdeling van lading over hun oppervlak. Metingen hebben namelijk laten zien dat veel colloïdale oppervlakken eigenlijk helemaal niet homogeen geladen zijn. Daarnaast is het ook steeds beter mogelijk geworden om gecontroleerd deeltjes te maken met allerlei oppervlaktestructuren, bijvoorbeeld deeltjes met een positief geladen bovenkant en een negatief geladen onderkant. De aanname is dat deze nieuwe colloïden eigenschappen hebben die nog niet zijn waargenomen voor de deeltjes die we al kennen, bijvoorbeeld dat ze zich kunnen organiseren in nog niet eerder waargenomen structuren. Een analyse waarbij zowel de ladingsverdeling als het bijbehorende elektrisch veld



Figuur 10.1: De ladingsverdeling van een willekeurig deeltje kan geschreven worden als een oneindige som van elementaire ladingsconfiguraties.

geschreven wordt als een som van een klassieke monopool, dipool, quadrupool, en hogere orde ladingsconfiguraties (polen), zoals geschetst voor de lading in Fig. 10.1, blijkt effectief te zijn om elektrostatistische interacties uit te rekenen tussen dit soort colloïden, aangezien vaak alleen de lagere ordes van belang zijn. In hoofdstuk 6 is daarnaast ook te zien dat er bij hooggeladen colloïden koppelingen ontstaan tussen de verschillende polen, wat ook invloed zal hebben op de totale interactie tussen de colloïden.

In hoofdstukken 7, 8, en 9 is het ladingsmechanisme van de colloïden zelf tegen het licht gehouden. We nemen aan dat de lading een dynamische grootte is, dat wil zeggen dat deze verandert in de nabijheid van andere colloïden. Dit effect staat bekend als ladingsregulatie. Het blijkt dat als we deze aanname doen het gebied waarin de colloïden een gerangschikte structuur vormen een stuk groter wordt. Ook blijkt er zich in het geval van identieke, maar inhomogeen geladen colloïden een netto aantrekkende kracht te kunnen ontwikkelen die geïnduceerd wordt door ladingsregulatie.

Dankwoord

De werkdagen van een promovendus kunnen soms druk zijn maar de sfeer is meestal ongedwongen, zaken zoals deadlines komen in mindere mate voor. Daarom gaf René van Roij me vier jaar terug twee tips mee: probeer 's ochtends een beetje op tijd op de zaak te zijn (ik zal de bijbehorende tijd hier maar niet noemen), en wees er op bedacht dat er een periode kan komen waarin het onderzoek even vastzit. Dat schijnt er bij te horen. Nu, aan het eind, bedenk ik me dat ondanks het gebrek aan sociale controle het academisch 'op tijd' zo slecht nog niet is. Bovendien heb ik gelukkig geen lange periodes gekend waarin mijn onderzoek geen kant op wilde. Mijn conclusie is dat ik dat laatste vooral te danken heb aan de fantastische begeleiding van René. Zijn enthousiasme en brede interesse spoorden me steeds weer aan om verschillende onderzoekslintjes uit te werpen en zorgde dat ik er naar uit kon kijken om tussenresultaten of problemen snel concreet te maken om ze zo te kunnen bediscussiëren. Ik ben hem daarnaast ondermeer ook erg dankbaar voor al zijn hulp bij het 'aan de man brengen' van onze resultaten en de bijzonder fijne manier waarop ik onze samenwerking beleefde.

Ik dank ook Marjolein Dijkstra voor haar enthousiasme maar toch ook kritische houding bij mooie gezamenlijke projecten, en de plezierige manier waarop deze werden besproken. Ik bedank mijn promotor Henk van Beijeren voor zijn scherpe blik en de goede suggesties betreffende het theoriehoofdstuk. Alfons van Blaaderen ben ik dankbaar voor zijn interesse tijdens werkbesprekingen en de vele suggesties die hij dan terloops gaf over onderzoek dat al wel of juist nog niet gedaan was.

Peter, Frank en Joost dank ik voor een hele aangename samenwerking bij voor mij zeer leerzame projecten, en ook alle andere collega's van de groep van René en de SCM en FCC groepen ben ik dankbaar voor interessante (werk)discussies en goede sfeer op conferenties.

Ik dank Joost, Els en Olga, en natuurlijk ook Geertje, Biene en Wilma voor alle essentiële ondersteunende en administratieve hulp bij mijn werkzaamheden. Daarnaast dank ik Jeroen voor het enthousiast delen van zijn computerkennis, en Fedde voor het verwijderen van de anglicismen uit de Nederlandse samenvatting.

Teun ben ik dank verschuldigd omdat hij me de wonderlijke wereld van de ex-

perimentele fysica heeft willen laten zien. Helaas dat we onze theorie over de tegenovergesteld geladen deeltjes uiteindelijk niet helemaal konden bewijzen maar ik vond het een mooie ervaring. Ook de road trip naar een conferentie Granada was onvergetelijk maar was natuurlijk nooit zo mooi geweest als Laura en Bas er ook niet bij waren geweest.

Wat betreft de alledaagse werkdag ben ik met name Timothy dank verschuldigd, die me al die jaren op gezette tijden achter mijn bureau weg trok voor een kop koffie. Iedereen weet dat de beste ideeën ontstaan tijdens een goede koffiepauze. Jildou, Ties, Erik en Rembert zijn degenen die in deze en/of in de sportieve context ook zeker het expliciet vermelden waard zijn, maar ook vele andere collega's van het ITF dank ik voor hulp en gezelligheid.

Daarnaast zijn er essentiële randvoorwaarden die het mogelijk maken om op een heldere en gemotiveerde manier bezig te blijven. Dat zijn in mijn geval de mensen die zorgden voor afleiding in de vorm van gezelligheid en sportiviteit. PMB'ers, schaatsers, woensdagavondfietzers, zondagavondborrelaars, QSSP'ers, buurvrouwen. Bedankt. Expliciet bedank ik Janneke voor een erg aangenaam tijdelijk onderkomen, en naast haar (met name) ook Judith, Matthijs en Rick voor hun bijzonder nuchtere blik op de wereld die ik alleen van binnen zie; dat werkt verhelderend op zijn tijd. Tenslotte bedank ik mijn familie, en met name mijn ouders, voor hun nooit aflatende enthousiasme over mijn bezigheden, en het zijn van een constante factor door de jaren heen.

Publications

The following list considers publications that were used as chapters. However, Chapters 4,5, and 9 are expected to be published soon after appearance of this thesis.

1. N. Boon and R. van Roij, '*Blue energy*' from ion adsorption and electrode charging in sea and river water, *Mol. Phys.* **109**, 1229 (2011). (Chapter 3)
2. N. Boon, E. Gallardo Carvajal, S. Zheng, E. Eggen, M. Dijkstra, and R. van Roij, *Screening of heterogeneous surfaces: charge renormalization of Janus particles*, *J. Phys.: Cond. Matter.* **22**, 104104 (2010). (Chapter 6)
3. F. Smallenburg, N. Boon, M. Kater, M. Dijkstra and R. van Roij, *Phase diagrams of colloidal spheres with a constant zeta-potential*, *J. Chem. Phys.* **134**, 074505 (2011). (Chapter 7)
4. N. Boon and R. van Roij, *Charge regulation and ionic screening of patchy surfaces*, *J. Chem. Phys.* **134**, 054706 (2011) (Chapter 8)